# Towards Doppler-free two-photon spectroscopy of trapped and cooled HD$^+$ ions

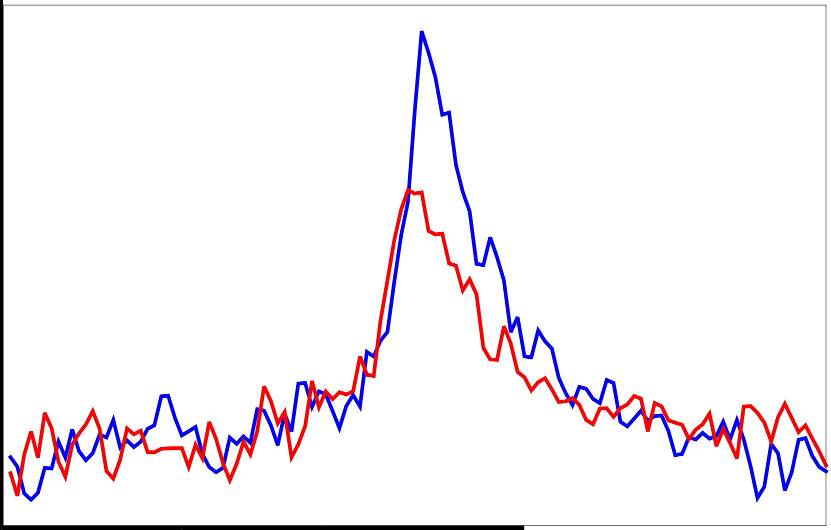

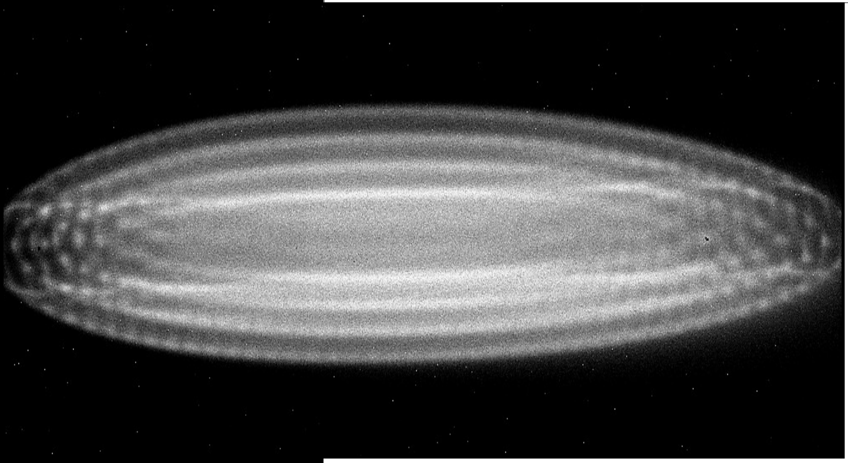

Sayan Patra

VRIJE UNIVERSITEIT AMSTERDAM

# Towards Doppler-free two-photon spectroscopy of trapped and cooled HD$^+$ ions

ACADEMISCH PROEFSCHRIFT

ter verkrijging van de graad Doctor of Philosophy
aan de Vrije Universiteit Amsterdam,
op gezag van de rector magnificus
prof.dr. V. Subramaniam,
in het openbaar te verdedigen
ten overstaan van de promotiecommissie
van de Faculteit der Bètawetenschappen
op donderdag 9 mei 2019 om 11.45 uur
in de aula van de universiteit,
De Boelelaan 1105

door

Sayan Patra
geboren te Burdwan, India

promotoren: prof.dr. W.M.G. Ubachs
prof.dr. K.S.E. Eikema
copromotor: dr. J.C.J. Koelemeij

To family and friends

A handful of elegant designs support Nature's exuberant
construction, from simple building blocks, of the material world.
-Frank Wilczek

This thesis was approved by the members of the reviewing committee:

dr. R. Gerritsma, Universiteit van Amsterdam, the Netherlands
prof.dr. P. Gori-Giorgi, Vrije Universiteit Amsterdam, the Netherlands
prof.dr. D. Iannuzzi, Vrije Universiteit Amsterdam, the Netherlands
dr. D. Leibfried, NIST Boulder, the United States of America
prof.dr. P.O. Schmidt, Leibniz Universität Hannover and PTB Braunschweig, Germany
dr. S. Sturm, Johannes Gutenberg-Universität Mainz and Max-Planck-Institut für Kernphysik, Germany

NWO Nederlandse Organisatie voor Wetenschappelijk Onderzoek

VU VRIJE UNIVERSITEIT AMSTERDAM

LaserLaB AMSTERDAM

This work is done as a part of the FOM-projectruimte “Time will tell; leads to new physics from a molecular optical clock” (13PR3109), which was financially supported by the Nederlandse Organisatie voor Wetenschappelijk Onderzoek (NWO). The research was performed at the LaserLaB, Vrije Universiteit Amsterdam.

# Contents

---

**1 Introduction 1**

1.1 Prologue 1

1.2 Determination of the proton-electron mass ratio $\mu_{\mathrm{pe}}$ 3

1.3 The hydrogen molecular ion $HD^+$: Benchmark system for testing molecular theory 4

1.4 Fundamental constants from $HD^+$ 6

1.5 Test of the Standard Model of particle physics and search for physics beyond it 8

1.6 Vibrational spectroscopy of the $HD^+$ ion 10

1.7 Outline and summary of this thesis 11

**2 Necessary background information 14**

2.1 Advances in *ab initio* calculations of the energy levels of $HD^+$ 14

2.1.1 Summary of recent advances in the calculations of the ro-vibrational transition frequencies of $HD^+$ 14

2.1.2 Hyperfine structure calculation 15

2.2 Summary of spectroscopy of the $(v, L) : (0, 2) \to (8, 3)$ overtone in $HD^+$ 16

2.3 Doppler-free two-photon spectroscopy of ro-vibrational transitions of $HD^+$ 22

2.3.1 Feasibility study 22

2.3.2 Limitations of the OBE model 29

**3 Experimental setup 32**

3.1 Laser-cooling of $Be^+$ ions and the ion trap setup 32

3.1.1 Ion trap setup 32

3.1.2 Laser-cooling setup for $Be^+$ ions 34

3.1.3 Experimental control and automation 38

3.1.4 Performance of the ion trap and laser-cooling setup 42

3.2 Frequency stabilisation of the spectroscopy lasers 43

3.2.1 The optical frequency comb (OFC) and the ultra-stable laser 44
3.2.2 The transfer-oscillator locking scheme 45
Principle and implementation 45
Performance of the frequency stabilisation scheme 53
Effect of intra-office optical fibre on the spectra purity of the lasers 57
Selection of $f_{\mathrm{rep}}$ of the OFC for multiple lasers 59

**4 *A priori* determination of required experimental parameters 61**
4.1 Introduction 61
4.2 Choice of hyperfine components 62
4.2.1 Zeeman shifts 62
4.2.2 Suppression of Doppler-broadened background 64
4.3 Modelling the Doppler-free two-photon spectrum: *a priori* determination of required experimental parameters 66
4.3.1 Brief review of the rate equation model 67
4.3.2 Calculation of the $(v, L) : (0, 3) \to (4, 2) \to (9, 3)$ Doppler-free two-photon spectrum: results 70
4.3.3 Estimate of frequency shift due to underlying Doppler-broadened background 75
4.4 Zeeman and AC Stark shifts 77
4.4.1 Zeeman shift 77
4.4.2 AC Stark shift due to the cooling laser at 313 nm and the dissociation laser at 532 nm 79

**Appendices 82**
4.A AC Stark shift due to the cooling laser and the dissociation laser 82

**5 Ghost features in Doppler-broadened spectra of ro-vibrational transitions in trapped HD$^+$ ions 84**
5.1 Introduction 84
5.2 Brief review of the rate equation model 85
5.3 Calculation of the $(v, L) : (0, 3) \to (4, 2)$ spectrum 87
5.4 Ghost features in $(v, L) : (0, 3) \to (4, 2)$ single-photon spectrum 89
5.5 Significance of ghost features for spectroscopy of trapped ions 96
5.6 Summary and conclusion 97

**6 Proton-electron mass ratio from HD$^+$ revisited 99**
6.1 Introduction 99
6.2 Improvement in theory 100
6.3 Comparison between experiment and theory 103

6.4 Determination of the proton-electron mass ratio $\mu_{\text{pe}}$ 106
6.5 Outlook and conclusion 111
6.6 Acknowledgments 112

**7 Observation of the $(v,L):(0,3) \rightarrow (9,3)$ two-photon transition in HD$^+$ 113**
7.1 Doppler-broadened $(v,L):(0,3) \rightarrow (9,3)$ ro-vibrational transition in HD$^+$ 113
7.2 Doppler-free two-photon $(v,L):(0,3) \rightarrow (9,3)$ transition in HD$^+$ 115
7.2.1 Experimental protocol and measured spectrum 115
7.2.2 Statistical test to distinguish "signal" from "noise" 119
The statistical test 119
Welch's $t$-test 121
Statistical analysis of the measured spectrum 122

**Appendices 126**
7.A Choice of optimum REMPD duration for the Doppler-free two-photon spectroscopy experiment 126

**8 Conclusion and Outlook 130**

**Bibliography 132**

**Acknowledgement 147**

Chapter 1

# Introduction

## 1.1 Prologue

A theory describing the interaction between electromagnetic radiation and matter, treating both the radiation field and matter quantum mechanically, was first formulated by Dirac in the 1920s. This theory was successfully employed to calculate the coefficient of spontaneous emission of an atom with a single electron [1]. In subsequent years, Dirac proposed a quantum theory of electrons consistent with the Special Theory of Relativity [2]. Dirac's theory also predicted the existence of positrons [3], which were experimentally detected by Anderson in 1932 [4]. However, it was found that Dirac's theory led to serious divergences in the calculation of the electron's self-energy when it is expanded in powers of $\alpha$, the fine structure constant [5–7]. Of particular interest to the development of the modern day formulation of Quantum Electrodynamics (QED) are further two predictions of Dirac's theory, namely, the magnetic moment of the electron and the degeneracy of the $2S_{1/2}$ and $2P_{1/2}$ levels in atomic hydrogen. The magnetic dipole moment of the electron is expressed in terms of the *g-factor*. The Dirac equation predicts the value of the *g-factor* for the electron $g_e = 2$.

In 1947, Kusch and co-workers measured $g_e$ to be $2(1.00119 \pm 0.00005)$, which is slightly different from 2 as predicted by Dirac [8–10]. The same year, in their classic experiment of measuring the fine structure of hydrogen atom using microwaves, Lamb and Retherford [11] discovered that the $2S_{1/2}$ and the $2P_{1/2}$ levels are not degenerate (Lamb shift), contrary to the prediction of Dirac's theory. Moreover, the hyperfine splitting in the ground states of atomic hydrogen and deuterium were also measured to be different from their theoretically predicted values, which assumed $g_e = 2$ [12]. These experimental results led to the present-day formalism of Quantum Electrodynamics, the relativistic quantum field theory (QFT) of electrodynamics successfully combining the Special Theory of Relativity and quantum mechanics. QED was developed by Bethe, Feynman, Schwinger, Tomonaga and Dyson in the 1940s [13–16]. In their formulation, the divergences encountered were avoided by writing the equations in terms of measurable, finite quantities such as charge and mass of the electron (renormalisation). Thorough and mathematically rigorous discussions on Quantum electrodynamics can be found in standard textbooks and is beyond the scope of this thesis (also beyond the expertise of the author). A primary consequence of this renormalisation essential to this thesis is that certain measurable quantities in terms of which the equations of QED are written, cannot be calculated *ab initio*, but have to be measured (this is true not only for QED, but for any renormalisable Quantum Field Theory (QFT)). These quantities in most cases, appear in most basic equations of physics and are called "fundamental constants". Examples of fundamental constants are the velocity of light in vacuum $c$, the mass of the electron $m_\mathrm{e}$, the charge of the electron $e$, the fine structure constant $\alpha$, the Planck's constant $h$, the Rydberg constant $R_\infty$ etc. A precise and accurate knowledge of the values of these fundamental constants is essential to the scientific community to provide accurate quantitative descriptions of the physical world. The Task Group on Fundamental Constants (TGFC) of the Committee on Data for Science and Technology (CODATA) was established in 1969 to provide the scientific community with a set of internationally accepted values of the fundamental constants. The first such compilation of fundamental constants was published in 1973 [17] and has since been periodically updated to take into account recent measurements of the fundamental constants. These constants can have dimensions (*e.g.* charge of an electron $e$) or also can be dimensionless (*e.g.* fine structure constant $\alpha$). In this thesis, the CODATA-14 recommendations of fundamental constants have been used [18], and in some cases, of CODATA-10 [19].

Since its inception, QED is one of the most precisely tested theories in physics. In general, a precision test of QED entails a comparison between theoretical prediction and an experimental result to the same end, leading to a determination of the fine-structure constant $\alpha$, which scales the electromagnetic interactions. $\alpha$ can be expressed as

$$\begin{aligned} \alpha &= \frac{e^2}{4\pi\epsilon_0\hbar c} \quad \text{in the S.I. system of units and} \\ \alpha &= \frac{1}{c} \quad \text{in atomic units.} \end{aligned} \tag{1.1}$$

In the Eq. 1.1, $c$ is the speed of light in vacuum and $\hbar = \frac{h}{2\pi}$ is the reduced Planck's constant. The value of $\alpha$ ($\approx \frac{1}{137}$) can be determined via various methods such as from the measurements of the constants appearing in its expression as in Eq. 1.1, or from the measurement of $h/m$ of atoms like Cs and

Rb [20,21]. $\alpha$ can also be measured directly using the Quantum Hall effect [22] or from the measurement of the anomalous magnetic moment of the electron ($g_e - 2$) [23]. Recently, a competitive measurement of $\alpha$ has also been performed using matter-wave interferometry [24]. In spite of its approximative nature, QED has proved to be a successful theory via consistent determination of $\alpha$ from the different methods mentioned above.

Precise QED calculations in molecules are in general more complicated than in atoms due to their rotations and vibrations in addition to the electronic structure. A precision test of QED in molecules can be performed via comparison between the measurement of a rotational-vibrational transition in a molecule and the corresponding theoretical prediction. For such a calculation, particularly important is a precise and accurate value of $\mu_{\mathrm{pe}}$, the proton-electron mass ratio (together with other fundamental constants) as it scales the rotational and vibrational energy levels in molecules. $\mu_{\mathrm{pe}}$ is also considered as a fundamental constant, although, in the strict definition of the term is not so. This is because, the electron, being a lepton, gains its mass due to its interaction with the Higgs field. The proton, on the other hand is a hadron and gains its mass from the gluons, the strong interaction (described by Quantum Chromodynamics or QCD) force carriers which bind the quarks together to form the proton. The mass of the proton $m_{\mathrm{p}}$ is proportional to $\Lambda_{QCD}$ which characterises the strength of the strong interactions.

This thesis describes an experiment designed to verify the calculations of energy corrections to molecular vibrational levels due to Quantum Electrodynamics in the hydrogen molecular ion $\mathrm{HD}^+$ and consequently put an improved or competitive constraint on the proton-electron mass ratio $\mu_{\mathrm{pe}}$. This also requires a precise and accurate knowledge of the deuteron-electron mass ratio $\mu_{\mathrm{de}}$, as $\mathrm{HD}^+$ nuclei are composed of a proton and a deuteron.

## 1.2 Determination of the proton-electron mass ratio $\mu_{\mathrm{pe}}$

The proton-electron mass ratio has been measured in different ways with increasing accuracy over the years. Most determinations of $\mu_{\mathrm{pe}}$ were done by taking the ratio of individual measurements of $m_{\mathrm{p}}$ and $m_{\mathrm{e}}$. In the 1980s, $\mu_{\mathrm{pe}}$ was determined via measuring cyclotron frequencies of free protons and electrons in a high magnetic field in a Penning trap, leading to uncertainties of 0.6 parts-per-million (ppm) [25] and 41 parts-per-billion (ppb) [26]. The determinations were further improved by Farnham *et al.* in 1995, when they compared the cyclotron frequencies of electrons and a single $\mathrm{C}^{6+}$ ions in a Penning trap [27]. Furthermore, in 2004, Verdú *et al.* improved the determination of the electron mass measurement by measuring the $g$-factor of an electron bound in $^{16}\mathrm{O}^{7+}$ ion in a Penning trap [28], and consequently, the precision of $\mu_{\mathrm{pe}}$. Later in 2011, the antiproton-electron mass ratio was determined as a single parameter from from measurements of two-photon transitions in antiprotonic helium [29]. By invoking the charge, parity and time-reversal symmetry (CPT symmetry) between the anti-proton and the proton, it was inferred that the antiproton-electron mass ratio is equal to the proton-electron mass ratio $\mu_{\mathrm{pe}}$ within the uncertainty limits.

Individually, the most precise determinations of $m_{\mathrm{e}}$ and $m_{\mathrm{p}}$ have been done with a relative uncertainty of 30 parts-per-trillion (ppt) [30] and 32 ppt [31] respectively, from measurements in Penning traps. The electron mass measurement entailed the combination of an extremely precise measurement of the magnetic moment of a single electron bound to a carbon nucleus and bound-state Quantum Electrodynamic calculations. The proton mass measurement on the other hand, was performed by comparing cyclotron frequencies of protons and highly charged carbon ions ($^{12}\mathrm{C}^{6+}$) in a purpose-built Penning trap. Although the precision of the proton atomic mass $m_{\mathrm{p}}$ measurement in Ref. [31] is about 3 times better than the current CODATA-14 [18] prescribed value of the same (relative uncertainty 89 ppt), the former exhibits a $3\sigma$ deviation from the latter. This discrepancy is a stimulus for further measurements of $m_{\mathrm{p}}$ with comparable or better uncertainties for consistency check.

In the 1970s, Wing *et al.* in their article “Observation of the infrared spectrum of the hydrogen molecular ion $\mathrm{HD}^+$” speculated that if the theory is improved for the calculation of ro-vibrational transition frequencies in $\mathrm{HD}^+$, then an experimental measurement of comparable accuracy would lead to the determination of several constants which scale the molecular energy levels, of which the least known at that time was the proton-electron mass ratio $\mu_{\mathrm{pe}}$ [32]. The first determination of $\mu_{\mathrm{pe}}$ has been done from a precise measurement of the $v : 0 \to 8$ vibrational overtone of $\mathrm{HD}^+$ with a relative uncertainty of 2.9 ppb [33].

## 1.3 The hydrogen molecular ion $\mathrm{HD}^+$: Benchmark system for testing molecular theory

The hydrogen atom is the simplest atom composed of a proton and an electron. Its transition frequencies can be calculated with very high accuracy. These calculations include not only the non-relativistic contribution, but also the relativistic and QED (radiative) corrections to it. The most accurate *ab initio* calculation of transition frequencies in atomic hydrogen are the transitions within the $n = 2$ manifold [18]. On the experimental front, the $1S_{1/2}$-$2S_{1/2}$ transition has been measured with a relative frequency uncertainty of $4.2 \times 10^{-15}$ [34,35]. This impressive theoretical and experimental precision in atomic hydrogen has made it the ideal system for testing QED.

For molecules, the situation is in general more dire than atoms. Molecules are composed of more than one atom. Due to their multi-particle structure, molecules have more degrees of freedom than atoms, leading to rotational and vibrational structure in addition to the electronic energy level structure. This makes the calculation of molecular energy level structure more difficult than for atoms. Even for the smallest neutral molecule $H_2$, calculation of its energy level structure is much more complicated than atomic hydrogen owing to the four-body (two protons and two electrons) structure of the former, in particular due the electron-electron correlation. Recently, calculations of the dissociation and transition energies of several rovibrational levels in the ground electronic state of $H_2$ has been done with a relative precision of $\sim 6 \times 10^{-9}$ [36]. These calculations agree well with the corresponding measurements [37–39] in most cases, but some discrepancies still remain [36].

In HD, an isotopologue of $H_2$, the $R(1)$ line of the $(2,0)$ overtone band ($(v, N)$ : $(2,2) \leftarrow (0,1)$, where $v$ and $N$ are the vibrational and rotational quantum numbers, repsectively) has been recently measured with a fractional frequency uncertainty $9.2 \times 10^{-11}$ [40] and $4 \times 10^{-10}$ [41]. Although the fractional frequency uncertainties of both the measurements mentioned above is much better than the $4 \times 10^{-9}$ relative frequency uncertainty of the *ab initio* calculation of the same [36, 40], a hitherto unresolved discrepancy of 900 kHz (about ten times the combined experimental uncertainty) was observed between them [40, 41]. An improvement in the theory, leading to uncertainties comparable to that of the measurements might lead to a resolution of the discrepancy. In light of Refs. [36, 42–44], it seems that a precision of $10^{-6}$ cm$^{-1}$ (30 kHz) on the energy levels in ground electronic state of $H_2$ and/or HD is feasible in near future.

Turning to the simplest molecule, the hydrogen molecular ion $H_2^+$ is composed of only three particles, namely, two protons and an electron, making its energy level structure calculations from first principles simpler than $H_2$/HD. Calculations of energies of a number of vibrational and rotational states of $H_2^+$ and its isotopologue $HD^+$ have been done by Moss, leading to calculations of the transition frequencies with a relative freqency uncertainty of $5 \times 10^{-9}$ [45, 46]. In these calculations, apart from the non-relativistic part of the energy, leading order relativistic ($\sim \alpha^2 R_\infty$) and radiative ($\sim \alpha^3 R_\infty$) corrections were also included. More recently, the accuracy and precision of the ro-vibrational transition frequency calculations in $H_2^+$ and $HD^+$ have been improved by orders of magnitude by Korobov, Karr and co-workers, in which not only they consider the leading order relativistic and radiative corrections, but also higher order QED corrections to the transition frequencies. The accuracy of the calculation of the fundamental ro-vibrational transition in $H_2^+$ in its ground electronic state is $\sim 8 \times 10^{-12}$ in relative frequency terms [47]. A detailed discussion regarding the method developed by Korobov and co-workers is beyond the purview of this thesis. Brief discussions of these calculations are presented in Chapter 2 (Section 2.1) and Chapter 6 (Section 6.2) of this thesis. Besides the ro-vibrational energy level structure, the hyperfine structure of $H_2^+$ is also known with very high accuracy [48, 49]. Hence the hydrogen molecular ion $H_2^+$ stands out to be an ideal system to test molecular theory.

On the experimental front, $H_2^+$ is not favourable. As it is a homonuclear molecule, it does not have a permanent electric dipole moment, leading to no dipole-allowed ro-vibrational transitions to measure. However, close to the dissociation limit of the ground electronic state, $g/u$ symmetry breaking due to the hyperfine Hamiltonian can lead to observable electric dipole excitations between otherwise (dipole) forbidden adjacent rotational levels. To this end, Critchley *et al.* observed and measured the $N : 1 \leftarrow 0$ rotational transition in the highest bound vibrational level $v = 19$ in the ground electronic state $1s\sigma_\mathrm{g}$ ($X\ ^2\Sigma_\mathrm{g}^+$) of $H_2^+$ [50, 51]. Also, a transition between the $(v = 19, N = 1)$ level in the ground electronic state and the $(v = 0, N = 2)$ level of the $2p\sigma_\mathrm{u}$ ($A\ ^2\Sigma_\mathrm{u}^+$) excited electronic state in $H_2^+$ was observed by Carrington and co-workers [52, 53]. Moreover, multi-photon and electric quadrupole transitions can also be probed. An experiment towards the observation and measurement of a two-photon transition between $v = 0$ and $v = 1$ vibrational levels in the ground electronic state of $H_2^+$ is underway in the group of L. Hilico and J.-Ph. Karr at Laboratoire Kastler Brossel in Paris, France [54–59].

Experimentally, $HD^+$, an isotopologue of $H_2^+$ is more amenable. $HD^+$ is also a three-body system like $H_2^+$, however unlike the latter, the former is a heteronuclear molecule, the nuclei being constituted of a proton and a deuteron. $HD^+$ has a small permanent electric dipole moment, leading to weak dipole allowed transitions. The ro-vibrational transitions and hyperfine structure of $HD^+$ can also be calculated with relative frequency uncertainties comparable to $H_2^+$ [47]. The excited vibrational levels in the ground electronic state of $HD^+$ exhibit lifetimes ~10 ms, leading to spectrally narrow transitions. Also, transitions can be found in the near-infrared (NIR) region of the electromagnetic spectrum, which can be measured with high precision due to easy availability of spectrally pure probe radiation sources.

In this work, an experiment towards measuring a dipole-forbidden ro-vibrational transition in $HD^+$ will be described with a target experimental accuracy better than the *ab initio* calculations. Such a measurement will allow the most stringent test of energy-level structure calculations of molecules in the framework of QED at the parts-per-trillion (ppt) level.

## 1.4 Fundamental constants from $HD^+$

In the Born-Oppenheimer approximation, the vibrational transition frequencies of a molecule $\nu_{vib} \propto \sqrt{m_\mathrm{e}/\mu}$ and the rotational transition frequencies $\nu_{rot} \propto m_\mathrm{e}/\mu$, where $\mu$ is the reduced nuclear mass. Hence, a precise and accurate measurement of a rotational or a vibrational transition would allow a determination of the ratio $m_\mathrm{e}/\mu$ from a molecule, provided the theoretical calculations are accurate enough and the uncertainty in the theoretical calculations is limited by the knowledge of the quantities $m_\mathrm{e}$ and $\mu$. For $\mathrm{H}_2^+$, the $\mu = m_\mathrm{p}/2$, as the nuclei are protons and hence, the proton-electron mass ratio $\mu_\mathrm{pe}$ can be determined from a single measurement of a rotational or vibrational transition. However, for HD$^+$, $\mu^{-1} = m_\mathrm{p}^{-1} + m_\mathrm{d}^{-1}$, where $m_\mathrm{d}$ is the mass of the deuteron. Hence, in HD$^+$, it is impossible to determine the individual mass ratios $m_\mathrm{e}/m_\mathrm{p}$ and $m_\mathrm{e}/m_\mathrm{d}$ from a single measurement. However, of the three quantities $m_\mathrm{e}$, $m_\mathrm{p}$ and $m_\mathrm{d}$, considering the most accurately (and precisely) known two quantities as input parameters, it is possible to put an improved constraint on the least precisely known one. In this manner, $\mu_\mathrm{pe}$ was determined from HD$^+$ by Biesheuvel *et al.* with a relative uncertainty of 2.9 parts-per-billion (ppb) [33]. In that work, the theoretical calculations considered fundamental constants prescribed by CODATA-10 [19]. With the publication of the more recent CODATA-14 values, it was realised that it is scientifically more prudent to constrain the value of $m_\mathrm{p}$ from the measurement of ro-vibrational transitions in hydrogen molecular ions [60]. This aspect will be addressed elaborately later in this thesis (see Chapter 6). More recently, similar reasoning led Alighanbari *et al.* to determine $m_\mathrm{p}$ with a relative uncertainty of 1.3 ppb, the most precise determination of the same from hydrogen molecular ions [61].

Recently, it has been found that the proton and deuteron charge radii $r_\mathrm{p}$ and $r_\mathrm{d}$ respectively, as determined from muonic hydrogen and muonic deuterium exhibits a $\sim 5\sigma$ discrepancy [62, 63] from the value of the same quantities recommended by CODATA-14. The reason for this discrepancy is still not understood and is known in the community as the “proton radius puzzle”. This has consequently put a question mark on the accuracy of the value of the Rydberg constant $R_\infty$ as recommended in CODATA-14 as it is closely related to $r_\mathrm{p}$ (via spectroscopy of atomic hydrogen) [64]. This has led to a series of new measurements to determine the quantities $r_\mathrm{p}$ and $r_\mathrm{d}$ from diverse systems for consistency checks [65]. It is also possible to weigh into the proton radius puzzle using ro-vibrational transitions in hydrogen molecular ions as a probe [59]. The energy $E_{vL}$ of the ro-vibrational levels in HD$^+$ can be expressed as

$$E_{vL} = E_{vL}(R_\infty, m_\mathrm{p}/m_\mathrm{e}, m_\mathrm{d}/m_\mathrm{e}, r_\mathrm{p}, r_\mathrm{d}), \tag{1.2}$$

where $v$ and $L$[1] are the vibrational and rotational quantum numbers. For $\mathrm{H}_2^+$, it can be expressed as a function of all the parameters mentioned in the above equation other than $m_\mathrm{d}$ and $r_\mathrm{d}$. By combining measurements from HD$^+$ and

---

[1] Henceforth, the rotational qunatum number will be denoted by $L$ in this thesis, unless mentioned otherwise.

$H_2^+$, it is possible to determine $r_\mathrm{p}$. Furthermore, by combining $n$ measurements of different ro-vibrational transitions in $H_2^+$ and $HD^+$, it is possible to determine $n$ fundamental constants as defined in Eq. 1.2 independently as proposed in Ref. [59].

## 1.5 Test of the Standard Model of particle physics and search for physics beyond it

The Standard Model of particle physics is the most successful theory describing how the elementary particles interact at the smallest scale. Of the four fundamental interactions describing the physical world, the Standard Model successfully incorporates the electromagnetic, weak (more generally electroweak) and the strong interactions. The mathematical formalism of the Standard Model is provided essentially by Quantum Field Theory, as a consequence of which, the former requires fundamental constants as input parameters as is required by any renormalisable QFT. But there are no particular constraints on the "constancy" of the fundamental constants over space-time. The idea that fundamental constants can vary with space and/or time was first put forward by Dirac in 1937 [66]. Considering the Standard model to be a complete description of atomic and sub-atomic interactions, any temporal and/or spatial variations in the fundamental constants would imply physical processes beyond the Standard Model.

The most precise measurement of the temporal variation of $\alpha$ from a single measurement was done by comparing clock transition frequencies of two independent atomic optical frequency standards, the $\mathrm{Al}^+$ ion and the $\mathrm{Hg}^+$ ion optical frequency standards at NIST, Boulder, putting a constraint of $(\frac{\dot{\alpha}}{\alpha})_{\mathrm{Al}^+/\mathrm{Hg}^+} = -1.6(2.6) \times 10^{-17}$ per year [67]. The same quantities were further measured at NPL in England and PTB in Germany by comparing frequencies of an $\mathrm{Yb}^+$ ion optical clock and a $^{133}\mathrm{Cs}$ atomic clock [68,69]. Combining results from these experiments (and a few others) has led to the constraint on time variation of $\alpha$ to be $\frac{\dot{\alpha}}{\alpha} = -0.7(2.1) \times 10^{-17}$/year (NPL) and $\frac{\dot{\alpha}}{\alpha} = -0.2(20) \times 10^{-17}$/year (PTB). However, these laboratory measurements of the time variation of $\alpha$ are limited to the current epoch. On cosmological time-scales, variation in the value of $\alpha$ can be deduced from observing absorption lines towards distant quasars, the light from which is studied using very large telescopes (at the W. M. Keck Observatory in Hawaii, USA and the VLT in Chile). The most precise limit on the variation of $\alpha$ from quasar data is $\frac{\Delta\alpha}{\alpha} = -1.42(0.55)_\mathrm{stat}(0.65)_\mathrm{sys} \times 10^{-6}$ from strong metal absorption system at redshift $z_{abs} = 1.1508$ in the quasar HE 0515-4414 [70]. Temporal variation of $\alpha$ is interesting to particle physicists and in particular for any proposed Grand Unified Theory (GUT). In simple terms, a GUT describes all the fundamental forces of nature in a single theory and the different forces would emerge from it due to symmetry breaking processes at various energy scales. A temporal variation of the fine-structure constant would imply temporal variations of the coupling constants of the other fundamental forces like the strong and the weak forces, or else a GUT would only be true at a particular point in time [71, 72]. Similar arguments can also be presented for spatial variations. Of particular interest in this regard for QCD is the time-variation of the proton-electron mass ratio $\mu_{\mathrm{pe}}$. A time-variation in $\Lambda_{QCD}$ would indicate a temporal variation in the QCD coupling constant and can be observed from a temporal variation of $\mu_{\mathrm{pe}}$ as $\Lambda_{QCD}$ does not influence the mass of the electron.

The temporal variation of $\mu_{\mathrm{pe}}$ has been constrained to $\frac{\Delta\mu_{\mathrm{pe}}}{\mu_{\mathrm{pe}}} = 0.0(1.0) \times 10^{-7}$ from comparing the transition frequencies of methanol in the quasar PKS1830-211 (redshift $z$=0.89) observed with a radio telescope and the same measured in the laboratory [73]. In the laboratory, a model independent constraint on the temporal variation of $\mu_{\mathrm{pe}}$ was obtained to be $\frac{\dot{\mu}_{\mathrm{pe}}}{\mu_{\mathrm{pe}}} = -3.8(5.6) \times 10^{-14}$/year from a comparison of a ro-vibrational transition frequency in $\mathrm{SF}_6$ and the fundamental hyperfine transition in $^{133}$Cs [74]. Further improvement on the time variation of $\mu_{\mathrm{pe}}$ was made by comparing optical transitions in $\mathrm{Yb}^+$ ion clock and $^{133}$Cs clock and a constraint of $(\frac{\dot{\mu}_{\mathrm{pe}}}{\mu_{\mathrm{pe}}})_{\mathrm{Yb}^+/\mathrm{Cs}^+} = -0.2(1.1) \times 10^{-16}$/year (NPL) and $(\frac{\dot{\mu}_{\mathrm{pe}}}{\mu_{\mathrm{pe}}})_{\mathrm{Yb}^+/\mathrm{Cs}^+} = -3.8(5.6) \times 10^{-14}$/year (PTB) was put [68, 69].

Spectroscopy of ro-vibrational transitions in hydrogen molecular ions with high precision and accuracy would lead to the development of molecular ion clocks, which have been proposed in Ref. [75] to be able to achieve a fractional frequency uncertainty $\sim 10^{-17}$. That would allow to put a more stringent constraint on the time variation of $\mu_{\mathrm{pe}}$. Such a molecular ion clock transition depends on $\mu_{\mathrm{pe}}$, which is fundamentally different from atomic optical clock transitions, which depend mainly on $\alpha$. A direct comparison between a molecular ion clock and an atomic optical clock for a considerable period of time would enable a direct study of temporal variation of $\mu_{\mathrm{pe}}$ and $\alpha$, thereby serving as a very sensitive probe for the Standard Model itself.

The search for physics beyond the Standard Model from hydrogen molecular ions (as well as the neutral hydrogen molecules $\mathrm{H}_2$ and $\mathrm{D}_2$) goes further. For example, a hypothetical "fifth force" may be proposed to exist between hadrons, which can be modelled as

$$V_5(r) \propto \alpha_5 \frac{\exp(-r/\lambda)}{r}, \tag{1.3}$$

where $\alpha_5$ is the coupling constant in analogy with the electromagnetic coupling constant $\alpha$ and $\lambda$ is the characteristic length scale of this interaction [76]. Owing to the simple structure of hydrogen molecular ions, the effects of this interaction $V_5(r)$ can be calculated very precisely. An experimental measure-

ment with sufficient accuracy would then allow to put a constraint on the length scale and strength of this fifth force. Till date, the most stringent constraint on the length scale and the interaction strength of the hypothetical fifth force has been provided by Biesheuvel *et al.* from an accurate measurement of $v : 0 \rightarrow 8$ vibrational overtone transition in $HD^+$ [33].
Another example is the effect of extra dimensions. In the theory of large extra dimensions proposed by Arkani-Hamed, Dimopoulos and Dvali (also known as the ADD theory) [77], it is argued that gravitation acts in its full force in dimensions higher than the three spatial dimensions in which the strong, weak and the electromagnetic interactions are described. Essentially this means that only a small part of the entire gravitational interaction is perceived in the three spatial dimensions. Presence of additional spatial dimensions would have to be in very small length scales or else would have been visible in experimental observations till now. This length scale is known as the "compactification radius" for the dimension concerned. Accurate calculations of the effects of these extra spatial dimensions on the ro-vibrational transition frequencies in hydrogen molecular ions can provide constraints on their strength and compactification radius [78, 79].

## 1.6 Vibrational spectroscopy of the $HD^+$ ion

Ro-vibrational transitions in $HD^+$ ions were first observed by Wing *et al.* [32] in the infrared in 1976. In their experiment, $HD^+$ ions in a beam were irradiated by an infrared $CO_2$ laser and transitions excited were detected by monitoring the change in cross-section of charge exchange between $HD^+$ and $H_2$ with vibrational levels. In that work, Wing *et al.* measured ro-vibrational transitions involving $v = 0...3, L = 0...3$ in the frequency range of 49.22 THz (1642 $\text{cm}^{-1}$) to 56.03 THz (1869 $\text{cm}^{-1}$) and determined the transition frequencies with a relative uncertainty of 1 ppm (0.001 $\text{cm}^{-1}$). Later in the 1980s and 1990s, Carrington and co-workers both measured and calculated several transitions in $HD^+$ [80–83]. The uncertainties of both the calculations and the measurements were $\sim$0.0001 $\text{cm}^{-1}$, and at that time provided the most stringent test of molecular theory. Uncertainty in the measurement of a ro-vibrational transition in $HD^+$ was improved to 2 ppb for the $(v, L) : (0, 2) \rightarrow (4, 3)$ vibrational overtone at 1.39 $\mu$m in 2007 [84]. This improvement in experimental accuracy was aided by the availability of better probe radiation sources, advent of techniques of sympathetic cooling of molecular ions by laser-cooled atomic ions. $HD^+$ ions were sympathetically cooled to translational temperatures of $\sim$10 mK by laser-cooled $Be^+$ ions in an ion trap, leading to much smaller first-order Doppler-broadening. The detection method employed in the later experiment was (1+1') resonance-enhanced multi-photon dissociation (REMPD),

which entails dissociating the ions excited by the probe laser to $v = 4$. The spectroscopic signal was formed by fractional loss of $\mathrm{HD}^+$ ions in the trap due to the REMPD process.
Uncertainty in the measurement of vibrational transitions in $\mathrm{HD}^+$ was further reduced to 1.1 ppb on the $(v, L) : (0, 0) \rightarrow (1, 1)$ transition by Bressel *et al.* in 2012 [85]. However, the experimentally measured transition frequency in this work was offset from the *ab initio* calculations by $2.5\sigma$. In 2016, spectroscopy on the $(v, L) : (0, 2) \rightarrow (8, 3)$ overtone was performed by Biesheuvel *et al.* [33, 86] with a relative frequency uncertainty of 1.1 ppb, however in this case agreeing with the theoretical calculations within the experimental uncertainty. This experiment is briefly discussed later (Chapter 2) in this thesis as it is the precursor to the experiment to be described in this work. In 2018, Alighanbari *et al.* performed Doppler-free spectroscopy in the Lamb-Dicke regime on a rotational transition at ∼1 THz in $\mathrm{HD}^+$ with a relative frequency uncertainty of $3.8 \times 10^{-10}$, which is till date the most precise measurement of a rotational transition in the hydrogen molecular ions [61]. The rotational transition measured by Alighanbari *et al.* in Ref. [61], although Doppler-free, is still more than one order of magnitude less precise than the *ab initio* calculation of ro-vibrational transition frequencies in $\mathrm{HD}^+$ [47]. To this end, a Doppler-free two-photon spectroscopy experiment on the $(v, L) : (0, 3) \rightarrow (9, 3)$ overtone was proposed in Ref. [87] by Tran *et al.*, the implementation of which is the main topic of discussion in this work.

## 1.7 Outline and summary of this thesis

This thesis describes the design, development and progress of an experiment towards Doppler-free two-photon spectroscopy of the $(v, L) : (0, 3) \rightarrow (9, 3)$ ro-vibrational transition in $\mathrm{HD}^+$ as proposed in Ref. [87]. Also some topics will be discussed which are closely related to the main experiment and were investigated by the author in the course of his tenure as a PhD student at Vrije Universiteit Amsterdam. The thesis is structured as follows:
**Chapter 2:** Recent advances in the *ab initio* calculations of energy level structure in hydrogen molecular ions are briefly mentioned. A brief summary of the measurement of the $v : 0 \rightarrow 8$ single-photon ro-vibrational transition in $\mathrm{HD}^+$ is presented and its results are discussed [33, 86]. The experimental setup used for this measurement is briefly described as the Doppler-free two-photon spectroscopy experiment described in this thesis is largely built upon it. The systematic shifts and uncertainties of the $v : 0 \rightarrow 8$ measurement are presented, which explains that the 1.1 ppb fractional frequency uncertainty achieved in this experiment is limited almost exclusively by the first-order Doppler broadening. Also discussed briefly are the results of Ref. [87], which are essential for

the design and realisation of the Doppler-free two-photon spectroscopy experiment.

**Chapter 3:** The experimental set up is described. Parts of the experimental set up were used to measure the $v : 0 \rightarrow 8$ vibrational overtone transition in HD$^+$ [33, 86] and have been described in more details elsewhere and hence discussed briefly. The spectroscopy laser system for probing the two-photon transition is extensively described together with its performance.

**Chapter 4:** The choice of hyperfine component of the $(v, L) : (0, 3) \rightarrow (9, 3)$ ro-vibrational transition to be measured is discussed on the basis of minimum net Zeeman shift and suppressed Doppler-broadened background, which are essential for a strong signal. An extended rate-equation model has been developed following the work of Biesheuvel *et al.* [33, 86] for modelling the expected two-photon spectrum. This model is useful for *a priori* determination of required experimental parameters such as appropriate laser detunings, optimum excitation duration and laser intensities, the experimental optimisation of which would be extremely tedious. The simulated two-photon lineshape can also be used to estimate shift in the estimation of the resonance frequency of the Doppler-free feature due to the Doppler-broadened background. The AC Stark shift induced by the dissociation laser at 532 nm and the cooling laser at 313 nm lasers as well as the Zeeman shift are discussed.

**Chapter 5:** "Ghost features" in Doppler-broadened ro-vibrational spectrum of trapped, laser-cooled HD$^+$ ions are discussed. These are features appearing in the Doppler-broadened single-photon spectrum in a finite sample of molecules (or atoms) with closely spaced components, the line profiles of which are partially overlapping due to first-order Doppler broadening. The example case of the $(v, L) : (0, 3) \rightarrow (4, 2)$ single-photon ro-vibrational transition of HD$^+$ has been studied. The ghost features are found to appear in the spectrum where there are no underlying hyperfine components of the ro-vibrational transition. The conditions in which these ghost features appear have been studied and their dependence on experimental parameters such as translational temperature of the sample molecules, finite number of the sample molecules, laser intensities and probe durations are extensively discussed and their implications indicated.

**Chapter 6:** A re-derivation of the proton-electron mass ratio $\mu_{\mathrm{pe}}$ from the existing spectroscopic measurements of ro-vibrational transitions in HD$^+$ in the light of CODATA-14 prescribed set of fundamental constants is presented. This has important consequences for the determination of the same constant from the Doppler-free two-photon experiment.

**Chapter 7:** The first observation of the $(v = 9)$ vibrational level in the ground electronic state of HD$^+$ is reported. Recent progress towards the observation and measurement of the Doppler-free two-photon ro-vibrational transition in HD$^+$ is presented. Some evidence has been presented towards the observation of the $(v, L) : (0, 3) \rightarrow (9, 3)$ Doppler-free two-photon transition.

**Chapter 8:** The thesis is concluded with the discussion of some prospects of the Doppler-free two-photon experiment in $HD^+$.

Chapter 2

# Necessary background information

## 2.1 Advances in *ab initio* calculations of the energy levels of HD$^+$

### 2.1.1 Summary of recent advances in the calculations of the ro-vibrational transition frequencies of HD$^+$

In this section, a condensed summary of the advances in the theoretical calculations of the ro-vibrational energy level structure of HD$^+$ in its ground electronic state are presented and the recent results mentioned (discussed in more detail in Sec. 6.2). The energy $E$ of a ro-vibrational level in the electronic ground state of the HD$^+$ molecular ion can be written as

$$E = R_\infty hc[E_{\mathrm{nr}}(\mu_{\mathrm{pe}}, \mu_{\mathrm{de}}) + \alpha^2 F_{\mathrm{QED}}(\alpha) + A_{\mathrm{p}}^{\mathrm{fs}} \left(\frac{r_{\mathrm{p}}}{a_0}\right)^2 + A_{\mathrm{d}}^{\mathrm{fs}} \left(\frac{r_{\mathrm{d}}}{a_0}\right)^2]. \tag{2.1}$$

In Eq. 2.1, $R_\infty$ and $\alpha$ are the Rydberg constant and the fine-structure constant, respectively, and $a_0$ is the Bohr radius. The main contribution to the total energy $E$ is from the non-relativistic energy $E_{\mathrm{nr}}$, which can be expressed as a function of $\mu_{\mathrm{pe}}$ and $\mu_{\mathrm{de}}$, which are the proton-electron and the deuteron-electron mass ratios, respectively. The non-relativistic part of the energy can be calculated with arbitrary precision (at least 16 digits) by solving the Schrödinger equation for the exact three-body Coulomb Hamiltonian as described in Ref. [88–91]. Calculations of the relativistic and radiative corrections to the non-relativistic energy, summarized by the term $\alpha^2 F_{\mathrm{QED}}(\alpha)$, have been improved over the years to the order of $m\alpha^7$. For a more thorough discussion of these calculations the reader is referred to Refs. [47, 92–95]. $A_\mathrm{p}^\mathrm{fs}\left(\frac{r_\mathrm{p}}{a_0}\right)^2$ and $A_\mathrm{d}^\mathrm{fs}\left(\frac{r_\mathrm{d}}{a_0}\right)^2$ are the leading-order nuclear-finite size corrections to $E$ due to the proton and deuteron charge radii $r_\mathrm{p}$ and $r_\mathrm{d}$ respectively. The coefficients $A_\mathrm{n}^\mathrm{fs}(\mathrm{n}=\mathrm{p},\mathrm{d})$ are proportional to the squared density of the wave function at the electron-nucleus coalescence point. Recent state-of-the-art theoretical calculations have revealed that currently the uncertainty in the calculated frequencies of the three accurately measured vibrational overtones in HD$^+$ (see Sec. 6.2) is $\sim 8\times10^{-12}$ in relative terms.

### 2.1.2 Hyperfine structure calculation

HD$^+$ has hyperfine structure associated with the spins of its constituents and the rotation of the molecule, and their respective magnetic interactions. In the experiment, we measure one (or two) hyperfine component(s) of the chosen ro-vibrational transition. Hence, an accurate knowledge of the hyperfine level energies is also imperative for an accurate measurement of the ro-vibrational transitions. Below, we state the effective spin hamiltonian in HD$^+$, the solution to which provides us with the hyperfine structure. The effective spin Hamiltonian can be written following Ref. [48] as

$$\begin{aligned}H_\mathrm{eff} =& E_1(\mathbf{L}\cdot\mathbf{s}_\mathrm{e}) + E_2(\mathbf{L}\cdot\mathbf{I}_\mathrm{p}) + E_3(\mathbf{L}\cdot\mathbf{I}_\mathrm{d}) + E_4(\mathbf{I}_\mathrm{p}\cdot\mathbf{s}_\mathrm{e})\\ &+ E_5(\mathbf{I}_\mathrm{d}\cdot\mathbf{s}_\mathrm{e})\\ &+ E_6\{2\mathbf{L}^2(\mathbf{I}_\mathrm{p}\cdot\mathbf{s}_\mathrm{e}) - 3[(\mathbf{L}\cdot\mathbf{I}_\mathrm{p})(\mathbf{L}\cdot\mathbf{s}_\mathrm{e}) + (\mathbf{L}\cdot\mathbf{s}_\mathrm{e})(\mathbf{L}\cdot\mathbf{I}_\mathrm{p})]\}\\ &+ E_7\{2\mathbf{L}^2(\mathbf{I}_\mathrm{d}\cdot\mathbf{s}_\mathrm{e}) - 3[(\mathbf{L}\cdot\mathbf{I}_\mathrm{d})(\mathbf{L}\cdot\mathbf{s}_\mathrm{e}) + (\mathbf{L}\cdot\mathbf{s}_\mathrm{e})(\mathbf{L}\cdot\mathbf{I}_\mathrm{d})]\}\\ &+ E_8\{2\mathbf{L}^2(\mathbf{I}_\mathrm{p}\cdot\mathbf{I}_\mathrm{d}) - 3[(\mathbf{L}\cdot\mathbf{I}_\mathrm{p})(\mathbf{L}\cdot\mathbf{I}_\mathrm{d}) + (\mathbf{L}\cdot\mathbf{I}_\mathrm{d})(\mathbf{L}\cdot\mathbf{I}_\mathrm{p})]\}\\ &+ E_9[\mathbf{L}^2\mathbf{I}_\mathrm{d}{}^2 - \frac{3}{2}(\mathbf{L}\cdot\mathbf{I}_\mathrm{d}) - 3(\mathbf{L}\cdot\mathbf{I}_\mathrm{d})^2].\end{aligned} \tag{2.2}$$

In Eq. 2.2, $\mathbf{L}$, $\mathbf{s}_\mathrm{e}$, $\mathbf{I}_\mathrm{p}$ and $\mathbf{I}_\mathrm{d}$ are the rotational, electron-spin, proton-spin and the deuteron-spin angular momenta, respectively. In $H_\mathrm{eff}$, the coefficients $E_n$ ($n = 1...9$) are numerical quantities which are found by averaging the Breit-Pauli Hamiltonian (which underlies the effective spin Hamiltonian of Eq. 2.2) over the spatial degrees of freedom [48]. As expected from the magnitude of their magnetic moments relative to those of the other HD$^+$ constituents, the proton-electron spin-spin interaction is the strongest one and sets the principal splitting of the rotational levels. The appropriate coupling scheme for the spin angular momentum is as below:

$$\begin{aligned}\mathbf{F} &= \mathbf{I}_{\mathrm{p}} + \mathbf{s}_{\mathrm{e}},\\ \mathbf{S} &= \mathbf{F} + \mathbf{I}_{\mathrm{d}},\\ \mathbf{J} &= \mathbf{L} + \mathbf{S}.\end{aligned}$$

With the spin quantum numbers given by $s_{\mathrm{e}} = 1/2$, $I_{\mathrm{p}} = 1/2$, and $I_{\mathrm{d}} = 1$, this coupling scheme implies that the hyperfine structure has 4 components for $L = 0$, 10 components for $L = 1$ and 12 components for $L \geq 2$. Below, in Fig. 2.1, the hyperfine structure for a rotational level with $L \geq 2$ for HD$^+$ is shown.

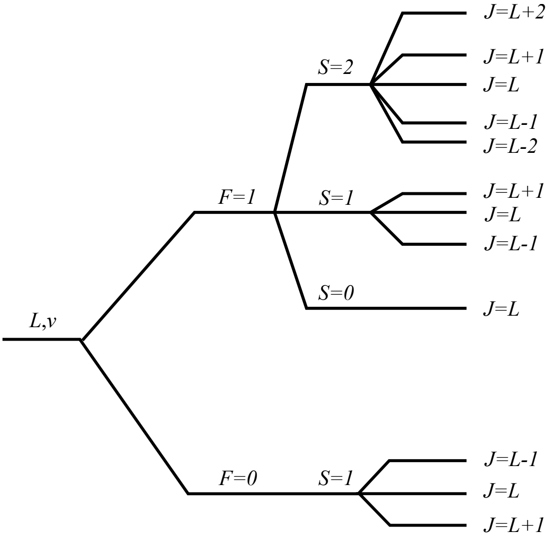

**Figure 2.1:** Schematic of the hyperfine structure of a rotational level with $L \geq 2$ in HD$^+$.

## 2.2 Summary of spectroscopy of the $(v, L) : (0, 2) \rightarrow (8, 3)$ overtone in HD$^+$

In 2016, at Vrije Universiteit Amsterdam, spectroscopy on the $(v, L) : (0, 2) \rightarrow (8, 3)$ overtone was performed by Biesheuvel *et al.* [33, 86]. This experiment is the precursor to the Doppler-free two-photon spectroscopy experiment to be described in detail in this thesis. Hence, at this point it is useful to briefly review the experimental setup, methods and results of this experiment, also because these played an important role in the design of the two-photon experiment. A more detailed description of the setup used for the $(v, L) : (0, 2) \rightarrow (8, 3)$ spectroscopy can be found in Refs. [33, 86, 96, 97].

About 750 $Be^+$ ions are laser-cooled to form a Coulomb crystal with "secular temperature" ∼10 mK in a segmented linear Paul trap. The cooling radiation at 313 nm is generated by the second harmonic of 626 nm light from a Spectra Physics 380D ring-dye laser pumped by a solid state Nd:$YVO_4$ laser at 532 nm. Second harmonic of the 626 nm light was produced by a BBO crystal in a bow-tie enhancement cavity. $HD^+$ ions are generated in the trap by leaking in neutral HD gas into the trap while bombarding them with ∼200 eV electrons, leading to electron-impact ionisation. 40-85 $HD^+$ ions are sympathetically cooled by the crystal of ∼750 $Be^+$ ions. The $(v, L) : (0, 2) \rightarrow (8, 3)$ overtone was excited by a continuous-wave titanium:sapphire (Ti:S) laser at 782 nm directed along the ion-trap axis. The Ti:S laser was frequency locked to an optical frequency comb (OFC) laser (Menlo Systems GmbH, FC1500), referenced to a GPS disciplined rubidium atomic clock, to provide absolute frequency calibration. The transition was detected by selectively dissociating the $HD^+$ molecules excited to the $(v = 8, L = 3)$ manifold using a 532 nm laser (resonance enhanced multi-photon dissociation, REMPD). The dissociation light was obtained by splitting off part of the pump laser. The spectroscopic signal was derived from the fractional loss of $HD^+$ ions due to the REMPD process, which can be represented as

$$S(t) = f_{\mathrm{NL}} \left( \frac{N_{\mathrm{HD}^+}(0) - N_{\mathrm{HD}^+}(t)}{N_{\mathrm{HD}^+}(0)} \right). \tag{2.4}$$

In Eq. 2.4, $N_{\mathrm{HD}^+}(0)$ and $N_{\mathrm{HD}^+}(t)$ represent the number of $HD^+$ ions in the trap before and after a REMPD duration of $t$ seconds. As detailed in Ref. [86], $f_{\mathrm{NL}}$ is a nonlinear function which deviates only slightly from the function $f(x) = x$, and which accounts for the nonlinearity in the determination of $N_{\mathrm{HD}^+}$ obtained by the so-called method of "secular excitation" [84]. In this method, the radial centre-of-mass (COM) mode of motion of the $HD^+$ ions is excited by a radio-frequency wave whose frequency is (nearly) resonant with the COM motional mode. The motionally excited $HD^+$ ions consequently excite the motion of the surrounding laser-cooled $Be^+$ ions, thereby heating them and causing a change in the Doppler width of the 313 nm $Be^+$ cooling transition. Since the 313 nm laser frequency is red detuned from the $Be^+$ transition frequency, this leads to a visible change in the 313 nm fluorescence level. The frequency of the secular excitation electric field was scanned over the $HD^+$ motional resonance (600. . .850 kHz) to generate a fluorescence profile which was recorded by a photomultiplier tube (PMT) and a photon counting system. The area under this fluorescence curve is proportional (although not linearly [86]) to the number of HD$^+$ ions in the ion-trap. In Fig. 2.2, such a fluorescence spectrum due to secular excitation is presented.

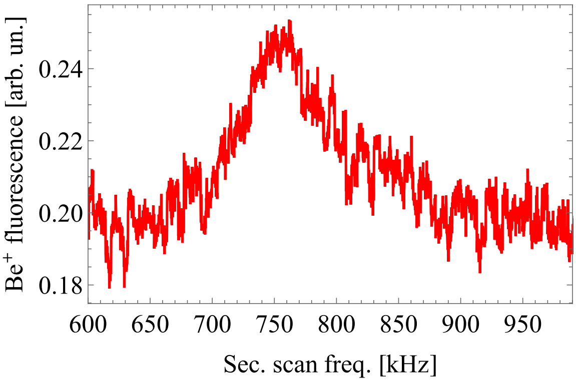

**Figure 2.2:** A typical secular excitation spectrum (resulting from a 10 s linear frequency sweep) of sympathetically cooled HD$^+$ ions in a Coulomb crystal of laser-cooled Be$^+$ ions.

In the manner described above, a spectrum was obtained by stepping the probe laser over a frequency range of ~250 MHz about the theoretically calculated "spin-averaged" frequency of the $(v, L) : (0, 2) \rightarrow (8, 3)$ ro-vibrational transition, which is wide enough to address the strongest 25 hyperfine components of the ro-vibrational transition. In total, 1772 data points were recorded for 10 s REMPD duration each, and the experimentally recorded spectrum is shown in Fig. 2.3. As can be observed in Fig. 2.3, the recorded spectrum is Doppler broadened, so that clusters of hyperfine transitions merge together to produce an asymmetric spectrum with only partially resolved hyperfine structure. Hence to extract the spin-averaged ro-vibrational transition frequency of the $(v, L) : (0, 2) \rightarrow (8, 3)$ overtone, a lineshape model was developed which captured the aspects of hyperfine structure, HD$^+$ rotational population redistribution under the influence of blackbody radiation (BBR), Doppler broadening and the non-linear secular excitation signal. The core of this line-shape model embodied a set of rate equations in which the interactions of the HD$^+$ ions with the probe and dissociation lasers as well as ambient BBR at 300 K were described by Einstein's $B$ coefficients. Spontaneous emission was described by Einstein's $A$ coefficients, which were computed as explained in Ref. [86]. Other physical parameters such as laser intensity $I_{\mathrm{L}}$, HD$^+$ ion secular temperature $T_{\mathrm{HD}^+}$, average Be$^+$ ion secular temperature $T_0$ , and probe laser frequency $\nu$

were used which reflected the experimental conditions. Values of these physical parameters were independently obtained where possible, or treated as fit parameters in the spectral lineshape fit procedure. For an extensive and rigorous description of the rate equation model, the reader is referred to Refs. [33, 86]. However, for the sake of completeness, a very brief description of the rate equation model used to model the experimental $(v, L) : (0, 2) \rightarrow (8, 3)$ ro-vibrational spectra is presented here.

At 300 K (i.e. slightly above room temperature), 97.6% of the $HD^+$ ion population can be found in rotational levels with $v = 0, L = 0...5$. Each of these rotational levels possesses hyperfine structure. The rate equation started out from a state vector $\rho(t)$ describing the population of the 62 hyperfine levels of the $v = 0, L = 0...5$ manifold. Subsequently, the rate equations are applied to form a set of coupled differential equations, which capture the dynamics of the ion population interacting with the different lasers and BBR. Other parameters affecting the spectrum, such as non-linear dependence of the secular excitation spectrum with $N_{\mathrm{HD}^+}$, and the absolute number of $HD^+$ ions in the trap, were deduced and incorporated with the help of molecular dynamics (MD) simulations. Zeeman shifts due to magnetic field were not considered in the lineshape model as the shifts at the typical operating magnetic field of 1.9 G is much smaller than the Doppler-broadened linewidth implying that all the Zeeman components are addressed simultaneously by the probe laser. The set of coupled differential equations were solved by the `NDSolve` algorithm of *Mathematica*. The simulated spectroscopic signal is then given by

$$S_{\mathrm{sim}}(t) = f_{\mathrm{NL}}\left(\frac{\rho(0) - \rho(t)}{\rho(0)}\right). \tag{2.5}$$

As a matter of fact, the nonlinear function $f_{\mathrm{NL}}$ is not only dependent on the fractional loss of $HD^+$ ions, but also on the $Be^+$ temperature, $T_0$, reached during secular excitation [86]. The value of $T_0$ is typically ∼3 K, and can be found from MD simulations or from a fit to the experimental spectrum. The function $f_{\mathrm{NL}}$ itself was found by combining the velocity distributions obtained from MD simulations of the secular excitation with the velocity-dependent $Be^+$ 313 nm scattering rate function [86]. To obtain a smooth, continuous lineshape function for fitting the experimental spectrum, $S_{\mathrm{sim}}(t)$ was computed on a dense grid of values of $I_{\mathrm{L}}$, $T_{\mathrm{HD}^+}$, $\nu$ and interpolated to generate a smooth function

$$S_{\mathrm{sim}}(t) = S_{\mathrm{sim}}(\nu - \nu_{0,\mathrm{fit}}, T_{\mathrm{HD}^+}, I_{\mathrm{L}}, T_0, t) \tag{2.6}$$

In Eq. 2.6, $\nu_{0,\mathrm{fit}}$ corresponds to the fitted spin-averaged frequency of the $(v, L) : (0, 2) \rightarrow (8, 3)$ ro-vibrational transition.

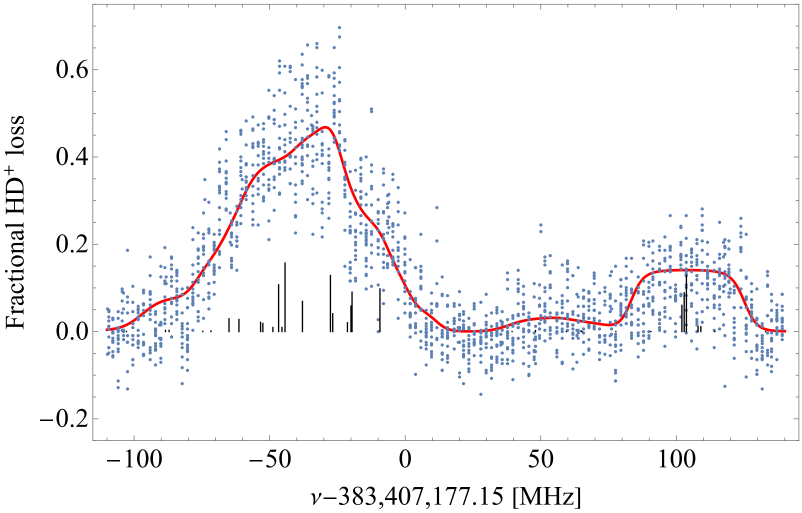

**Figure 2.3:** The experimentally recorded spectrum of the $(v, L) : (0, 2) \rightarrow (8, 3)$ ro-vibrational transition of HD$^+$ plotted with the fitted lineshape function (red solid curve), as well as the location and strength of the underlying hyperfine components (most of which are unresolved). Figure reproduced from Ref. [86].

Frequency shifts due to systematic effects such as the Zeeman effect, the AC Stark effect due to the probe and dissociation lasers, and the second-order Doppler effect were also estimated. After correcting for these systematic shifts, a value of $\nu_{0,\mathrm{expt}} = 383,407,177.38(41)$ MHz was determined for the spin-averaged frequency of the $(v, L) : (0, 2) \rightarrow (8, 3)$ ro-vibrational transition. The size and corresponding uncertainties of the various systematic and statistical sources of error are presented in Table 2.1. The experimentally determined frequency agrees well with the more accurate theoretical value $\nu_{0,\mathrm{theo}} = 383,407,177.150(15)$ MHz[1] [94].

The largest contribution to the 1.1 ppb relative uncertainty of the experiment stems from first-order Doppler broadening, as this forms the limiting factor in the first four entries of Table 2.1 [86]. A natural step forward towards higher precision in spectroscopic study of HD$^+$ ro-vibrational transitions would be suppressing the first-order Doppler-broadening. Hence, an experiment towards Doppler-free two-photon spectroscopy of HD$^+$ ions was conceived and designed to be performed in the existing ion-trap setup. The rest of this thesis will

---

[1] The theoretical value presented in Ref. [94] used the CODATA-10 recommendations of fundamental constants. For an updated value of the calculated frequency using CODATA-14, see Table 6.1 in Sec. 6.2 [60].

| Origin | Shift | Uncertainty | |
|---|---|---|---|
| | (MHz) | (MHz) | (ppb) |
| Resolution (statistical fit error) | 0 | 0.33 | 0.85 |
| Doppler effect due to chemistry | −0.25 | 0.25 | 0.66 |
| Ignoring population of $L = 6$ in rate equations | 0 | 0.032 | 0.083 |
| Doppler effect due to micromotion | −0.055 | 0.020 | 0.052 |
| Frequency measurement | 0 | 0.010 | 0.026 |
| BBR temperature | 0 | 0.005 | 0.013 |
| Zeeman effect | −0.0169 | 0.003 | 0.008 |
| Stark effect | −0.0013 | 0.0001 | 0.0004 |
| Electric-quadrupole shift | 0 | 0.0001 | 0.0003 |
| Second-order Doppler shift | 0 | 0.000005 | 0.00001 |
| Total | −0.0182 | 0.41 | 1.1 |

**Table 2.1:** Systematic shifts and uncertainty budget of the single-photon spectroscopy of the $(v, L) : (0, 2) \rightarrow (8, 3)$ rovibrational transition. Table reproduced from Ref. [33].

mainly focus on the design and implementation of such a Doppler-free two-photon spectroscopy experiment.

## 2.3 Doppler-free two-photon spectroscopy of ro-vibrational transitions of HD$^+$

### 2.3.1 Feasibility study

The possibility of performing a Doppler-free two-photon spectroscopy experiment of ro-vibrational transitions in trapped HD$^+$ ions in the existing ion trap setup at Vrije Universiteit Amsterdam was comprehensively investigated in Ref. [87] by Tran *et al.* As the findings of this article are fundamental for the design of the two-photon experiment, the methods and results of Ref. [87] are discussed briefly together with their implications for the setup at Vrije Universiteit Amsterdam.

The idea for Doppler-free spectroscopy studied in Ref. [87] is to achieve the so-called "Lamb-Dicke regime", in which the effective wavelength of the probe radiation is considerably larger than the motional amplitude of the trapped ions, thereby suppressing the first-order Doppler broadening. The basic idea underlying the present two-photon spectroscopic scheme consists in making two-photon transitions in a three-level ladder system, driven by two lasers of approximately the same wavelength but with opposite directions. For such a system, the effective wave vector equals the difference of the two individual wave vectors, which from the viewpoint of the HD$^+$ ion corresponds to the interaction with a single optical electric field with very large wavelength. This feature enables driving optical transitions deep inside the Lamb-Dicke regime (i.e. first-order Doppler free). The required counter propagating laser beams can be readily introduced along the trap symmetry axis of the experimental apparatus, which was also used for the cooling, spectroscopy and dissociation lasers for the $(v, L) : (0, 2) \rightarrow (8, 3)$ spectroscopy.

HD$^+$ has a small permanent electric dipole moment, which leads to weak vibrational overtones. A two-photon transition in a system whose single-photon transitions are weak will generally suffer from impractically small transition rates at typical, experimentally accessible laser intensities. However, a weak two-photon transition can be driven more efficiently by using a quasi-resonant intermediate level. The challenge therefore is to find a two-photon transition which has an intermediate level very nearly halfway in between the ground and excited energy levels. To find these, a software search algorithm was developed to analyse the extensive set of HD$^+$ ro-vibrational energy levels based on accurate calculations of ro-vibrational energy levels in HD$^+$ computed by Moss [46], thus looking for intermediate levels leading to small enough energy mismatch leading to a large enough effective wavelength of the probe radiation. The algorithm revealed a number of suitable two-photon transitions, of which the $(v, L) : (0, 3) \rightarrow (4, 2) \rightarrow (9, 3)$ at a single-photon wavelength of 1.44 $\mu$m turned out to be the most convenient one owing to the availability of commercial off-the-shelf radiation sources (with sufficient optical output power) in the form of diode lasers, optics, and reference frequency standards (in the form of a caesium-clock-referenced OFC laser and a Hz-linewidth laser already available in the laboratory).

In Ref. [87], several of the parameters considered are usual daily operational parameters of the ion-trap setup at Vrije Universiteit Amsterdam [96,98], for example the assumption of 100 HD$^+$ ions which are trapped and sympathetically cooled to ∼10 mK secular temperature by a crystal of ∼1000 laser-cooled Be$^+$ ions. The spectroscopic scheme employed is $(1 + 1' + 1")$ REMPD, where the probe radiation fields excite the HD$^+$ ions from $(v = 0, L = 3)$ to $(v = 9, L = 3)$ via the intermediate level $(v = 4, L = 2)$. The ions which are excited to the $v = 9$ vibrational manifold are efficiently dissociated within their radiative lifetime by a laser running at 532 nm. The frequencies of the probe radiation addressing the $(v, L) : (0, 3) \rightarrow (4, 2)$ transition (with resonant frequency $\omega_{12}$) and the $(v, L) : (4, 2) \rightarrow (9, 3)$ transition (with resonant frequency $\omega_{23}$) are 207.838 THz (denoted as $\nu = \frac{\omega}{2\pi}$) and 204.427 THz ($\nu' = \frac{\omega'}{2\pi}$), respectively with an energy mismatch of ∼410 GHz (relative energy mismatch: 0.05 % of the total transition frequency). The natural linewidths of the considered rovibrational levels are 37 mHz, 9.2 Hz and 13.1 Hz for $(v, L) : (0, 3)$, $(4, 2)$ and $(9, 3)$ respectively. The effective linewidth of the $(v = 9, L = 3)$ state, however, can be significantly broadened by the dissociation laser in order to have efficient dissociation. As in previous work, the spectroscopic signal is formed by considering the fractional loss of HD$^+$ ions in the trap due to the REMPD process.

Each of the ro-vibrational levels considered here has a hyperfine structure spread out over a frequency range of ∼1 GHz, as described in Sec. 2.1.2 [48]. Ref. [87] provides a selection of preferable hyperfine components to be probed. The selection criterion used in [87] is the net Zeeman shift of the two-photon transition. This is a critical issue in HD$^+$ which, being an open-shell molecule, exhibits large Zeeman shifts in transitions between states with different hyperfine quantum numbers. However, the two-photon transition allows selecting transitions between levels with homologous spin states (identical $F$, $S$ and $J$ quantum numbers) in the ground and the upper ro-vibrational levels, for which a large common-mode cancellation of the Zeeman effect occurs. The resulting net Zeeman shifts and splittings are smaller than the spectral linewidths of the transtion, allowing the Zeeman effect to be ignored in the four-level optical Bloch equation (OBE) model of Ref. [87].

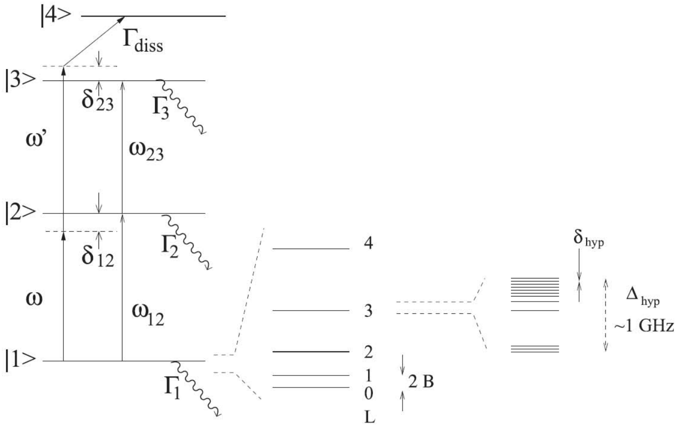

**Figure 2.4:** Partial energy level diagram showing the frequencies of the radiation fields relative to the single-photon transition frequencies, the spontaneous decay rates, and the four energy levels involved in the OBE model is shown in the left. In the centre, a schematic of the rotational states of $|1\rangle$ is shown, and on the right the hyperfine structure of a single rotational state is shown. Figure taken from Ref. [87].

If the trapped HD$^+$ ions are excited by counter-propagating laser beams along the trap axis, the effective wavelength of the transition becomes $\lambda_{\text{eff}} = \frac{2\pi c}{\omega_{12}-\omega_{23}}$ ($\sim$700 $\mu$m), which is large compared to the motional amplitude $a$ ($\sim$1 $\mu$m) along the trap axis. This leads to a Lamb-Dicke parameter $\eta = \frac{a}{\lambda_{\text{eff}}} \approx 0.014$, which is much smaller than 1, leading to suppression of first-order Doppler-broadening.

The dynamics of the interaction of the molecular levels with the probe and dissociation lasers is described by a set of four-level Optical Bloch equations. The ro-vibrational states $(v, L)$ : $(0, 3)$, $(4, 2)$ and $(9, 3)$ (henceforth denoted by $|1\rangle$, $|2\rangle$ and $|3\rangle$, respectively) interact with the probe radiation fields with optical frequencies $\omega$ and $\omega'$ coherently. The upper state $|3\rangle$ interacts incoherently and irreversibly with the dissociation laser to transfer population to another state $|4\rangle$ which represents the dissociated level. The simulation of the REMPD dynamics through the OBE model takes into account the ion motions obtained from a MD simulation involving 20 HD$^+$ ions, sympathetically cooled by 400 Be$^+$ ions. Ambient BBR radiation at 300 K redistributes population among the rotational levels in the $v = 0$ manifold. However, the redistribution of population due to BBR is much slower than that of the probe and dissociation radiations and hence not considered in the OBE model. Spontaneous emission is introduced in the OBE model phenomenologically.

The spectroscopic two-photon signal is the sum of two distinct contributions, namely the signal due to sequential excitations (i.e. one absorption of a first photon at frequency $\omega$, followed by a second, later absorption of a photon at frequency $\omega'$), and a signal due to direct two-photon excitation. The sequential path essentially involves two single-photon transitions and therefore leads to a Doppler-broadened signal, whereas the signal due to the direct path is Doppler-free (on top of the Doppler-broadened background). One of the main objectives of the study in Ref. [87] was to determine proper frequency detunings of the probe radiation fields so as to achieve a large signal-to-background ratio for the Doppler-free two-photon signal. The OBE simulations furthermore assumed Rabi frequencies $\Omega_{12} = \Omega_{23} = 2\pi \times 5$ kHz, which is achievable using narrowband commercial diode laser systems. The dissociation rate was taken to be $\Gamma_{\text{diss}} = 200\ \text{s}^{-1}$, which is also practically achievable. The OBEs were numerically solved using a fourth-order Runge-Kutta method with time steps of $1 \times 10^{-9} \ldots 5 \times 10^{-8}$ s to capture the relevant dynamics.
For the doubly resonant condition of $\omega = \omega_{12}$ and $\omega' = \omega_{23}$, the Doppler-free two-photon signal is expected to be largest. However, because the detuning $\delta_{12} = \omega - \omega_{12}$ of the laser addressing the $v : 0 \rightarrow 4$ transition in the doubly resonant condition is less than $\Gamma_{\text{D}}$, the single photon Doppler width of the transition, significant population is transferred to the $|2\rangle$ level. Consequently, the population in $|2\rangle$ is excited by the laser addressing $v : 4 \rightarrow 9$ and gets dissociated. As pointed out above, this process is Doppler-broadened because of the velocity distribution of the trapped $HD^+$ ions and competes with the Doppler-free two-photon transition. Hence, it is imperative to increase $\delta_{12}$ such that population transfer to the intermediate level is minimised. Increasing $\delta_{12}$ suppresses the sequential Doppler-broadened transitions, and at the same time the Doppler-free two-photon signal gains visibility. At the same time, however, the two-photon transition rate scales with the inverse square of the intermediate detuning $\delta_{12}$ [87]. Therefore, the optimal value of $\delta_{12}$ would be slightly larger than $\Gamma_{\text{D}}$ to efficiently suppress the Doppler-broadened sequential two-photon excitations, while minimising the reduction of the two-photon transition rate due to the non-zero intermediate detuning. A more detailed discussion about the choice of detuning $\delta_{12}$ to be used in the experiment will be presented in Chapter 4 (Sec. 4.3). In Fig. 2.5, the expected Doppler-free two-photon signal is plotted against $\delta_{23}$ for different values of $\delta_{12}$, confirming the assertion made above for the optimal choice of $\delta_{12}$.

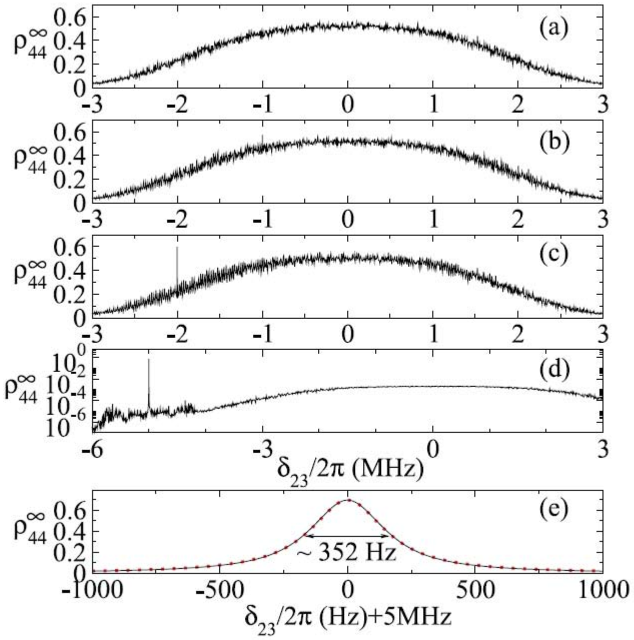

**Figure 2.5:** The expected two-photon signal plotted for different values of $\delta_{12}$: (a) 0 MHz, (b) -1 MHz, (c) -2 MHz, (d) -5 MHz. Panel (e) provides a high-resolution view of the direct two-photon excitation signal of (d). It is clearly observed that for $\delta_{12} \geq \Gamma_{\mathrm{D}}$, the Doppler-free signal is prominently visible on top of the suppressed Doppler-broadened background. Figure taken from Ref. [87].

The adverse effect of an increased intermediate detuning $\delta_{12}$ on the two-photon transition rate can be ameliorated by increasing the intensity of the two probe radiation fields. However, this will lead to increased power broadening. A trade off can be made between the signal-to-background ratio and power broadening such that the experimental accuracy still exceeds the theoretical accuracy of the spin-averaged frequency of the $(v, L) : (0, 3) \rightarrow (9.3)$ ro-vibrational transition.

Frequency shifts due to systematic effects, the most prominent of which being the Zeeman and AC Stark shifts due to the various electromagnetic fields present at the location of the HD$^+$ ions are expected to be determined with an uncertainty below 1 kHz. A more detailed analysis will also be presented later in Chapter 4 (Sec. 4.4) for an estimate of AC Stark shifts induced by the cooling and dissociation lasers. For the spectroscopy lasers with frequencies $\omega$ and $\omega'$, an estimate of the AC Stark shift (or "light shift") $\Delta_{LS}$ can be obtained from Eq. 2.7 (Equation 10 in Ref. [87])

$$\Delta_{LS} = \frac{\Omega_{23}^2 - \Omega_{12}^2}{\delta_{12}}. \tag{2.7}$$

Eq. 2.7 is valid near the two-photon resonance at $\delta_{12} = -\delta_{23}$. Hence by controlling the spectroscopy laser intensities, $\Omega_{12}$ and $\Omega_{23}$ can be matched to suppress the AC Stark shift due to the spectroscopy lasers. For the range of experimental parameters considered by Ref. [87], $\Delta_{LS}$ is limited to values in the range (-1 kHz, 1 kHz).

Probing along the trap axis minimises the effect of micromotion, which causes sidebands at the radio-frequency (rf) drive frequency of the ion trap (~13.2 MHz). However, with the Lamb-Dicke parameter $\eta \approx 0.014$, the sidebands will be both strongly suppressed as well as located far away from the carrier, so that for all practical reasons, they can be assumed to have a negligible effect on the lineshape of the Doppler-free two-photon signal. The second-order Doppler shift was estimated to amount to $\sim 10^{-14}$ in relative frequency terms, which is well within the target accuracy of the present experiment.

One remaining essential aspect of the envisaged two-photon spectroscopy is linewidth broadening due to laser frequency noise. As a matter of fact, laser frequency noise might lead to laser linewidths of the order of Rabi frequencies induced by the probe radiation fields, which in turn would affect the two-photon transition rate. Hence, laser frequency noise was incorporated into the OBE model in order to study the dependence of the two-photon transition rate $\Gamma_{\mathrm{2ph}}$ the laser linewidth. Furthermore, an analytical expression for $\Gamma_{\mathrm{2ph}}$ was derived which is valid in the "large $\delta_{12}$" ($\delta_{12} > \Gamma_{\mathrm{D}}$) limit:

$$\Gamma_{\mathrm{2ph}} = \frac{\Omega_{12}^2 \Omega_{23}^2}{\delta_{12}^2} \frac{\Gamma_3^{\mathrm{eff}} + 2\Gamma_{\mathrm{FWHM}}}{\delta_{13}^2 + \frac{(\Gamma_3^{\mathrm{eff}} + 2\Gamma_{\mathrm{FWHM}})^2}{4}}. \tag{2.8}$$

In Eq. 2.8, $\delta_{13}$ is the detuning of the sum of the probe laser frequencies from the two-photon resonance frequency, $\Gamma_3^{\mathrm{eff}}$ stands for the combined spontaneous emission and dissociation rates of the upper state $|3\rangle$, and $\Gamma_{\mathrm{FWHM}}$ is the linewidth of each probe laser, taken to be equal for both. For sufficiently large values of $\delta_{12}$, the results of the full OBE model and of Eq. 2.8 are in good agreement. This is visible in Fig. 2.6, which shows $\Gamma_{\mathrm{2ph}}$ as a function of $\Delta_{\mathrm{FWHM}}$, computed using both methods, for $\delta_{12}$ equal to the Doppler width. The effect of BBR-induced population redistribution among the various rotational levels of the ground vibrational manifold becomes important for REMPD durations of more than 1 s. This phenomenon will prove instrumental to achieving sufficiently high REMPD signals. For example, at typical ambient temperatures of ~300 K, 97.6 % of the $HD^+$ population is in the rotational levels $L = 0...5$,

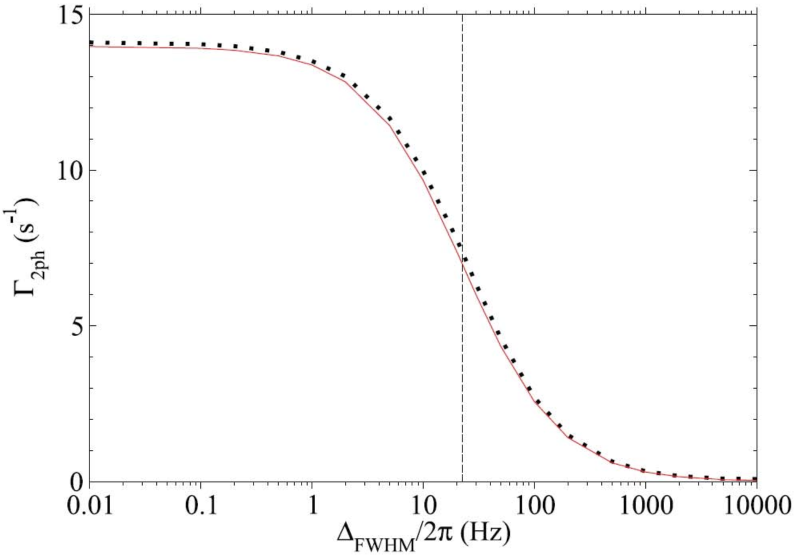

**Figure 2.6:** The Doppler-free two-photon transition rate $\Gamma_{2\text{ph}}$ is plotted plotted as a function of the linewidth of the spectroscopy lasers. The black dots represent the results from the solution of the OBEs and the red curve represents the result from Eq. 2.8. Figure taken from Ref. [87].

distributed over 62 hyperfine states in total. The population in a target hyperfine state might therefore be as low as 1-2%, and the maximum REMPD signal would be limited to a similarly small value. Owing to the redistribution of population by BBR, however, the target state population will be replenished, leading to an enhancement of the signal. In Ref. [87] this is modelled as follows. Since the interaction of the rotational states with the BBR field is incoherent, and treating also the REMPD process as an incoherent process (assuming that REMPD takes place at a much higher rate than BBR-induced transitions), the rotational-state dynamics can be described using rate equations. The two-photon signal $s(t)$ is defined to be

$$s(t) = \frac{\sum_{\alpha,L} \rho_{\alpha L}(0) - \rho_{\alpha L}(t)}{\sum_{\alpha,L} \rho_{\alpha L}(0)}. \tag{2.9}$$

In Eq. 2.9, $\rho_{\alpha L}(0)$ is the population in the hyperfine levels of a rotational level $L$ with a set of quantum numbers represented by $\alpha \equiv (F, S, J)$ at time $t = 0$. $\rho_{\alpha L}(t)$ represents the population of the chosen hyperfine level in rotational level

$L$ after a REMPD duration of $t$. For example, in Fig. 2.7, the signal $s(t)$ is plotted against REMPD durations from 1 ms to 1000 s for REMPD of the hyperfine state with quantum numbers $(L, F, S, J) = (3, 1, 2, 5)$. The choice of this hyperfine level will be explained later in this work.

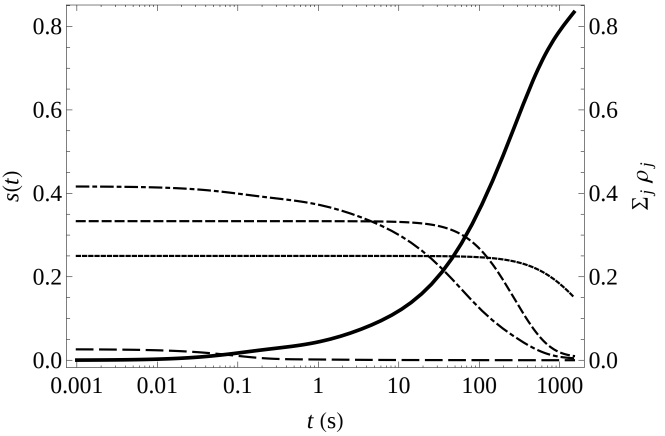

**Figure 2.7:** The expected signal $s(t)$ is plotted against probe duration for different hyperfine levels. The solid black line is for the hyperfine component starting with $(F, S, J) = (1, 2, 5)$ of the $(v, L) = (0, 3)$ ro-vibrational manifold. The other curves show the depletion of the total population in ro-vibrational states summed over certain subgroups of rotational and hyperfine states: long-dashed curve, population in $(L, F, S, J) = (3, 1, 2, 5)$; dash-dotted curve, sum over $L$, $J$ of all population in states with $F = 1$, $S = 2$; short-dashed curve, sum over $L$, $S$, $J$ of all population in states with $F = 1$, $S = 0, 1$ (but not $S = 2$); dotted curve, sum over $L$, $S$, $J$ of all population in states with $F = 0$. Graph taken from Ref. [87].

### 2.3.2 Limitations of the OBE model

The thorough study performed by Tran *et al.* in Ref. [87] still has some simplifying assumptions. To apply the results to the actual experimental design, these limitations need to be identified and adapted appropriately. These limitations will be addressed in the following paragraphs.

One simplifying assumption made in this study is that the chosen hyperfine substates of the relevant ro-vibrational states are sufficiently isolated, i.e. the interaction dynamics with the different radiation sources to be used in the experiment can be modelled by a set of four-level OBEs. However, the strongest hyperfine components of a typical vibrational overtone transition in HD$^+$ are densely packed in the main lobes of the hyperfine spectrum, as can be seen in Fig. 2.8. The problem it poses is that at 10 mK secular temperature of

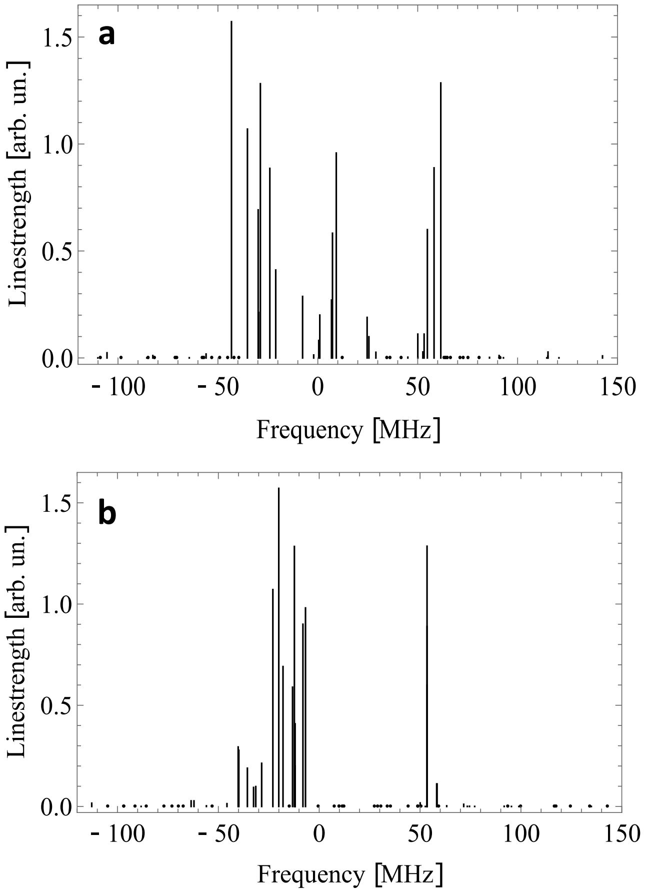

**Figure 2.8:** Theoretical hyperfine structure of the $(v, L) : (0, 3) \rightarrow (4, 2)$ (a) and $(v, L) : (4, 2) \rightarrow (9, 3)$ (b) transitions.

the trapped $HD^+$ ions, the Doppler-profiles of the adjacent components of the hyperfine spectra of both $(v, L) : (0, 3) \rightarrow (4, 2)$ and $(v, L) : (4, 2) \rightarrow (9, 3)$ transitions overlap. This implies that some of the hyperfine components of interest are insufficiently isolated (or partially Doppler-resolved) to apply the results of the four-level OBE model. At the same time, solving the OBE for all 24 pertinent hyperfine states involved would pose a formidable (if not intractable) computational task (in particular if magnetic substates are treated separately too, which would increase the number of states in the OBE by another factor of seven). In spite of this, a number of suitable hyperfine components were identified following qualitative arguments given in Ref. [58]. A simpler, but faithful representation of the expected spectrum can be obtained by an extension of the rate equation model developed by Biesheuvel *et al.* [33, 86]. As described later in Chapter 4, this allows a meaningful assessment of the suitability of the lines identified by Karr *et al.* in Ref. [58], and the feasibility of the proposed two-photon spectroscopy as a whole.

## Chapter 3

# Experimental setup

## 3.1 Laser-cooling of $Be^+$ ions and the ion trap setup

### 3.1.1 Ion trap setup

Charged particles like atomic or molecular ions can be localised in space in ion traps. Confining the sample atoms or molecules in space allows for a plethora of advantages in the field of spectroscopy. As an example, for atomic ions, spatial localisation allows for efficient cooling of their translational motion using laser-cooling [99], leading to reduction of first-order Doppler broadening. The sample of interest in this experiment is $HD^+$, which cannot be laser-cooled. Nevertheless, $HD^+$ ions can be sympathetically cooled by laser-cooled atomic ions such as $Be^+$ by confining them in the same space [100]. Cooling the translational motion of the $HD^+$ ions leads to low velocities of the ions. Ion traps, when installed in ultra-high vacuum, allow for long storage times (of few days) of the trapped species with minimal external perturbations, leading to long interrogation times, which is desirable for high-precision spectroscopy.

The Earnshaw's theorem dictates that electrostatic fields alone cannot trap a charged particle in free space [101]. However, a static electric field in conjunction with a static magnetic field (Penning trap) can be used to trap charged particles [102, 103]. Also, a quadrupolar electric field rotating at a high frequency (Paul trap) [104] can provide a dynamic trapping potential for the charged particles. In the classical picture, the motion of an ion in a Paul trap has two components, a fast oscillatory motion of small amplitude at the frequency of the quadrupolar electric field (micromotion) superimposed on a slower, smooth average motion (secular motion) [105]. The original Paul trap had electrodes in the shape of hyperboloids of revolution, and the field-free region in such a trap is a single point in the centre of the trap. In a hyperbolic quadrupole Paul trap, confining more than one ion leads to the ions being pushed away from the centre of the trap due to the Coulomb repulsion between them. This has the effect of an increase in micromotion for ions which are located away from the centre of the trap [106, 107]. For experiments in which a large crystal of laser-cooled ions [108] are necessary, excess micromotion is not desirable as it leads to inefficient cooling [109]. This problem can be circumvented in a linear Paul trap [106, 110], in which the electrodes are four cylindrical rods (see Fig 3.1). In a linear Paul trap, a quadrupolar electric field provides confinement in the radial directions and the axial confinement is generated by a static electric field. The field-free region in a linear Paul trap is a line instead of a single point as in the trap with hyperbolic electrodes, and allows for trapping and cooling large number of ions [111], which is essential for the experiment described in this thesis.

The ion trap in which the Doppler-free two-photon experiment is performed is a linear Paul trap consisting of four cylindrical rods as trap electrodes. In a linear Paul trap, a radio-frequency voltage drive is applied to a pair of diagonally opposite rods with the other diagonal pair of rods kept at rf ground to generate an electric trapping potential in the radial directions ($x$ and $y$ axes), which near the trap axis ($z$-axis, coincident with the symmetry axis of the trap) can be approximated as

$$V(x, y, t) = \frac{V_0}{2}\left(1 + \frac{x^2 - y^2}{R'^2}\right)\cos(\Omega t). \tag{3.1}$$

In Eq. 3.1, $V_0$ and $\Omega$ are the amplitude and angular frequency of the radio-frequency voltage at the location of the ions in the trap. $R'$ is the distance of the trap axis ($z$-axis) from the trap electrodes. Axial confinement in a linear Paul trap is provided by end-cap electrodes to which a dc voltage is applied. The linear Paul trap used in this experiment has electrodes made of molybdenum. A schematic of the ion trap electrode configuration is shown in Fig. 3.1.

An rf voltage of angular frequency $\Omega \approx 2\pi\times 13.2$ MHz was fed to the diagonally opposite rods (RF1 and RF2 in Fig. 3.1). The rf voltage was generated by an arbitrary waveform generator (AWG) (Agilent, 33250A) and amplified in a rf-amplifier (RF Communications Inc., 815 Amplifier), after which the voltage was transformed upward using a helical resonator, and subsequently fed into the vacuum chamber, where it is guided to the trap electrodes. The amplitude of the rf voltage at the trap electrodes is typically 270 V, provided by the two unsegmented rf electrodes, which each have independently controlled static potentials as well. The other pair of diagonal electrodes are divided into five segments, of which three are used to (together with the static voltages of the rf electrodes) provide controlled dc voltages to compensate for stray voltages and axial confinement to the trapped ions, while being ac-coupled to ground all the time to provide rf ground. Ultra-high vacuum is required in the chamber in

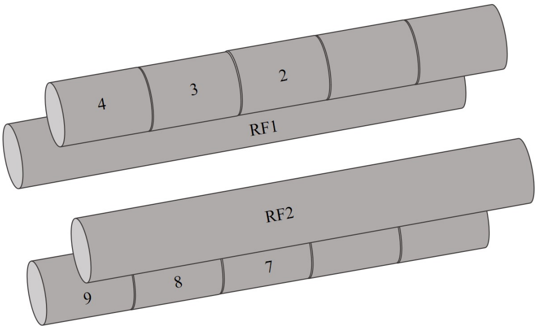

**Figure 3.1:** Schematic of the electrode configuration of the segmented linear Paul trap used in this experiment. The numbered electrodes indicate the section of the trap currently in use. Segments 2, 7, 4 and 9 form the end-cap electrodes of the ion trap, RF1 and RF2 are the electrodes to which the rf voltage drive is applied as well as static voltages for adjusting the confinement and position of the ions.

which the ion-trap is located to maximise the lifetimes of the ions. For this purpose, a combination of two turbo-molecular pumps mounted in series to increase the compression ratio (with pumping speeds of 520 l/s and 60 l/s) backed by a diaphragm pump is used. Once in a few months, a Titanium sublimation pump is used in conjunction with the above-mentioned pump combination to maintain a base pressure of $\sim 1.3 \times 10^{-10}$ mbar [1] in the ion-trap chamber. An extensive description of this ion trap is detailed in Refs. [86,96,98,112].

### 3.1.2 Laser-cooling setup for Be$^+$ ions

Since HD$^+$ ions cannot be directly laser-cooled, they have to be cooled sympathetically by a laser-cooled atomic species [113]. Sympathetic cooling works best when the charge-to-mass ratio between the coolant atoms and the HD$^+$ ions is $\approx 1$ [114]. For this reason, in this experiment, Be$^+$ ions are used as the coolant species [100]. Be$^+$ ions are cooled in the ion trap with laser light at 313 nm driving the $^2S_{1/2}$ to $^2P_{3/2}$ transition. In the following paragraph, the laser system used to generate the 313 nm laser light is described briefly.

Light at 626 nm is produced in a continuous-wave (CW) ring dye-laser (Spectra Physics, 380D) pumped by a frequency doubled CW Nd:YVO$_4$ laser at 532 nm. A pump laser power of 8 Watt at 532 nm is used to generate ~600 mW of

---

[1] The vacuum nipple in which the pressure gauge is mounted is quite hot, and lacks a line-of-sight to the turbo pump. Therefore the pressure inside the chamber will be lower. Cooling the vacuum nipple of the pressure gauge showed that the pressure in the main chamber is most probably just below $1 \times 10^{-10}$ mbar.

light at 626 nm. The dye used is Sulphorhodamine-B, also known as Kiton red, obtained from Radiant Dyes. The dye powder is dissolved in benzyl alcohol and mixed with ethylene glycol. This dye solution is then pumped through a nozzle by a dye circulator (Radiant Dyes, RD 1000) to form a dye jet which is pumped by the 532 nm laser, thus providing the gain medium for the ring dye-laser. The pressure used is ≈7.6 bar to produce a fast flowing, smooth dye jet devoid of air bubbles.

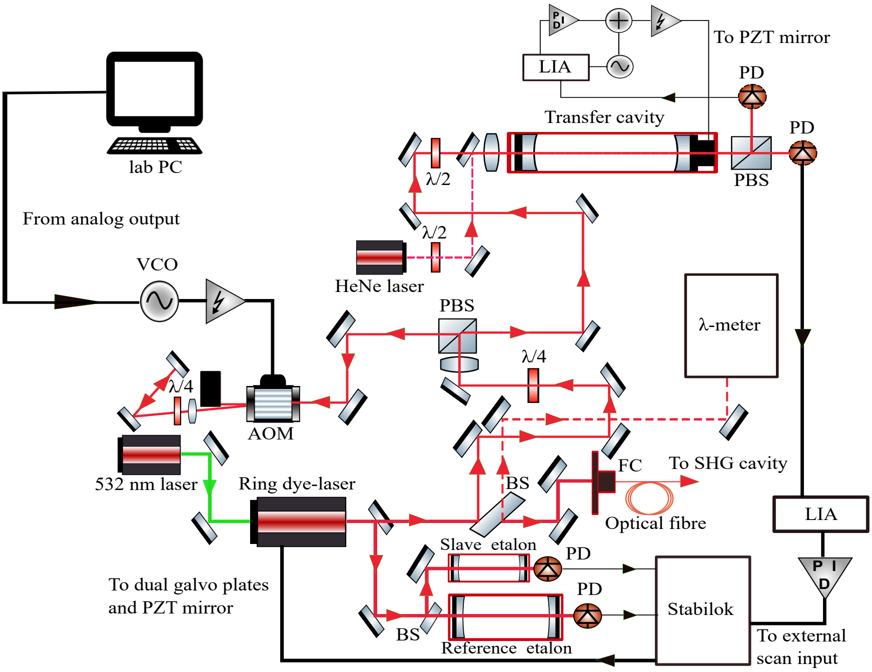

**Figure 3.2:** Schematic of the dye-laser setup used to generate tunable 626 nm light, converted to 313 nm in the SHG setup (Fig. 3.3) for laser cooling of Be$^+$ ions, with its frequency stabilisation scheme. PD, photodiode; BS, beam splitter; PBS, polarising beam splitter; LIA, lock-in-amplifier; λ-meter, wavelength meter; λ/2, half-waveplate; λ/4, quarter-waveplate; AOM, acousto-optic modulator; VCO, voltage-controlled oscillator; FC, fibre coupler/collimator.

The dye-laser is frequency stabilised using the arrangement shown in Fig. 3.2 and described in detail by Biesheuvel *et al.* [97]. To begin with, the dye laser is first stabilised to a reference and a slave etalon via the Stabilok locking mechanism [115]. Absolute frequency is measured using a wavelength meter

(Burleigh Instruments Inc, WA-20VIS) with a measurement uncertainty of 0.01 $\mathrm{cm}^{-1}$ (≈300 MHz). For tuning the dye-laser frequency continuously as required in the experiment, it is further offset locked to the fringes of another etalon (transfer cavity) [97]. The transfer cavity in turn is locked to a frequency-stabilised Helium-Neon (HeNe) laser oscillating at 633 nm with a specified absolute frequency accuracy of 2 MHz. The transfer cavity also provides absolute frequency stability to the dye laser. The frequency offset is provided by a double pass configuration through an in-loop acousto-optic modulator (AOM). When the frequency lock is engaged, the frequency of the dye laser can be expressed as

$$\nu_{\mathrm{dye}} = \nu_{\mathrm{HeNe}} + m \times \Delta_{\mathrm{FSR}} \pm \Delta_{\mathrm{AOM}}. \tag{3.2}$$

In Eq. 3.2, $\nu_{\mathrm{dye}}$ is the frequency of the ring dye-laser, $\nu_{\mathrm{HeNe}}$ is the frequency of the HeNe laser, $\Delta_{\mathrm{FSR}} \approx 149$ MHz is the free spectral range (FSR) of the transfer cavity and $\Delta_{\mathrm{AOM}}$ is the radio-frequency offset provided by the AOM. The frequency of the AOM can be tuned continuously by a voltage-controlled oscillator (VCO). $m$ is an integer denoting the number of times the FSR of the transfer cavity has to be multiplied to obtain $\nu_{\mathrm{dye}}$ from $\nu_{\mathrm{HeNe}}$. Continuous frequency tuning of the dye-laser is achieved by continuously tuning the AOM frequency while the servo-loop is engaged to keep the dye laser locked to the fringes of the transfer cavity. When the end of the AOM tuning range (±100 MHz) is reached, the AOM frequency can be stepped rapidly (faster than the response time of the feedback loop) by one FSR such that $m$ is increased or decreased by 1 while $\nu_{\mathrm{dye}}$ remains fixed. After this operation, the AOM (and thereby the dye laser frequency) can be tuned over another FSR of the transfer cavity. In this manner, the dye-laser can be continuously tuned over a range of 30 GHz at a maximum scan speed of 500 MHz $\mathrm{s}^{-1}$. A detailed discussion about the above-mentioned offset-lock can be found in Ref. [97].

About 300 mW of laser light at 626 nm is coupled into a single-mode optical fibre and impinged on a non-linear Brewster-cut $\beta$-Barium borate (BBO) crystal to coherently generate the second harmonic light at 313 nm (see Fig. 3.3). To increase the efficiency of the second harmonic generation (SHG) process and thus the amount of light at 313 nm available for the cooling of $\mathrm{Be}^{+}$ ions, the BBO crystal is placed in an enhancement cavity (SHG cavity) in bow-tie configuration [116]. The length of the SHG cavity is stabilised to the wavelength of the incident radiation at 626 nm to maximise intra-cavity power build up at 626 nm and consequenctly the output at 313 nm. The length stabilisation is provided by applying a feedback signal, produced using the Hänsch-Couillaud locking scheme to a piezo-electric transducer (PZT) mounted mirror in the SHG cavity, thereby controlling the length of the latter [117]. The feedback is generated by a proportional-integral-derivative (PID) controller (Toptica AG, PID110). About 6 mW of 313 nm light is generated after the SHG cavity, which after suffering losses at various optical surfaces provides ∼3 mW light at the location of the Be$^+$ ions in the ion trap.

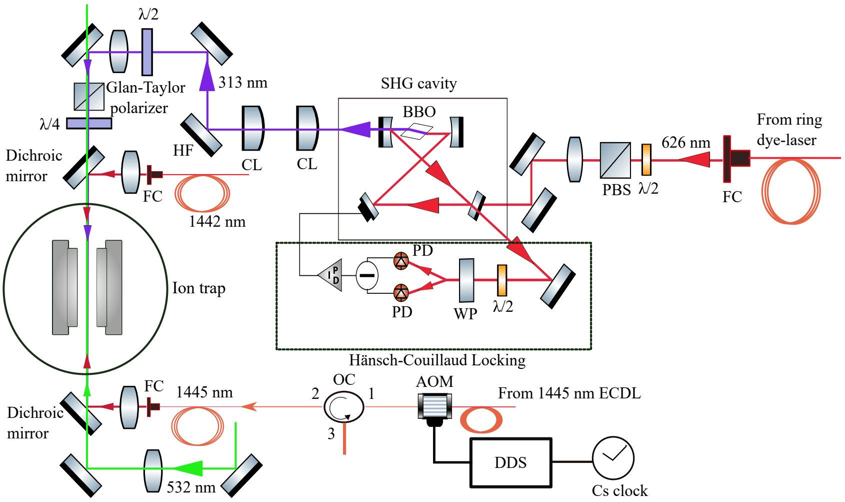

**Figure 3.3:** Schematic of the enhancement cavity used to generate light at 313 nm for cooling of Be$^+$ ions, with its frequency stabilisation scheme. CL, cylindrical lens; HF, harmonic filter; WP, Wollaston prism; OC, optical circulator; DDS, Direct digital synthesiser.

The Be$^+$ ions are Doppler laser-cooled by a single beam of 313 nm light with circular polarisation directed along the trap axis ($z$-axis) [112]. The beam is focussed to a beam waist of ∼150 $\mu$m at the location of the ions in the ion trap. For efficient laser cooling with a single beam, it is imperative to have a well defined quantisation axis which, in combination with the circular polarisation and the concomitant optical pumping, leads to an effective two-level system in the atomic species. In this case, the quantisation axis is provided by a static magnetic field (bias magnetic field) directed along the propagation direction of the 313 nm light. The bias magnetic field is generated by a pair of current-carrying coils (main coils) in Helmholtz configuration. As mentioned in Chapter 2, efficient cooling can be achieved for a minimum magnetic field of ∼20 mG. Any projection of the bias magnetic field along perpendicular directions ($x$ and $y$-axes) due to geometrical imperfection is cancelled by delivering an appropriate amount of current to a pair of current-carrying coils (shim coils) along the $x$ and $y$-axes each, while looking for maximum fluorescence of the laser-cooled Be$^+$ ions on an electron-multiplying charge-coupled-device (EM-

CCD) camera (Andor Technology, iXon$^{\mathrm{EM}}$+). The currents through the shim coils are also carefully tuned to cancel out any other form of stray magnetic field such as the Earth's magnetic field and the magnetic field due to the turbo pump employed to maintain ultra-high vacuum in the ion trap chamber. In this manner, the quantisation axis is kept fixed along the trap axis.

As will be explained later in Chapter 4 (Sec. 4.2.1), it is required to keep the magnetic field as small as possible to minimise the Zeeman shift during probing (REMPD duration) the Doppler-free two-photon transition. However, as the detection scheme via secular excitation requires efficient laser cooling, a higher bias magnetic field is desirable. This warrants some type of magnetic field switching between probing and detection through secular excitation. To faithfully reproduce the same magnetic field vectors during each phase of a measurement cycle, it is essential to have precise control over the current flowing through the main and shim coils. To this end, a voltage-controlled current supply (VCCS) capable of both sourcing and sinking current was designed and implemented in the ion trap setup in collaboration with the electronics workshop at Vrije Universiteit Amsterdam (Elektronica Beta VU). A control voltage is applied to the positive input of an operational amplifier (op amp), which drives its output voltage in a manner so that it switches on a bipolar junction transistor (BJT) T1 (see Fig. 3.4 for a schematic of the VCCS) when the control voltage is positive and the circuit acts as a current source. When the control voltage is negative, it drives the output voltage of the op amp in a manner such that another BJT (T2) is switched on, turning the circuit into a current sink. The current thus produced flows through the bias (and the shim coils) of the ion trap and through a sense resistor, which converts the current to a voltage to be used to apply a feedback to keep the current constant as long as the control voltage is fixed. In this manner, by changing the control voltage, the magnetic field can be switched in a reliable and reproducible manner. The voltage to current conversion of the circuit is set to 1, such that a change in the control voltage by 2.4 mV (which is the minimum voltage step size of the anolog output card used) produces a change in the current by 2.4 mA.

### 3.1.3 Experimental control and automation

The experimental setup has been automated to increase reproducibility and reliability during the measurement process. The control software has been implemented in the Python 2.6 programming language on a computer (Fujitsu, CELSIUS M730power) running Windows 7 operating system, which henceforth will be referred to as the lab PC.

The AWG used to generate the frequency and amplitude of the radio-frequency applied for the radial trapping of the ions in the ion trap is controlled via the lab PC. The dc voltages applied to the ion trap electrodes for compensation

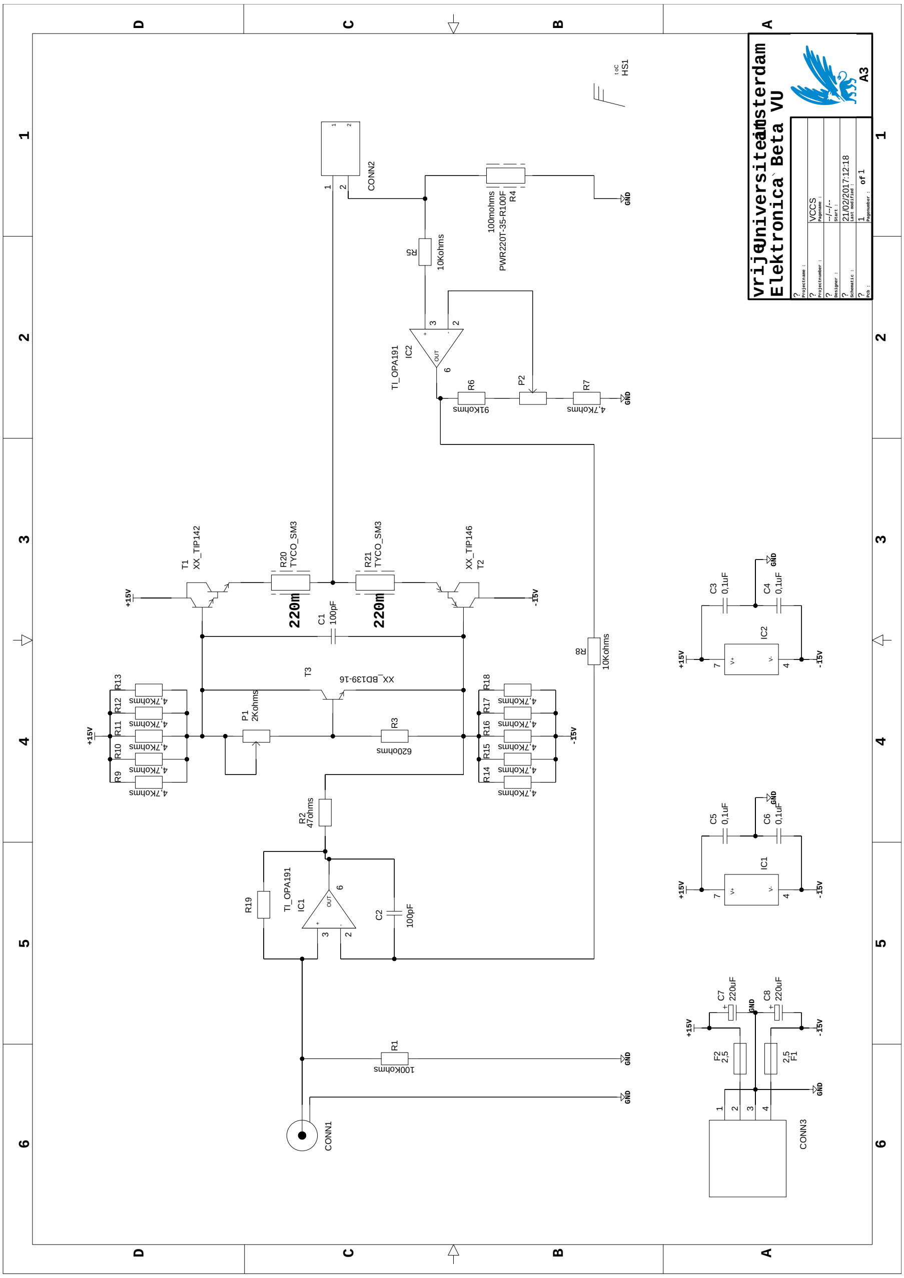

**Figure 3.4:** Electrical schematic of the VCCS used to switch between high and low magnetic field in the ion trap.

of stray electric fields are generated by a 13-bit analog output card (National Instruments, PCI 6723). This also allows switching between the individual and "multi-pole expansion" voltage control of the trap electrodes without the necessity of design and construction of dedicated electronic hardware. The compensation voltages applied to the ion trap electrodes are kept actively stabilised to their set values by a feedback circuit [98]. The rf voltage drive required for secular excitation of the $HD^+$ ions is applied by a voltage-controlled buffer amplifier (control voltage applied via the analog output card). The current required by the Be oven and the e-gun to produce $Be^+$ ions in the trap are set by the computer. Similarly, the stepper motor controlled leak valve to introduce HD gas in the trap vacuum chamber for producing $HD^+$ ions in the ion trap is also controlled by the lab PC. To avoid unwanted drifts of the e-gun emission current during trap loading, the emission current is actively controlled to a pre-set value. This is achieved by measuring the current drawn from the high-voltage source (which provides the e-gun's negative bias voltage as well as the emission current itself) by a sense resistor, which is then sent into a PID controller. The PID controller feeds back onto the e-gun filament current through an opto-coupler (so as to achieve galvanic isolation between the PID controller electronics and the high-voltage e-gun circuitry), which determines the filament temperature and thereby the emission of thermal electrons and, thus, the emission current.

The exposure of the $HD^+$ ions to the various laser beams during REMPD is controlled by mechanical shutters via application of synchronised TTL pulses from the lab PC. During REMPD, the $Be^+$ ions are cooled to $\sim$10 mK at a low bias magnetic field of $\sim$100 mG to reduce the Zeeman shift on the transition to be measured in the sympathetically cooled $HD^+$ ions. For this purpose, the detuning of the 313 nm laser is reduced to $-50$ MHz from the resonance frequency of the cooling transition and its power reduced to $\sim$150 $\mu$W during REMPD. During the secular excitation detection period, the detuning of the 313 nm laser is increased to $-300$ MHz from the resonance frequency of the cooling transition and the cooling-laser power increased to the maximum value ($\sim$2.5 mW). To reliably reproduce this power switching of the cooling laser, a half waveplate mounted on a motorised rotation stage is used in combination with a Glan-Taylor polariser in the 313 nm beam path between the SHG cavity and the ion trap. For controlling the detuning of the 313 nm laser, a VCO-controlled AOM is used as described in Sec. 3.1.2. The voltage controlling the VCO is applied by the lab PC via an analog output card (National Instruments, PCI 6723). The motorised rotation stage (Thorlabs, PRM1/MZ8) is also controlled by the lab PC.

The bias magnetic field required for laser cooling of $Be^+$ ions has to be switched to a low value during REMPD and to a high value during secular excitation and is implemented by a voltage-controlled current supply as mentioned in

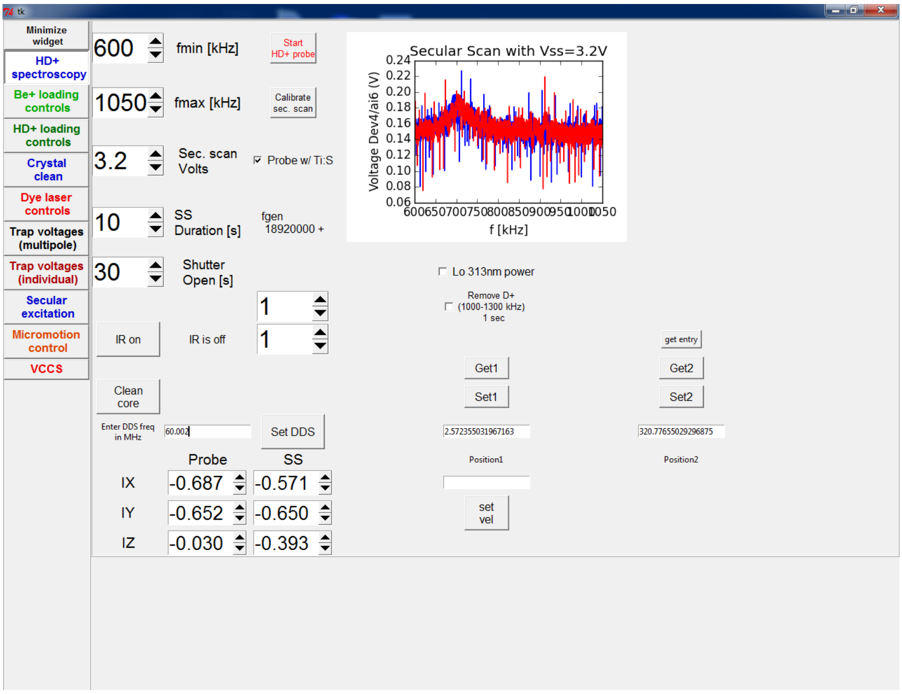

fmin [kHz]: 600

fmax [kHz]: 1050

Sec. scan Volts: 3.2

SS Duration [s]: 10

Shutter Open [s]: 30

☑ Probe w/ Ti:S

fgen 18920000 +

☐ Lo 313nm power

☐ Remove D+ (1000-1300 kHz) 1 sec

1

1

Enter DDS freq in MHz: 60.002

Position1: 2.572355031967163

Position2: 320.77655029296875

|  | Probe | SS |
|---|---|---|
| IX | -0.687 | -0.571 |
| IY | -0.652 | -0.650 |
| IZ | -0.030 | -0.393 |

**Figure 3.5:** Screenshot of the Tkinter GUI showing the window used to run the Doppler-free two-photon spectroscopy experiment. The different tabs on the left-hand side of the screen represent separate interfaces for functionalities such as Be$^+$ and HD$^+$ ion loading, controlling the detuning of the laser used for Doppler cooling of Be$^+$ ions, setting individual and multi-pole expansion control voltages of the trap electrodes, and setting the current of the VCCS.

Sec. 3.1.2. The secular excitation spectrum is recorded by a photomultiplier tube (Hamamatsu, R928) in conjunction with a photon counting system (Ortec Brookdeal, 5CI) and concurrently with the EMCCD camera. The experimental control software is used to read out the secular excitation fluorescence spectrum from the EMCCD camera via another control software also implemented in Python 2.6.
The entire experimental control software written in Python 2.6 is operated via the Tkinter graphical user interface (GUI) and a touch-screen monitor. A screenshot of the GUI used for the Doppler-free two-photon spectroscopy experiment is shown in Fig. 3.5.

### 3.1.4 Performance of the ion trap and laser-cooling setup

$Be^+$ ions are loaded into the ion trap by electron-impact ionisation of gas-phase neutral beryllium atoms, which are produced by a resistively heated oven containing a small beryllium wire. Through Doppler laser cooling at 313 nm, the $Be^+$ temperature in our apparatus can be reduced to 5…6 mK. Apart from a suitable choice of the 313 nm laser intensity, polarisation and detuning, this requires minimisation of micromotion by compensation of stray electric fields, and precise alignment of the magnetic bias field (which defines the quantisation axis) with the propagation direction of the laser [86, 118].

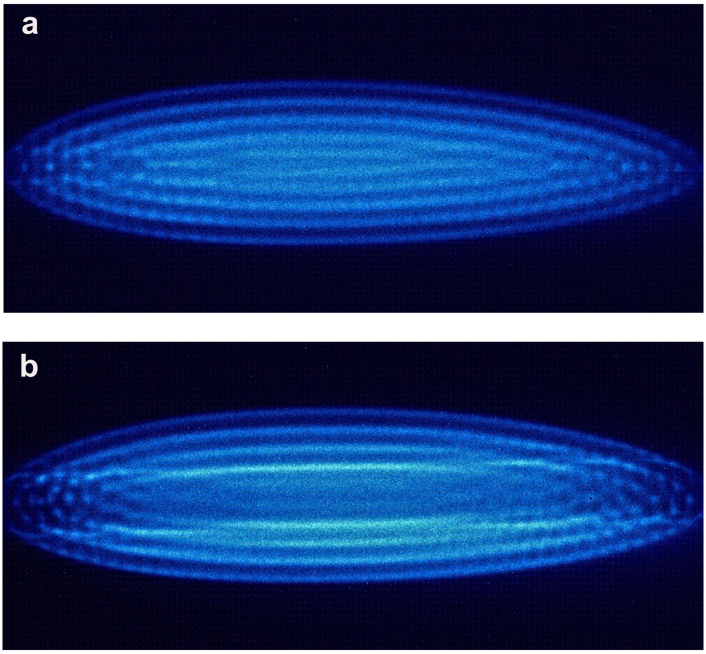

**Figure 3.6:** EMCCD images of typical Coulomb crystals consisting of $Be^+$ ions (a) and a bi-component ion crystal of $HD^+$ ions sympathetically cooled by laser-cooled $Be^+$ ions (b) are shown. The $HD^+$ ions form the dark core in the centre in (b).

Ion crystals comprised of 1000…1500 laser-cooled $Be^+$ ions are routinely generated in the ion trap. Fluorescence photons emitted by the $Be^+$ ions are collected using a combination of two lenses, filtered by a 313 nm optical band-pass filter, and imaged on the EMCCD camera placed perpendicularly to the direction of propagation of the 313 nm light. The three-dimensional ion crystals are ellipsoidal in shape with the major axis along the trap axis. $HD^+$ molecular ions are also produced *in situ* by electron impact ionization of neutral HD gas leaked in the ion-trap chamber through a stepper motor controlled leak valve. The thus created $HD^+$ ions are sympathetically cooled by the laser-cooled crystal of $Be^+$ ions to ∼10 mK translational secular temperature [86, 119]. Due to the nature of the ponderomotive trapping potential of the linear Paul trap, the lighter $HD^+$ ions experience tighter confinement because of their larger charge-to-mass ratio, and therefore occupy the central part of the crystal forming a dark core surrounded by the fluorescent $Be^+$ ions (Fig. 3.6b). About 40-100 $HD^+$ ions are sympathetically cooled together with some $H_2D^+$, ${HD_2}^+$, $H_3^+$ impurity ions.

## 3.2 Frequency stabilisation of the spectroscopy lasers

The lasers used for probing the two-photon transition are commercial, off-the-shelf extended cavity diode lasers (ECDLs) obtained from Toptica AG (DL 100 Pro). The grating-stabilised lasers were tuned to oscillate in single mode at 1442.4 nm and 1445.3 nm. The linewidth of these lasers is ∼100 kHz. A laser linewidth of 100 kHz would require high laser powers to induce a transition rate $\Gamma_{2\mathrm{ph}}$ sufficient for an observable spectroscopic signal of the Doppler-free two-photon transition. Such high laser powers and broad laser linewidths are not desirable as that would lead to a broad experimental feature, large power broadening and AC Stark shift, and consequently would impede achieving the target experimental accuracy of $\sim 10^{-12}$ in relative frequency uncertainty terms. Hence, the light generated by the lasers has to be spectrally narrowed. Also, the spectroscopy laser setup and the ion trap setup are in different lab spaces about 40 metres apart. Hence, the probe radiation of both the lasers have to be transferred via optical fibres. As the optical path length between the input and output terminals of the fibre varies randomly due to acoustic and thermal fluctuations, the optical fibre introduces noise on the optical wave it carries through the Doppler effect. In a round trip through the 40 m long optical fibre, the laser linewidth was measured to increase by ∼200 Hz, i.e., by ∼70 Hz in a single-pass (Sec. 3.2.2). So, to have the probe light in the ion trap with a linewidth ∼1 kHz, the linewidth of the lasers needed to be narrowed to <1 kHz before coupling into the optical fibre (or a complicated fibre-optic noise cancellation scheme has to be implemented).

A standard method of frequency stabilising a laser is to stabilise it to the transmission fringes of a high-finesse cavity (finesse ∼ 100000) made of ultra-low expansion (ULE) glass [120]. At a particular temperature, ULE glass has zero linear thermal expansion coefficient (zero-CTE temperature). The cavities are operated at this temperature by keeping them in an actively temperature-controlled chamber, thereby reducing the effects of random thermally induced cavity length variations adversely affecting the laser frequency stabilisation. The seismic noise introduced due to mechanical vibrations is cancelled by mounting the cavity setup on an actively vibration isolated platform. These cavities are furthermore kept under vacuum and inside an acoustically isolated enclosure to prevent perturbations due to acoustic noise. Lasers are stabilised to these cavities using the Pound-Drever-Hall (PDH) locking scheme [121]. With all these precautions, lasers are routinely narrowed down to few hundred mHz linewidth. The thermal noise floor of these high-finesse cavities can be even pushed down further by using single-crystal silicon cavities at cryogenic temperatures [122]. The down-side to these setups is that they have limited tunability.

A different protocol using an octave-spanning optical frequency comb (OFC) laser [123, 124] can be used to stabilise multiple lasers to the same ultrastable laser simultaneously as long as the wavelength of the lasers concerned are within the spectral bandwidth of the OFC. An OFC laser is a mode-locked femto-second pulsed laser whose repetition rate and carrier-envelope-offset frequencies are stabilised to a reference oscillator. The physics of optical frequency comb lasers is a subject in its own right and is beyond the scope of this thesis to be described in detail. Here, we briefly mention the main features of these lasers and introduce the OFC laser used in the experiment described in this thesis.

### 3.2.1 The optical frequency comb (OFC) and the ultra-stable laser

The frequency of each mode of the OFC can be expressed as

$$f_n = \pm f_0 + N \times f_{\text{rep}}, \tag{3.3}$$

where $f_{\text{rep}}$ and $f_0$ are the repetition rate frequency and the carrier-envelope offset frequency of the comb, respectively. $N$ is an integer denoting the mode number of the OFC laser.

An OFC laser whose $f_{\text{rep}}$ and $f_0$ are stabilised to an atomic clock can also be used as an absolute frequency reference. Such a commercial optical frequency comb laser (FC1500-250-WG) obtained from Menlo Systems GmbH is already available in the Atoms, Molecules and Laser Physics group at Vrije Universiteit Amsterdam. The $f_{\text{rep}}$ and $f_0$ of this OFC laser is stabilised to a commercial caesium atomic clock (Microsemi, CsIII model 4310B) with a frequency instability of $\sigma_y(\tau) < 8.5 \times 10^{-13}$ at 1000 seconds averaging time [125]. As can be seen from Eq. 3.3, the frequency instability of the comb modes depends on the instabilities of the $f_{\mathrm{rep}}$ and the $f_0$, which are partly due to the Cs atomic clock (in particular on longer time scales), and partly limited by noise sources inside the OFC laser itself (which impacts primarily the short-term stability). The caesium clock is continuously being compared with a rubidium atomic clock, which itself is disciplined to a GPS receiver for traceability to the SI second. On long time scales, the two atomic clocks are in agreement at the $1 \times 10^{-12}$ level or better, indicating that the frequency comb supports optical frequency measurements at the same accuracy level.

The oscillator of the OFC laser used in this experiment is a mode-locked Erbium-doped fibre laser with a centre frequency of 1560 nm. The output of the mode-locked laser is amplified and broadened in a highly non-linear fibre (HNLF) to generate an octave-spanning spectrum. The comb is self-referenced [126] with $f_0 = \pm 20$ MHz. The full-width at half-maximum (FWHM) of the $f_0$ beat is ~90 kHz. The $f_{\mathrm{rep}}$ of the comb is nominally 250 MHz with a narrow range of tunability (about ±2 MHz). While $f_{\mathrm{rep}}$ itself is derived from a highly stable frequency synthesiser, the optical beat note between the OFC and the CW spectroscopy lasers involves an OFC mode with $N \sim 10^6$. This large multiplication factor leads to a ~100 kHz linewidth of the individual comb modes. Hence, phase stabilising the spectroscopy lasers directly to the OFC would not be sufficient for the Doppler-free experiment.

A clever workaround this problem is to stabilise the repetition rate of the frequency comb to an ultra-stable laser with sub-Hz linewidth. Such a commercial ultra-stable laser (from now on to be called Hz laser) (Menlo Systems GmbH, ORS1500) is also available in our laboratory as a part of the frequency metrology infrastructure. The oscillator of this laser is an Erbium-doped fibre laser operating in continuous wave mode at ~1542 nm with a specified linewidth $< 2$ Hz. The $f_{\mathrm{rep}}$ of the OFC can be phase-locked to the Hz laser by applying a fast feedback to an intra-cavity electro-optic modulator (EOM) within the frequency comb resonator. Very high stabilities over the full spectrum of the OFC can be obtained by careful characterisation of the transfer functions between the actuators of the comb and the parameters $f_{\mathrm{rep}}$ and $f_0$ [127]. However, implementing this method in the OFC in our lab would have been a time-consuming endeavour, and we did not pursue this path. Instead we implemented a phase lock between the Hz laser and the ECDLs using the so-called "virtual beat notes", as described in the following section.

### 3.2.2 The transfer-oscillator locking scheme

#### Principle and implementation

It is desirable to directly stabilise the phase of our spectroscopy lasers to the Hz laser as the latter has a spectral purity which would be perfect for our purpose. However, the wavelength of the Hz laser is ∼100 nm away from the wavelengths of the spectroscopy lasers. Since a detector with such a large bandwidth is not available, the phases of the concerned lasers cannot be directly compared. However, since the Hz laser and both of the spectroscopy lasers are well within the spectrum of the OFC, a "transfer oscillator" locking scheme following Ref. [128] can be implemented to transfer the phase stability of the Hz laser to our spectroscopy lasers.

In its essence, the transfer oscillator locking scheme implemented in this work entails phase-stabilising both the ECDLs to the Hz laser simultaneously using the OFC as a "flywheel". The stabilisation scheme used is described below for the ECDL oscillating at 1442 nm and was implemented in the same manner for the ECDL at 1445 nm. In this scheme, a beat note $\Delta_{1442}$ is made between the ECDL at 1442 nm and its nearest comb-mode. Similarly, another beat note $\Delta_{\text{Hz laser}}$ is made between the Hz laser and its nearest comb-mode. The beat notes can be expressed as

$$\nu_{1442} = \pm f_0 + N_{1442} \times f_{\text{rep}} \pm \Delta_{1442} \tag{3.4a}$$

$$\nu_{\text{Hz laser}} = \pm f_0 + N_{\text{Hz laser}} \times f_{\text{rep}} \pm \Delta_{\text{Hz laser}}. \tag{3.4b}$$

The ambiguity in sign of the $f_0$ can be determined by looking at the frequency of the beat notes while changing the $f_0$ by a small amount. The ambiguity in the sign of the beat notes $\Delta_{1442}$ or $\Delta_{\text{Hz laser}}$ can also be resolved by changing $f_{\text{rep}}$ and observing the effect on the beat notes. For an extended measurement period, it is desirable to have a setup that requires minimum day-to-day maintenance. With this in mind, the frequency stabilisation setup for the spectroscopy lasers were built to be as close to a "turn key" system as possible. A basic requirement to this end is to have an optical-fibre-based beat note detection unit (FC-BDU). Such optical-fibre-based BDUs are available in the telecommunication band of the electromagnetic spectrum (C-band, 1540...1580 nm) due to the availability of fibre-pigtailed photodetectors, and off-the-shelf fibre-coupled optical band-pass filters (developed for DWDM, dense wavelength division multiplexing) which limit the optical spectrum impinging on the photodetector and thus prevent optical overload. Such a BDU is used to generate the beat note between the Hz laser and the OFC. For the spectroscopy lasers at 1442 nm and 1445 nm, the BDUs were set up using a combination of fibre-optic and free-space elements. A schematic of the BDUs is shown in Fig. 3.8 below. Light from the spectroscopy lasers is coupled into optical fibres via fibre-docks procured from Toptica AG, which have excellent reproducibility and require minimum re-alignment from day to day. The free-space output of the OFC is coupled into a single-mode optical fibre mounted on a three-axis translation stage (Thorlabs GmbH, MAX313D/M-3-Axis NanoMax Stage). Light from the OFC and the spectroscopy lasers is combined in a 80%-20% fibre-combiner

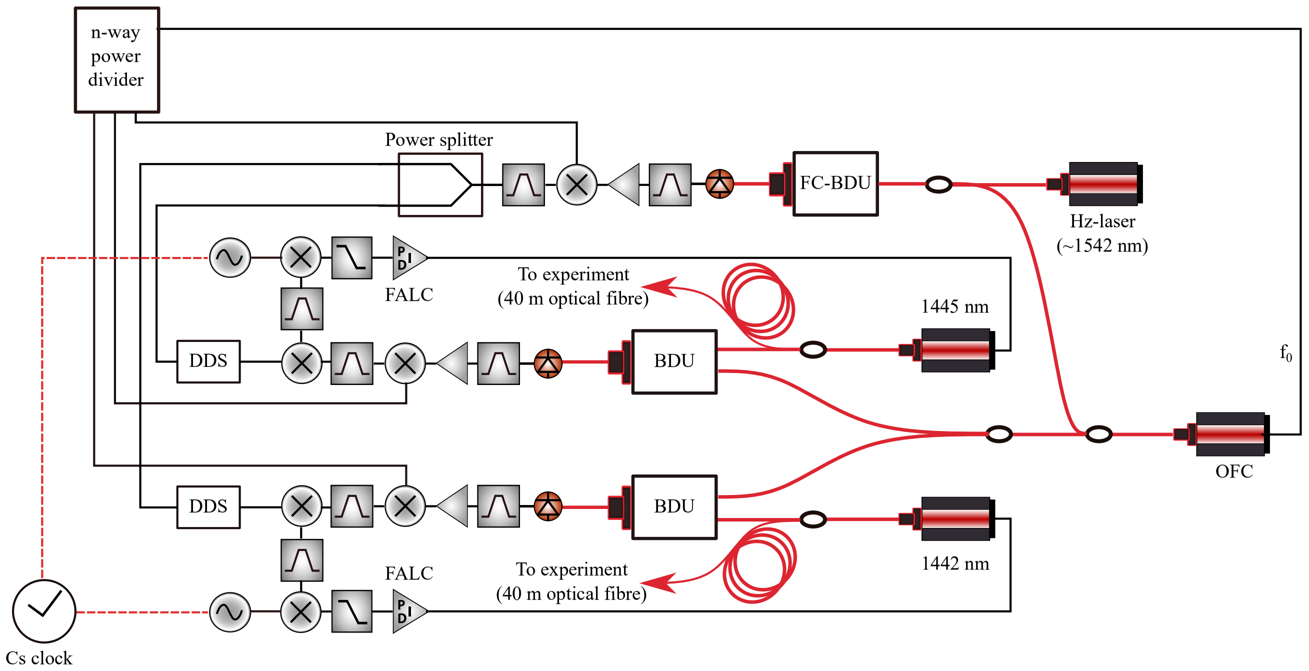

**Figure 3.7:** Schematic of the optical and electrical setup for the transfer oscillator frequency stabilisation of the spectroscopy lasers to the Hz laser. FC-BDU, fibre-coupled beat detection unit; BDU, beat detection unit; DDS, direct digital synthesis integrated circuit; FALC, Fast Analog Linewidth Control.

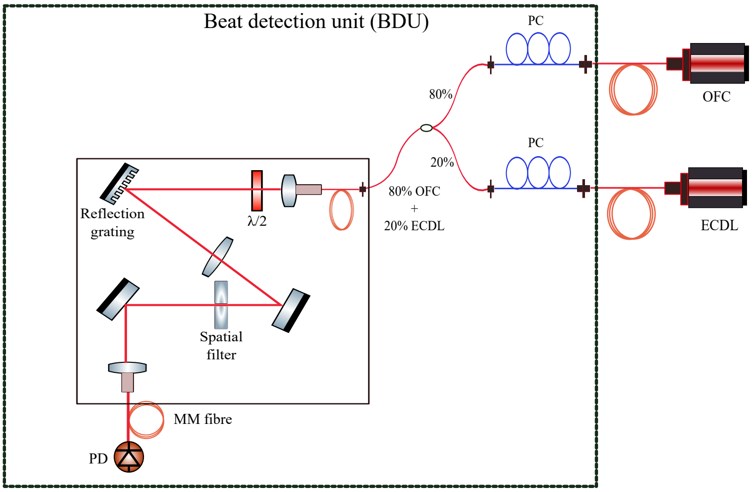

**Figure 3.8:** Schematic of the beat note detection unit for the beat note between the spectroscopy lasers and the optical frequency comb. PC; in-line fibre polarisation controller; MM fibre, multi-mode optical fibre; PD, photodetector; $\lambda/2$, half-waveplate.

(80% OFC light, 20% ECDL light) and collimated before being launched into the BDU. Combining and coupling the beams into a single optical fibre is instrumental in saving time on alignment on a daily basis. All the fibre arms carrying light to the BDU are equipped with in-line fibre polarisation controllers to match the polarisation of the interfering light waves for maximum signal-to-noise ratio (SNR) of the beat note. The combined light from the OFC and the ECDL is spectrally band-pass filtered by a combination of a reflective diffraction grating, a positive lens, and a slit (with the grating and slit located in the conjugate planes of the lens). The filtered light is coupled into a multi-mode optical fibre and made incident on a fibre-coupled photodetector with 3 GHz electrical bandwidth.

The SNR of the beat notes $\Delta_{1442}$ and $\Delta_{\text{Hz laser}}$ should be $\geq$ 30 dB to avoid cycle-slips, which lead to additional frequency noise and potentially frequency offsets. Tracking oscillators can be used to improve the SNR of the radio-frequency beat notes $\Delta_{1442}$ and/or $\Delta_{\text{Hz laser}}$ in case the adequate SNR cannot be obtained in the beat notes. A tracking oscillator is basically a VCO which follows the phase and frequency of the beat note $\Delta_{1442}$ or $\Delta_{\text{Hz laser}}$ via a phase-locked loop (PLL). However, this method has the drawback of limiting the control bandwidth of the optical PLL, which would necessitate some kind of optical pre-stabilisation of the ECDLs. Hence, tracking filters were not used in our setup. To ensure good SNR of the beat note between the nearest OFC mode and the ECDLs, the parameters of the OFC was slightly tweaked to increase the spectral power near 1442 nm without compromising on the SNR of the $f_0$ of the OFC. Owing to the availability of off-the-shelf rf-electronic components, $\Delta_{1442}$ and $\Delta_{\text{Hz laser}}$ were set to ~30 MHz and ~60 MHz respectively. The beat note $\Delta_{1442}$ is then amplified to ~7 dBm by an assembly of 3 low-noise amplifiers (Mini Circuits, ZFL-500LN-BNC+) and 3 band-pass filters (Mini Circuits, BBP-30+). $\Delta_{\text{Hz laser}}$ was also amplified by an assembly of 3 low-noise amplifiers and 3 band-pass filters at 60 MHz (MiniCircuits, BBP-60+) to ~10 dBm, and split into two parts by a 1 : 2 rf power-splitter as required by the stabilisation method which will be described later in the following paragraphs.

$\Delta_{1442}$ and $\Delta_{\text{Hz laser}}$ can then be mixed in a rf mixer and properly filtered to get rid of the $f_0$ and its associated noise, resulting in

$$f_\Delta = (\nu_{1442} - \nu_{\text{Hz laser}}) - (N_{1442} - N_{\text{Hz laser}}) \times f_{\text{rep}}, \tag{3.5}$$

where $f_\Delta$ is the virtual beat note between the ECDL at 1442 nm and the Hz laser. The second term in the expression for $f_\Delta$ contains the noise associated with $f_{\text{rep}}$ multiplied by the difference in mode numbers nearest to the frequencies of the ECDL at 1442 nm (also for the ECDL at 1445 nm) and the Hz laser. Due to the 100 nm wavelength difference between the two, this multiplied $f_{\text{rep}}$ noise contributes ~10 kHz linewidth.

To get around the residual $f_{\text{rep}}$ noise, the following procedure was adopted from Ref. [128]. The $f_0$ was first mixed individually with the beat notes $\Delta_{1442}$ ($\Delta_{1445}$) and $\Delta_{\text{Hz laser}}$ in rf-mixers (Mini Circuits, ZAD-1-1+) and properly filtered to get rid of the $f_0$ noise. Assuming the sign of $f_0$, $\Delta_{\text{Hz laser}}$ and $\Delta_{1442}$ to be "+" for the sake of clarity, these filtered frequencies can be expressed as

$$\Delta^*_{1442} = \nu_{1442} - N_{1442} \times f_{\text{rep}} \tag{3.6a}$$

$$\Delta^*_{\text{Hz laser}} = \nu_{\text{Hz laser}} - N_{\text{Hz laser}} \times f_{\text{rep}}. \tag{3.6b}$$

$\Delta^*_{\text{Hz laser}}$ can be multiplied with the ratio of two integers $\frac{N_1}{N_2}$ and then mixed with $\Delta^*_{1442}$ and appropriately filtered to get

$$f^*_\Delta = (\nu_{1442} - \nu_{\text{Hz laser}}) - (N_{1442} - N_{\text{Hz laser}} \times \frac{N_1}{N_2}) \times f_{\text{rep}} \tag{3.7}$$

If integers $N_1$ and $N_2$ in Eq. 3.7 are chosen such that

$$\frac{N_1}{N_2} = \frac{N_{1442}}{N_{\text{Hz laser}}},$$

then the second term in the expression for $f^*_\Delta$ becomes zero. $f^*_\Delta$ can then be used to compare the frequency and phase difference between the Hz laser and the ECDL at 1442 nm without any noise introduced by the OFC. $f^*_\Delta$ is known in technical parlance as "virtual beat note".

$N_{1442}$ and $N_{\text{Hz laser}}$ are known accurately by measuring the wavelengths of all the three lasers with a wavelength meter (Keysight, 86122C Multi-wavelength meter) with a measurement uncertainty of ~40 MHz, which is much less than half of the mode-spacing (~125 MHz) of the OFC and an accurate knowledge of $f_{\text{rep}}$, $f_0$, $\Delta_{1442}$, $\Delta_{\text{Hz laser}}$ together with the proper signs of these quantities. The wavelength meter was calibrated by comparing the wavelength of the Hz laser measured by it with independent determination of the same parameter using the OFC (for details on the method to determine the wavelength of the Hz laser with an OFC, see Refs. [129–131]). No offset was measured within the measurement uncertainty of the Keysight wavelength meter.

Keeping in mind the somewhat limited set of available operating frequencies of commercial rf-electronic components, $f_{\text{rep}}$ was chosen to have a value of ~250 MHz and the signs of $f_0$, $\Delta_{\text{Hz laser}}$ and $\Delta_{1442}$ were so chosen that $f^*_\Delta$ was ~30 MHz for both the ECDLs with $\Delta^*_{\text{Hz laser}}$ and $\Delta^*_{1442}$ to be ~40 MHz and ~10 MHz, respectively. Other possibilities were limited due to infrastructural constraints as will be described later in Sec. 3.2.2.

The multiplication of $\Delta^*_{\text{Hz laser}}$ by $N_1/N_2$ was done with a direct digital synthesis (DDS) integrated circuit (Analog Devices, AD9912). Simply put, a DDS multiplies an input radio-frequency with a pre-programmed ratio of two integers to produce a phase-coherent output frequency of choice within its range of operation. $f^*_\Delta$ was then compared to a Cs-clock-referenced stable rf source (Agilent, 33250A arbitrary waveform generator) with frequency ~30 MHz in an analog phase detector (MiniCircuits, ZRPD-1+) to generate an error signal, which was used to generate a wide-band control signal to the ECDL. The feedback was provided by a commercial (Toptica AG) proportional-integral-derivative (PID) regulator FALC (Fast Analog Linewidth Control) to both the current in the laser diode and the piezoelectric transducer (PZT) driving the grating of the ECDL. The feedback to the current was used to track the faster phase-noise. The feedback to the PZT suppressed the slow random frequency drifts. In this manner, in principle, it is possible to keep the ECDLs phase-locked to the Hz laser over an entire free-spectral range (FSR) of the extended cavity of the diode laser. However, in practice, the locking range is limited by the specifications of available electronic components such as band-pass filters, amplifiers, etc. The lock was further improved by passive vibration isolation achieved by putting the ECDLs on a solid 20 mm thick breadboard separated from the optical table via Viton rubber rings. Acoustic isolation was achieved by enclosing the ECDLs in a thick wooden cabinet, the inner walls of which were lined with pyramid foam. The absolute optical frequency of the ECDL was measured by counting the beat note frequency between the ECDL and the nearest mode of the OFC with a frequency counter (Agilent, 53131A) in combination with an accurate knowledge of $N_{1442}$ from the wavelength measurement, and the optical comb equation, Eq. 3.4a. The beat note $\Delta_{\text{Hz laser}}$ was counted by a zero dead-time frequency counter (K+K Messtechnik, FXM50). All the relevant beat note frequencies were continuously logged during the entire measurement campaign each day.

The Hz laser is known to drift slowly at an approximately linear rate of 0.03 Hz per second on average. Due to this non-zero drift of the Hz laser, the 1442 nm ECDL phase-locked to the former will also drift by

$$\Delta\nu_{1442,\text{drift}} = \frac{N_{1442}}{N_{\text{Hz laser}}} \times \Delta\nu_{\text{Hz laser,drift}}, \tag{3.8}$$

and similar for the 1445 nm ECDL. For a typical duration of a measurement sessions of four hours, the drift amounts to ∼400 Hz ($\sim 1 \times 10^{-12}$), which is of the order of the target resolution of the Doppler-free two-photon experiment. Note that any potential larger drift can be reliably detected since the caesium atomic clock, used to reference the OFC, has a specified instability below $8.5 \times 10^{-13}$ at 1000 s of averaging. For a REMPD duration of 30 seconds (choice of REMPD duration justified in Sec. 4.3.2), the drift of the Hz laser amounts to ∼0.9 Hz, and for the spectroscopy lasers, the drift is proportionally higher according to Eq. 3.8.

The frequency of the ECDL is corrected to account for the drift of the Hz laser quasi-continuously. The correction scheme is as follows. The beat note $\Delta_{\text{Hz laser}}$ between the Hz laser and the nearest OFC mode is recorded for 1000 seconds with a gate time of 1 second with the frequency counter. The choice of this 1000 s duration is based on the $\sigma$-$\tau$ plot of the frequency instability of the Hz laser with respect to the OFC (typical minimum instability of $8.5 \times 10^{-13}$ at 1000 s averaging time). Then an appropriate frequency correction following Eq. 3.8 is applied to correct the frequency of the virtual beat note between the ECDL and the Hz laser for the drift of the latter. The calculation of the frequency correction and steering of the frequency of the virtual beat note was done in LabView.

All the rf frequencies and frequency counters are referenced to the Cs atomic clock for traceability to the SI unit of second (and thereby to the frequency unit Hz). The counters for recording the rf beat note frequencies between the ECDLs and the OFC are read out over a fibre-optic White Rabbit time and frequency distribution network [132]. The advantage of such a network is that it can be used to transmit data (through optical Gigabit Ethernet) and the Cs clock frequency both with sufficient accuracy and precision. For example, the frequency stability of White Rabbit is typically comparable to or below the noise floor of the frequency counters used in this experiment. The Cs-clock frequency (10 MHz) is also distributed over a low phase noise coaxial cable. The clock signal as transmitted by the coaxial cable is compared with that transmitted by the White Rabbit network to verify the consistency of the two frequency distribution systems. The beat note frequencies between the ECDLs and the OFC are counted and logged on a computer via software implemented in LabView. Another software application operated on the same computer uses the logged rf beat note frequencies to calculate the drift of the Hz laser and apply an appropriate frequency correction to the ECDLs quasi-continuously, as described above. The frequency of the ECDL at 1442 nm is kept fixed and that of the ECDL at 1445 nm is scanned while searching for the Doppler-free two-photon resonance. The frequency of the 1445 nm laser is changed by changing its virtual beat note frequency with respect to the Hz laser, which is set by the lab PC running the spectroscopy experiment over the White Rabbit timing distribution network via the TCP/IP protocol. A schematic of the White Rabbit timing distribution network as used in our laboratory is shown in Fig. 3.9 below.

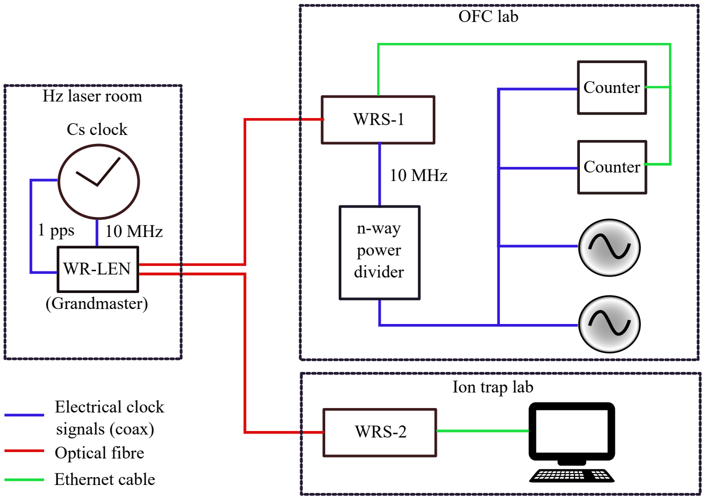

**Figure 3.9:** Simplified schematic of the White Rabbit data and time and frequency distribution network as implemented in our experiment. Cs clock, caesium atomic clock; WRS, White Rabbit Switch (Seven Solutions); WR-LEN, White Rabbit Lite Embedded Node (Seven Solutions). The WR-LEN is configured as the Grandmaster and the White Rabbit switches WRS-1 and WRS-2 are configured in slave mode and connected to the Grandmaster via optical fibres. The optical signal carries both Gigabit Ethernet data as well as time and frequency information, and is converted into an electrical signal and vice versa by optical small form-factor pluggable (SFP) transceivers at the input/output port of the WRS or WR-LEN. The computer and the counters are connected to the WRS with Ethernet cable via so-called "copper SFPs", which have an RJ45 port instead of a fibre-optic port.

### Performance of the frequency stabilisation scheme

One commonly applied method to determine the 3dB linewidth of an ultra-stable laser of linewidth ∼1 Hz is the optical heterodyne method [133]. In this method, a beat note is generated between the laser under test with another similar but independent laser with comparable or known linewidth. Assuming that the spectral lineshape of both the lasers is known (Lorentzian in most cases), linewidths of the individual lasers can be determined.

In our case, no second laser with spectral purity comparable to the Hz laser was available. An alternate method is to use delayed self-heterodyne detection [134]. In this method, light from the laser under test is split into two parts: one part is sent via a long fibre-optic delay-line with path length much longer than the coherence length of the laser and the other part is shifted in frequency by an AOM. Then both parts are heterodyned on a fast photodiode and a beat note around the AOM modulation frequency. However, for lasers with linewidth less than 1 kHz, the coherence lengths of these lasers are larger than 200 km (in optical fibres). Moreover, the optical fibre also has to be kept thermally, mechanically and acoustically isolated so as to not introduce any further linewidth broadening effects, which would require complex mitigation measures such as interferometric length measurement and active length compensation. Nevertheless, such a measurement was performed to at least qualitatively assess the spectral narrowing of the spectroscopy lasers, as will be discussed later in this section. Ultimately, an upper limit to the linewidth of the spectroscopy lasers can also be determined from the Doppler-free two-photon spectrum by fitting it with a line-shape model incorporating the laser line-widths via Eq. 2.8 for the two-photon transition rate $\Gamma_{2\mathrm{ph}}$.

As mentioned above, some indirect qualitative inferences can be drawn regarding the performance of the PLL stabilising the phase of the spectroscopy lasers to the Hz laser. When the lock is engaged, and the ECDL frequency is manually tuned into the capture range of the PLL, the phase-lock is established. The spectroscopy lasers can then be tuned over the entire pass-band of the band-pass filters used in the PLL while keeping the phase-lock intact. The in-loop virtual beat note as recorded using a rf-spectrum analyser (Rohde & Schwarz, FPC1000 Spectrum Analyzer) is shown in Fig. 3.10. The feedback-loop bandwidth can be inferred to be $\sim$250 kHz from the “servo bumps” in Fig. 3.10.

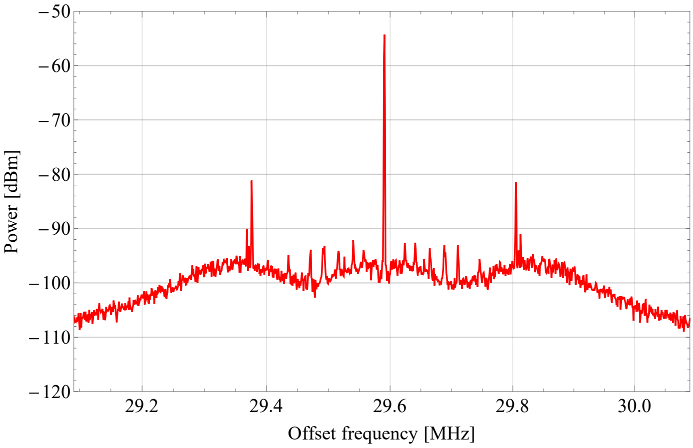

**Figure 3.10:** In-loop beat note of the 1442 nm laser while phase-locked to the Hz laser. The spectrum was recorded using an rf spectrum analyser (Rohde & Schwarz, FPC1000 Spectrum Analyzer) with resolution bandwidth (RBW) of 1 kHz and video bandwidth (VBW) of 300 Hz.

The overlapping Allan deviation of the spectroscopy laser at 1442 nm (similar data obtained for the ECDL at 1445 nm) is plotted in Fig. 3.11a below with respect to a mode of the OFC, referenced to the caesium atomic clock. The overlapping Allan deviation plot for the Hz laser frequency stability relative to OFC (and thereby ultimately the caesium clock) is shown in Fig. 3.11b for reference. The similarity in the Allan deviations can be used to infer qualitatively that the feedback provided by the FALC to the ECDLs successfully tracks the phase of the Hz laser without too many cycle slips (i.e. the number of potential cycle slips does not affect the accuracy of the virtual beat note frequency at the common instability levels shown in Figs. 3.11a and 3.11b).

A delayed self-heterodyne measurement of the spectroscopy lasers was performed for the two ECDLs operated in either free-running mode, or while locked to the OFC, or to the Hz laser through the virtual beat note (Fig. 3.12). The self-heterodyne setup consisted of a fibre-optic Mach-Zehnder interferometer, based on fibre-optic splitters/combiners (90%-10% at the input and 50%-50% at the output of the interferometric setup), having a 25-km-long fibre-optic spool in one arm, and an AOM with a frequency offset of 59.3 MHz in the other. Note that this interferometer is insensitive to noise with Fourier frequencies below the inverse delay difference of the two arms, i.e. noise below 8 kHz. The laser linewidths determined through this method must therefore be considered lower bounds to their true values. The 25 km of fibre was in a

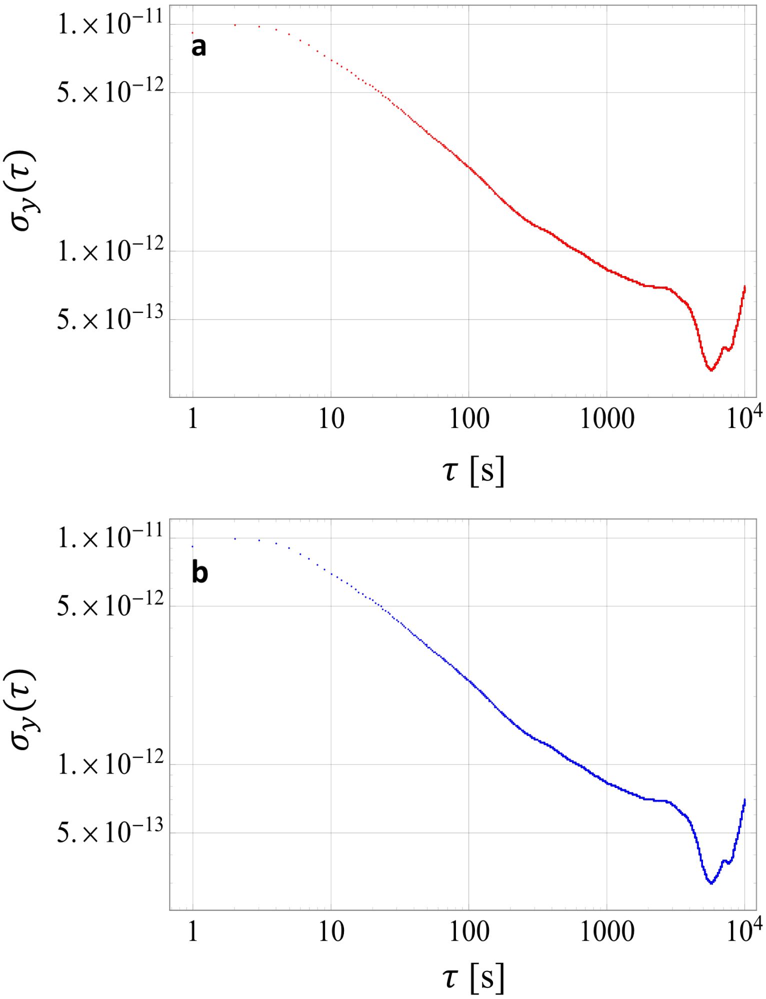

**Figure 3.11:** Overlapping Allan deviation plot of the spectroscopy laser at 1442 nm in (a) and the ultra-stable Hz-linewidth laser in (b). Data was recorded using an FXM50 frequency counter for about 6 hours.

spool kept in a wooden box to provide some isolation. All the measurements were done on the same day in a short span of time, which is to make sure that the slow length variations of the fibre (which lead to an effective Doppler shift of the fibre output optical frequency relative to the input optical frequency) introduced by the optical fibre due to external perturbations occurred at more or less the same rate. Hence, any difference in the delayed self-heterodyne spectrum of the lasers would be an indication of the spectral quality of the spectroscopy lasers and thereby the frequency and phase reference to which they are stabilised. The results of these measurements can be seen in Fig. 3.12 for the ECDL at 1442 nm and is similar for the ECDL at 1445 nm.

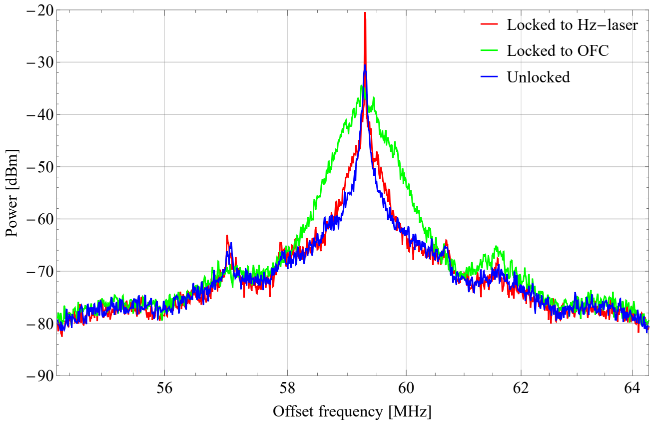

**Figure 3.12:** Delayed self-heterodyne measurement for the ECDL at 1442 nm. The spectrum was recorded using an rf spectrum analyser (Rohde & Schwarz, FPC 1000 Spectrum Analyzer) with a span of 10 MHz, RBW of 10 kHz and VBW of 300 Hz.

From Fig. 3.12, it can be clearly observed that the Hz laser provides a much better phase reference than the optical frequency comb. It is also interesting to note here that the grating-stabilised ECDLs have better noise characteristics than the frequency comb laser in use for noise at higher Fourier frequencies. In Fig. 3.13, we can observe the fringes (side-lobes) due to the interference between the two arms of the interferometer used in the self-heterodyne measurements with the ECDL locked to the Hz laser. This indicates that with the spectroscopy laser stabilised to the Hz laser, the coherence length is $\geq$25 km. The interference fringes with an FSR of $\sim$8 kHz is consistent with the delay introduced by the 25 km fibre spool.

### Effect of intra-office optical fibre on the spectra purity of the lasers

The infrastructure of the experiment is such that the spectroscopy laser and the frequency stabilisation infrastructure is in one laboratory, while the ion-trap

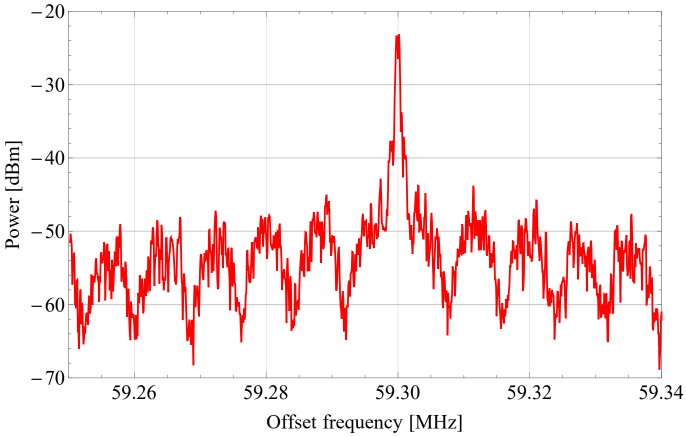

**Figure 3.13:** Delayed self-heterodyne measurement for the ECDL at 1442 nm while phase-locked to the Hz laser. The spectrum was recorded using an rf spectrum analyser (Rohde & Schwarz, FPC 1000 Spectrum Analyzer) with a span of 100 kHz, RBW of 100 Hz and VBW of 100 Hz.

setup is located in another. Spatially they are separated by ∼40 m, and they are connected by a 40 m long optical fiber, shielded by PVC flexible tubing for protection. Hence, light from the spectroscopy lasers had to be transferred to the ion trap via optical fibre. The Hz laser is installed in a temperature-controlled room ∼20 m away from the frequency comb and the spectroscopy laser setup. So, the light from the Hz laser had also to be transferred via optical fibre to the OFC for the frequency stabilisation. The optical fibres also introduce phase noise in the optical signal that is being transmitted through them. This additional noise introduced by the fibre is primarily because of optical path length fluctuations of thermal and acoustic origin, which lead to apparent phase variations through the Doppler effect (the end of the optical fibre appears to be moving with respect to its input). There are schemes with which this additional noise introduced by the optical fibres can be compensated with a feedback loop [135,136], a technology also available at Vrije Universiteit Amsterdam [137].

The linewidth broadening of the frequency stabilised spectroscopy lasers in a round trip through the 40 m long optical-fibre was measured to be ∼200 Hz (Fig. 3.14). From this measurement, the linewidth broadening due to single-pass through the 40 m optical fibre is estimated to be ∼70 Hz [138]. Based on the measurement of linewidth broadening of the ECDL, the broadening due to the 20 m long optical fibre of the Hz laser linewidth was estimated to be

<50 Hz, which is sufficient for the target experimental accuracy. Hence, for this experiment no fibre-optic noise cancellation scheme was implemented.

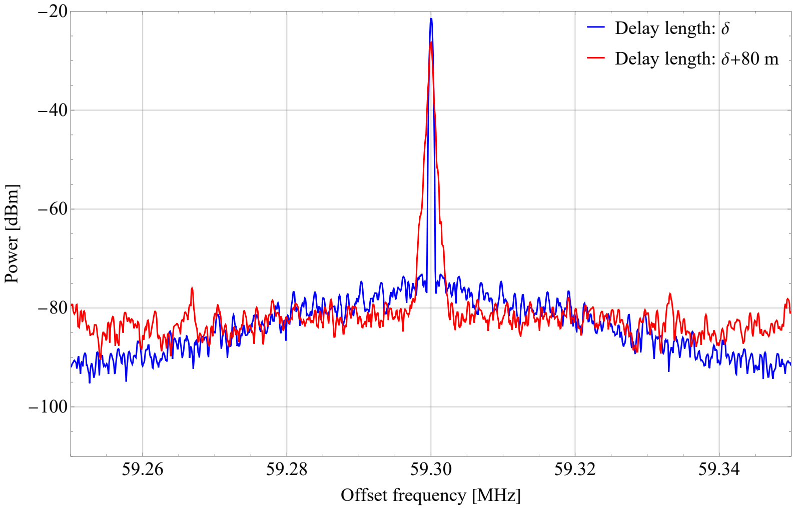

**Figure 3.14:** Delayed self-heterodyne beat note measurement for estimating linewidth broadening due to the 40 m long uncompensated fibre-optic link between the lab in which the spectroscopy lasers are and the lab in which the ion trap is located. The delay length $\delta$ represents the small delay between the two arms of the interferometric set up for the self-heterodyne measurements due to additional length of 2 m patch cord, mating adapters and the AOM. Any difference between the two traces is due to the 80 m (round-trip) of optical fibre.

### Selection of $f_{\text{rep}}$ of the OFC for multiple lasers

The Hz laser and the OFC are part of a common infrastructure shared by different experimental groups. Hence, the $f_{\text{rep}}$ and $f_0$ had to be chosen such that the different experiments that require the OFC can run simultaneously. The frequency comb was used by a number of experiments, either for frequency stabilisation or for absolute frequency calibration, and in all cases involved the generation of a beat note between the relevant lasers with the nearest mode of the OFC. In principle, any value of $f_{\text{rep}}$ and $f_0$ may be used for such a purpose. However, impossibility to obtain commercial off-the-shelf rf band-pass filters for any desired operational frequency limited the choices to a few values of $f_{\text{rep}}$ and $f_0$. The choice of the beat note frequencies were even more stringent for this experiment due to the implementation of the transfer-oscillator frequency stabilisation scheme for the two spectroscopy lasers. Hence, a software routine was written in Python to take into consideration all the laser frequencies and the beat notes required by them to find out viable $f_{\mathrm{rep}}$ and $f_0$ values to be used.

The beat note of the Hz laser with the nearest OFC mode was fixed to be within 57-63 MHz, the pass-band of MiniCircuits BBP-60+ band-pass filters. With this fixed, a set of linear equations was solved to find out the possible choices for $f_{\mathrm{rep}}$ and $f_0$ such that all the lasers can be at beat notes within the pass-band of commercial off-the-shelf band-pass filters. The $f_{\mathrm{rep}}$ and $f_0$ thus chosen were 249.719551 MHz and +20 MHz, respectively.

Chapter 4

# *A priori* determination of required experimental parameters

## 4.1 Introduction

The feasibility study of the Doppler-free two-photon spectroscopy of Ref. [87] provided a compelling indication of its experimental realisation. Yet, a number of open questions are left to be answered, such as the expected signal-to-background level which is achieved if the Doppler-broadened signal of other hyperfine components is also taken into account, the actual two-photon transition rate for the hyperfine component under study (given its magnetic substates and the polarisation of the probe radiation), the precision with which Zeeman shifts and AC Stark shifts due to the cooling and dissociation lasers can be determined, and how to determine the spin-averaged transition frequency from the hyperfine component whose frequency has been measured. This Chapter addresses the open questions through an extended rate equation model, and theoretical calculations of the Zeeman and Stark shifts. The results of this Chapter form the basis on which the most suitable experimental conditions and target hyperfine states for the two-photon spectroscopy are determined and selected.

## 4.2 Choice of hyperfine components[1]

As mentioned in Sec. 2.3.1, $HD^+$ has an unpaired electron, leading to relatively large Zeeman shifts at typical magnetic field strengths in the experimental apparatus. In the ion trap setup used in the present experiment, a static magnetic field $\mathbf{B}$ (directed along the trap-axis parallel to the propagation direction of the cooling radiation at 313 nm) provides the quantisation axis so that the $Be^+$ ions can be laser-cooled by a single circularly polarised beam at 313 nm. This static magnetic field can be reduced to $\sim 20$ mG and still be sufficiently strong and well oriented for efficient cooling of the $Be^+$ ions to $\sim$10 mK secular temperature. The magnetic field magnitude $|\mathbf{B}| \sim 20$ mG sets the limit to which the Zeeman splittings of the hyperfine components will affect the width of the lineshape. To enhance the two-photon transition rate $\Gamma_{2\text{ph}}$, the Zeeman subcomponents need to be addressed all together. Hence, a hyperfine component is preferred with a Zeeman splitting comparable to or less than the laser linewidth (plus the possible additional linewidth caused by power broadening) at $\sim 20$ mG magnetic field. Another important factor contributing to the choice of hyperfine components is the suppression of Doppler-broadened background, not only due to sequential two-photon excitation via the chosen intermediate hyperfine level in $(v = 4,\ L = 2)$, but also due to adjacent hyperfine components. Furthermore, it is also important to have significant population in the chosen hyperfine level of $(v = 0,\ L = 3)$ as that would lead to a stronger REMPD signal, leading to improved signal to background ratio for the Doppler-free peak. All these factors will be discussed in the followings subsections, culminating in a choice of hyperfine component that will be measured in the Doppler-free two-photon experiment.

### 4.2.1 Zeeman shifts

To calculate the Zeeman shifts, the effective spin hamiltonian for a ro-vibrational level $(v, L)$, $H_{\text{eff}}^{total}$ is written as [87, 139]

$$H_{\text{eff}}^{total} = H_{\text{eff}} + E_{10}(\mathbf{L} \cdot \mathbf{B}) + E_{11}(\mathbf{I_p} \cdot \mathbf{B}) + E_{12}(\mathbf{I_d} \cdot \mathbf{B}) + E_{13}(\mathbf{s_e} \cdot \mathbf{B}). \quad (4.1)$$

In Eq. 4.1, $H_{\text{eff}}$ is the field-free effective spin hamiltonian as introduced in Eq. 2.2. The rest of the terms in Eq. 4.1 represent the interaction of the $HD^+$ ions in the relevant level $(v, L)$ with a magnetic field $\mathbf{B}$ directed along the

---

[1] Parts of this section have been published in Ref. [58], of which the author of this thesis is also a co-author.

quantisation axis (trap axis). The coefficients can be expressed as [87]

$$E_{10} = -\mu_B \sum_i \frac{Z_i m_\mathrm{e}}{m_i} \frac{\langle vL||L||vL\rangle}{\sqrt{L(L+1)(2L+1)}} \tag{4.2a}$$

$$E_{11} = -\frac{e\mu_\mathrm{p}}{m_\mathrm{p}c} = -4.2577 \text{ kHz G}^{-1} \tag{4.2b}$$

$$E_{12} = -\frac{e\mu_\mathrm{d}}{2m_\mathrm{d}c} = -0.6536 \text{ kHz G}^{-1} \tag{4.2c}$$

$$E_{13} = -\frac{e\mu_\mathrm{e}}{m_\mathrm{e}c} = 2.8024952 \text{ MHz G}^{-1}. \tag{4.2d}$$

Here, $\mu_B$ is the Bohr magneton, $e$ stands for the electron charge, and $m_\mathrm{p}$, $m_\mathrm{d}$, $m_\mathrm{e}$, $\mu_\mathrm{p}$, $\mu_\mathrm{d}$ and $\mu_\mathrm{e}$ are the masses and magnetic moments of the proton, deuteron, and electron, respectively. For the calculations of the values of $E_{11}$, $E_{12}$, $E_{13}$, the CODATA-14 set of fundamental physical constants were used. $E_{10}$ was calculated using non-relativistic variational wavefunctions from Ref. [140]. The values obtained for $E_{10}$ thus were $-0.55792$ kHz G$^{-1}$ and $-0.50281$ kHz G$^{-1}$ for $(v = 0,\ L = 3)$ and $(v = 9, L = 3)$ respectively. From Eqs. 4.2a, it can be inferred that the interaction of the electron spin $\mathbf{s}_\mathrm{e}$ with $\mathbf{B}$ is the dominant effect contributing to the Zeeman shift. of the ro-vibrational levels in HD$^+$.

In the presence of a magnetic field $\mathbf{B}$, each hyperfine level with total angular momentum $J$ splits into $2J + 1$ sub-levels. The differential Zeeman shifts of the initial and final states define the Zeeman shift to the two-photon transition. It was found in Ref. [87] that some hyperfine components connecting homologous spin states (states with same spin quantum numbers $(F, S, J)$) in $(v = 0,\ L = 3)$ and $(v = 9,\ L = 3)$ benefit from strong cancellation of Zeeman shifts. A number of such choices were mentioned in Ref. [87], which are tabulated below in Table 4.1, where the net Zeeman shifts are ∼10 Hz for $|\mathbf{B}| = 20$ mG.

|  | $(F,S)=(0,1)$ | $(F,S)=(1,1)$ | $(F,S)=(1,2)$ |  |
|---|---|---|---|---|
| $(v,L)$ | $J=4$ | $J=4$ | $J=5$ | $J=1$ |
| (0,3) | 6.8549 | −18.0662 | −27.9358 | 14.0003 |
|  | −6.8564 | −18.0652 | 27.9358 | −14.0137 |
| (9,3) | 6.1161 | −18.0820 | −27.9391 | 13.9928 |
|  | −6.1179 | −18.0807 | 27.9391 | −14.0167 |
| $(0,3) \rightarrow (9,3)$ | −0.7388 | 0.0158 | 0.0033 | −0.0075 |
|  | −0.7385 | 0.0155 | 0.0033 | −0.003 |

**Table 4.1:** Hyperfine states of the $(v=0, L=3)$ and $(v=9, L=3)$ ro-vibrational states with minimum net Zeeman shifts at 20 mG magnetic field. The Zeeman shifts are expressed in kHz and are shown for $M_J = -J$ (upper line) and $M_J = +J$ (lower line). It should however be noted here that the two-photon transitions with $\Delta M_J = 0$ only benefit from the cancellation of Zeeman shift. Table reproduced from Ref. [87].

### 4.2.2 Suppression of Doppler-broadened background

In Section 2.3.2 and in Ref. [58], it was mentioned that the 4-level OBE model does not take into account the densely packed hyperfine structures of both $(v,L)$ : $(0,3) \rightarrow (4,2)$ and $(4,2) \rightarrow (9,3)$ ro-vibrational transitions during the REMPD dynamics. The closely spaced hyperfine components provide additional contributions to the Doppler-broadened background, which consequently leads to a reduced signal-to-background ratio for the Doppler-free two-photon peak. To assess whether a hyperfine component can be found which allows sufficient isolation from the Doppler-broadened single-photon lineshape, it is imperative to study the single-photon Doppler-broadened spectrum of $(v,L)$ : $(0,3) \rightarrow (4,2)$ transition, as this step leads to the accumulation of population in $(v=4,\ L=2)$, which in turn leads to Doppler-broadened background. As described also in Ref. [58], a first approximation is to assume that the second photon (at 1445 nm) together with the 532 nm photon leads to dissociation of any population in $v=4$ with unit probability (later in this chapter it will be shown that this represents a worst-case scenario, and a more refined model will be presented there). In this case it suffices to compute the Doppler-broadened single-photon REMPD spectrum of the $(v,L) : (0,3) \rightarrow (4,2)$ transition. This was done using the rate-equation method developed by Biesheuvel *et al.* in Refs. [33, 86] to simulate the single-photon $(v,L)$ : $(0,3) \rightarrow (4,2)$ spectrum with parameters used in the experimental setup.

In Fig. 4.1, the potential target hyperfine components of the $(v,L) : (0,3) \rightarrow (4,2)$ transition which can lead to Doppler-free two-photon transitions with minimum net Zeeman shifts are shown. As can be observed from the simulated spectrum in Fig. 4.1, the signal is very strong in the central parts.

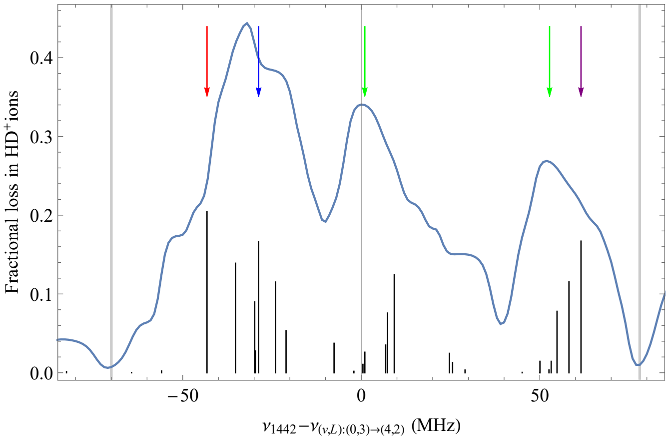

**Figure 4.1:** Simulated Doppler-broadened single-photon spectrum of the $(v, L)$ : $(0, 3) \rightarrow (4, 2)$ transition at 1442 nm, assuming detection by measuring HD$^+$ loss, due to dissociation with unit probability by the 1445 nm and 532 nm photons. The spectrum was calculated for REMPD duration of 10 s, an ambient BBR temperature of 300 K, an HD$^+$ ion secular temperature of 10 mK and 5 mW of laser power focused in a beam waist of 150 $\mu$m. The theoretical hyperfine transitions are indicated by the vertical black sticks. Hyperfine components of special interest are colour-coded as follows: red $(F, S) : (1, 2), J = 5 \rightarrow J' = 4$, blue $(F, S), (1, 1), J = 4 \rightarrow J' = 3$, green $(F, S) : (1, 2), J = 1 \rightarrow J' = 0, 2$, purple $(F, S) : (0; 1), J = 4 \rightarrow J' = 3$. The graphs in this figure were also published in Ref. [58].

So, assuming the worst-case scenario, for which any population accumulated in $(v = 4,\ L = 2)$ due to the laser at 1442 nm $(\omega)$ gets dissociated by the 1445 nm laser $(\omega')$ addressing the $(v, L) : (4, 2) \rightarrow (9, 3)$ transition, any hyperfine component selected in the centre of the spectrum would suffer from strong Doppler-broadened background, leading to poor signal to background or even invisibility of the Doppler-free two-photon peak [87]. Hence, it is desirable to have a hyperfine component which is located near the outer wings of the $(v, L) : (0, 3) \rightarrow (4, 2)$ ro-vibrational spectrum, while choosing the detuning $\delta_{12}$ of the 1442 nm laser such that its interaction with the stronger hyperfine components in the centre of the spectrum is minimised. These additional criteria (apart from the requirement of a small Zeeman shift) can be met by the components starting from the hyperfine levels $(F = 1, S = 2, J = 5)$ and $(F = 0, S = 1, J = 4)$ in the $(v = 0, L = 3)$. Of these two, the component starting with $(F = 0,\ S = 1,\ J = 4)$ can be probed with minimum detuning $\delta_{12}$ of the 1442 nm laser. The relevant detunings of the 1442 nm laser for which the Doppler-broadened background will be minimum are marked by the grey vertical lines in Fig. 4.1. However, it might be possible to probe these transitions with even smaller detunings than shown in Fig. 4.1 due to hyperfine state selectivity by the 1442 nm laser. This possibility will be studied further in Sec. 4.3. Of the two choices of hyperfine components starting with $(F = 1,\ S = 2,\ J = 5)$ and $(F = 0,\ S = 1,\ J = 4)$ in $(v = 0,\ L = 3)$, the former has higher spin multiplicity leading to higher population and thereby stronger REMPD signal. This led to the choice of the component starting with $(F = 1,\ S = 2,\ J = 5)$ in $(v = 0,\ L = 3)$ as the preferred hyperfine component to be measured in the Doppler-free two-photon spectroscopy experiment.

## 4.3 Modelling the Doppler-free two-photon spectrum: *a priori* determination of required experimental parameters

From the preceding section is clear that experimental conditions such as detunings and intensities of the spectroscopy lasers as well as REMPD duration need to be chosen carefully to optimise the signal-to-background and signal-to-noise ratios. Given the slow rate of data acquisition (a typical spectrum is expected to be acquired over a time period of several weeks) an experimental optimisation procedure would be extremely time consuming. It is therefore useful to develop a numerical lineshape model that faithfully describes the expected Doppler-free two-photon spectrum, so that the dependence of signal strength on experimental conditions can be investigated quickly for a wide range of parameters. The same model can also be used to determine *a priori* favourable experimental parameters such as appropriate laser detunings ($\delta_{12}$ and $\delta_{23}$), REMPD duration and HD$^+$ secular temperature for a two-photon signal with good signal-to-background ratio.

As discussed in Chapter 2 following Ref. [87], the preferred detuning $\delta_{12}$ for optimal visibility of the Doppler-free two-photon signal is slightly greater than $\Gamma_\mathrm{D}$, the Doppler width of the $(v, L) : (0, 3) \rightarrow (4, 2)$ transition at the HD$^+$ ion secular temperature $T_{\mathrm{HD}^+}$ (at a typical temperature of 10 mK, $\Gamma_\mathrm{D} = 8.6$ MHz). If $\delta_{12} \geq \Gamma_\mathrm{D}$, the REMPD signal contribution due to the sequential Doppler-broadened two-photon excitation via the chosen hyperfine state in the intermediate level $(v = 4,\ L = 2)$ is minimised. However, interaction of the 1442 nm laser with the line profiles of the adjacent hyperfine components may lead to increased Doppler-broadened background. This contribution to the background is incoherent and can be adequately described by the rate equation model developed in Refs. [33,86], which is computationally far less intensive than solving a set of OBEs involving all the hyperfine levels concerned. However, to faithfully describe the expected two-photon spectrum, it is essential to include not only the laser-induced interactions between the relevant ro-vibrational levels, but also to include BBR-induced interactions between all ro-vibrational levels with $v$ ranging from 0 to 4. Spontaneous emission from $v = 9$ is not considered under the assumption that the dissociation rate is large enough to ensure that any HD$^+$ ions excited to $v = 9$ by the lasers will be efficiently dissociated within its radiative lifetime. The treatment also includes physical parameters like HD$^+$ ion secular temperature $T_{\mathrm{HD}^+}$, REMPD duration, ambient BBR temperature, saturation and depletion effects due to finite-sized sample of HD$^+$ in the ion trap, laser powers and linewidths leading to a faithful representation of the expected two-photon spectrum. In the next few subsections, this extended rate-equation model will be described and its results discussed.

### 4.3.1 Brief review of the rate equation model

The sample of HD$^+$ ions in the trap can be represented by a state vector $\rho(t)$ which describes the population of all 310 hyperfine states of the ro-vibrational levels ($v = 0...4, L \leq 5$). We ignore rotational levels $L \geq 6$ in the $v = 0$ manifold as they contain less than 2.4% of the HD$^+$ population at a typical ambient BBR temperature of 300 K, thus making the problem computationally less intensive. Summing all the elements of $\rho(t)$ gives a measure of the sample population, which can be used to construct a simulated REMPD signal based on the fractional loss of molecules from the sample. The hyperfine structure arises from the interaction between the nuclear and the electronic spins. The Zeeman substructure is ignored for the typical magnetic field values used during the experiment, which lead to Zeeman sub-components well encapsulated within the Doppler-broadened line profile ($\sim$ 8.6 MHz width) at 10 mK translational temperature of the ions. During REMPD, the ions interact with the probe and dissociation lasers as well as the BBR field at 300 K. It is important to note that the interaction with BBR gives rise to a temperature $\sim$300 K of the internal degrees of freedom of the HD$^+$ molecular ions, whereas their external degrees of freedom are $\sim$10 mK by virtue of the sympathetic cooling by the laser-cooled Be$^+$ ions. This discrepancy between the internal and external temperatures is possible since the eigenfrequencies of the internal degrees of freedom ($>$ 1 THz) are orders of magnitude larger than the eigenfrequencies of the external degrees of freedom ($\sim$1 MHz), which implies that any interaction between them must be either highly nonresonant or of very high order, and in either case much weaker than the thermalisation processes due to BBR and sympathetic cooling [141]. The time evolution of the molecular state populations during this period can be cast in mathematical form as

$$\frac{d}{dt}\rho(t) = M_{1\mathrm{ph}} \cdot \rho(t) + M_{2\mathrm{ph}} \cdot \rho(t) + M_{\mathrm{BBR}} \cdot \rho(t), \tag{4.3}$$

where $M_{\mathrm{1ph}}$, $M_{\mathrm{2ph}}$ and $M_{\mathrm{BBR}}$ are matrices representing the interaction of the HD$^+$ molecules with the probe lasers through Doppler-broadened single-photon transitions (including sequential excitation to $v = 9$), Doppler-free two-photon transitions to $v = 9$, and the BBR field respectively. $M_{\mathrm{BBR}}$ also includes the process of spontaneous emission. The matrix elements of $M_{\mathrm{1ph}}$ can be written as:

$$M_{\mathrm{1ph},\alpha\alpha} = -\sum_{\alpha'} B_{\alpha\alpha'} D_z \left(\omega - \omega_{\alpha\alpha'}, T_{\mathrm{HD^+}}\right) \frac{I_{\mathrm{probe}}}{c}, \tag{4.4}$$

$$M_{\mathrm{1ph},\alpha\alpha'} = B_{\alpha'\alpha} D_z \left(\omega - \omega_{\alpha\alpha'}, T_{\mathrm{HD^+}}\right) \frac{I_{\mathrm{probe}}}{c}, \tag{4.5}$$

where $M_{\mathrm{1ph},\alpha\alpha}$ represents the diagonal elements describing the loss of population from a state $\alpha$ due to stimulated emission with the summation running over all states $\alpha'$ which can be populated by the stimulating radiation. $M_{\mathrm{1ph},\alpha\alpha'}$ represents off-diagonal elements describing gain in population in the state $\alpha$ from another state $\alpha'$ due to stimulated emission from the latter. Here, $\alpha$ stands for the set of quantum labels $(v, L, F, S, J)$ describing a hyperfine state, and the matrices include all hyperfine states for $v = 0...4$ and $L = 0...5$. $B_{\alpha\alpha'}$ and $B_{\alpha'\alpha}$ are the Einstein coefficients for stimulated absorption and emission between levels $\alpha$ and $\alpha'$ with a transition frequency $\omega_{\alpha\alpha'}$. $D_z$ is a normalised response function integrated over all probe laser frequencies in the frame of the HD$^+$ ions moving in the z-direction (the symmetry axis of the ion trap in this case) with a thermal distribution corresponding to ion temperature $T_{\mathrm{HD^+}}$, $I_{\mathrm{probe}}$ is the intensity of the probe laser and $c$ the speed of light in vacuum. The matrix $M_{\mathrm{BBR}}$ represents the exchange of population between ro-vibrational levels considered here through electric dipole transitions facilitated by the ambient BBR field and spontaneous emission. It has both diagonal and off-diagonal elements. Spontaneous emission is described by the Einstein coefficient for spontaneous emission $A_{\alpha'\alpha}$. The interactions induced by BBR have the general form of $B_{\alpha'\alpha} \cdot W(\omega_{\alpha\alpha'}, T_{\mathrm{BBR}})$ and $B_{\alpha\alpha'} \cdot W(\omega_{\alpha\alpha'}, T_{\mathrm{BBR}})$ corresponding to stimulated absorption and stimulated emission respectively. $W(\omega, T_{\mathrm{BBR}})$ is the ambient BBR spectral energy density and can be expressed as:

$$W(\omega, T_{\mathrm{BBR}}) = \frac{\hbar\omega^3}{\pi^2 c^3} \left(\mathrm{e}^{\frac{\hbar\omega}{k_B T_{\mathrm{BBR}}}} - 1\right)^{-1}, \tag{4.6}$$

where $\hbar$ is the reduced Planck's constant, $k_B$ is the Boltzmann's constant, $\omega$ and $T_{\mathrm{BBR}}$ are the frequency and temperature of the ambient BBR field. Here, $T_{\mathrm{BBR}}$ is 300 K unless mentioned otherwise. The Einstein coefficients $A$ and $B$ used here are obtained following the procedure described in detail by Biesheuvel *et al.* [86].

The Doppler-free two-photon transition is treated as a loss process from the ground level, i.e., the chosen hyperfine component $(F = 1, S = 2, J = 5)$ of

$(v = 0, L = 3)$. This is justified by the assumption of instantaneous dissociation of the HD$^+$ ions (i.e. well within the radiative lifetime of the upper level) following two-photon excitation. The Doppler-free two-photon transition rate can be written as [87]:

$$\Gamma_{\mathrm{2ph}} = \frac{\Omega_{12}^2 \Omega_{23}^2}{\delta_{12}^2} \frac{\Gamma_3^{eff} + 2\Gamma_{\mathrm{FWHM}}}{\delta_{13}^2 + \frac{(\Gamma_3^{eff} + 2\Gamma_{\mathrm{FWHM}})^2}{4}}, \tag{4.7}$$

where $\Gamma_3^{eff}$ is the effective linewidth of the upper level being equal to the sum of its natural linewidth (13 Hz) and the dissociation rate. $\delta_{12}$ is the detuning of the 1442 nm laser from the ground to intermediate level resonance. $\delta_{13}$ is the detuning of the sum of two probe laser frequencies from the two-photon resonance frequency. $\Omega_{12}$ and $\Omega_{23}$ are the Rabi frequencies of the ground-to-intermediate level and intermediate-to-upper level transitions, respectively. $\Gamma_{\mathrm{FWHM}}$ is the linewidth of the probe lasers (same width is assumed for both the spectroscopy lasers). The dissociation rate can be made sufficiently large by increasing the intensity of the dissociation laser to fulfil the assumption made above.

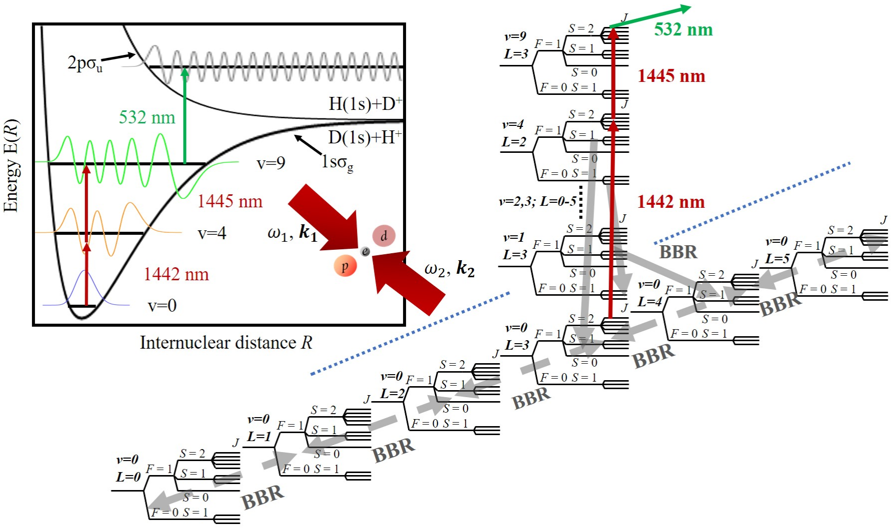

**Figure 4.2:** Partial level scheme of the ro-vibrational levels involved in the two-photon transition to be modelled is shown, indicating the different interactions involved.

The two-photon transition rate $\Gamma_{\mathrm{2ph}}$ as derived by Tran *et al.* [87] can only be applied directly to non-degenerate levels. In case of HD$^+$, most hyperfine states have several degenerate Zeeman substates. Hence, it is necessary to consider the excitations of the individual Zeeman substates and combine them to give a "state-to-state" two-photon transition rate between the concerned hyperfine states in the $(v = 0, L = 3)$ and $(v = 9, L = 3)$ ro-vibrational levels. To this end, it is required to calculate the Rabi frequencies between the individual Zeeman substates of the ground and intermediate states and the intermediate and excited states. Assuming that the Zeeman substates are "nearly degenerate" for the applied magnetic field of 20 mG, $\delta_{12}$ and the lifetimes are considered equal for all of them and the population distribution among them is assumed to be thermal at an ambient BBR temperature of 300 K. We calculate the Rabi frequencies for the so called "$\pi$-transitions", for which the Zeeman levels involved in the transitions have the same magnetic quantum number $M_J$. With these assumptions, a two-photon rate $\Gamma_{2\mathrm{ph},M_{J_g}}$ is calculated for each $M_{J_g}$ level in the ground hyperfine state $J_g$. The effective two-photon rate for the hyperfine state can then be expressed as

$$\Gamma_{2\mathrm{ph},J_g} = \frac{1}{2J_g+1} \sum_{M_{J_g}} \Gamma_{2\mathrm{ph},M_{J_g}}, \tag{4.8}$$

where $\frac{1}{2J_g+1}$ is the normalizing factor.
In Section 4.3.2, the calculations leading to the two-photon spectrum of the $(v, L) : (0, 3) \to (4, 2) \to (9, 3)$ ro-vibrational transition in HD$^+$ are described briefly.

### 4.3.2 Calculation of the $(v, L) : (0, 3) \to (4, 2) \to (9, 3)$ Doppler-free two-photon spectrum: results

The matrices and the matrix elements were built up using *Mathematica*, after which the `NDSolve` algorithm of the same software package was used to numerically solve Eq. 4.3 to find the fractional loss of HD$^+$ ions due to REMPD. By solving Eq. 4.3 for different frequency detunings of the 1445 nm laser, continuous REMPD spectra are obtained. Using this tool to numerically simulate lineshapes, the effects of different detunings of the first (1442 nm) laser, different HD$^+$ temperatures, and longer REMPD durations can be studied. This facilitates the selection of optimum experimental parameters, i.e. the choice of experimental parameters which maximise the signal-to-background and signal-to-noise ratios. For example, in Figs. 4.3 and 4.4, the simulated spectra for the two-photon transition $(v, L) : (0, 3) \to (4, 2) \to (9, 3)$ are plotted for different detunings of the 1442 nm laser from the chosen hyperfine component $(F, S, J) : (1, 2, 5) \to (1, 2, 4)$ of the ground to intermediate ro-vibrational transition $(v, L) : (0, 3) \to (4, 2)$.

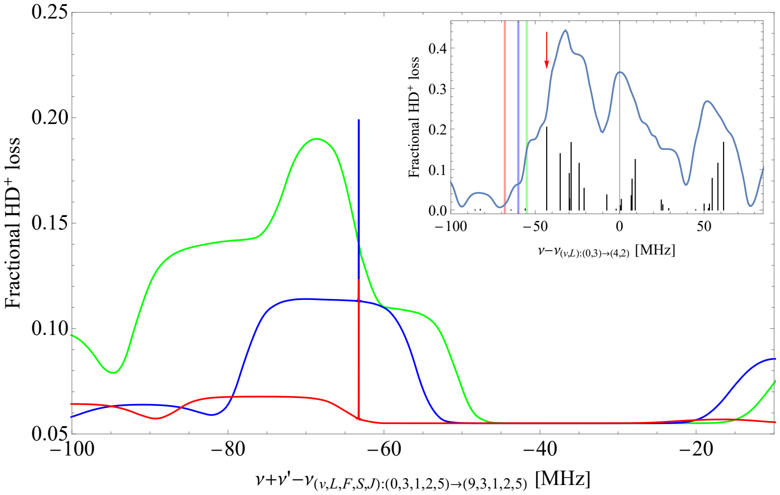

**Figure 4.3:** Simulated two-photon spectra showing a Doppler-free feature on top of a Doppler-broadened background for three different detunings of the 1442 nm laser, assuming 10 s of REMPD. The fractional loss of $HD^+$ ions during REMPD is plotted versus the sum of the frequencies of 1442 nm and 1445 nm lasers relative to the spin-averaged ro-vibrational frequency of the $(v, L) : (0, 3) \to (9, 3)$ transition. The green, blue and red curves correspond to the position of the 1442 nm laser at $-55$ MHz, $-60$ MHz, and $-68$ MHz with respect to the spin-averaged frequency of the $(v, L) : (0, 3) \to (4, 2)$ ro-vibrational transition, respectively. These three detunings correspond to frequency offsets of about $-12$ MHz, $-18$ MHz, and $-25$ MHz from the selected hyperfine component of the $(v, L) : (0, 3) \to (4, 2)$ spectrum, respectively. See also the description of the inset below. The laser beam parameters used for the simulations are the same for both the 1442 nm and 1445 nm lasers: 5 mW of laser light focussed in a beam of waist 150 $\mu$m, while an $HD^+$ ion secular temperature of 10 mK and 300 K BBR temperature were assumed. **Inset:** Simulated spectrum of the single-photon $(v, L) : (0, 3) \to (4, 2)$ transition, obtained with the same parameters as used in the main figure. The stick spectrum represents the theoretical hyperfine structure of the ground-to-intermediate level ro-vibrational transition. The vertical lines represent the frequency detunings of the 1442 nm laser with respect to the chosen hyperfine component (indicated by the red arrow), for which the two-photon spectra of the main figure were obtained, and using the same colour coding scheme.

For a detuning of about $-25$ MHz from the chosen hyperfine component, the Doppler-free two-photon transition is prominently visible on top of a suppressed Doppler-broadened background. For this large detuning, the 1442 nm laser

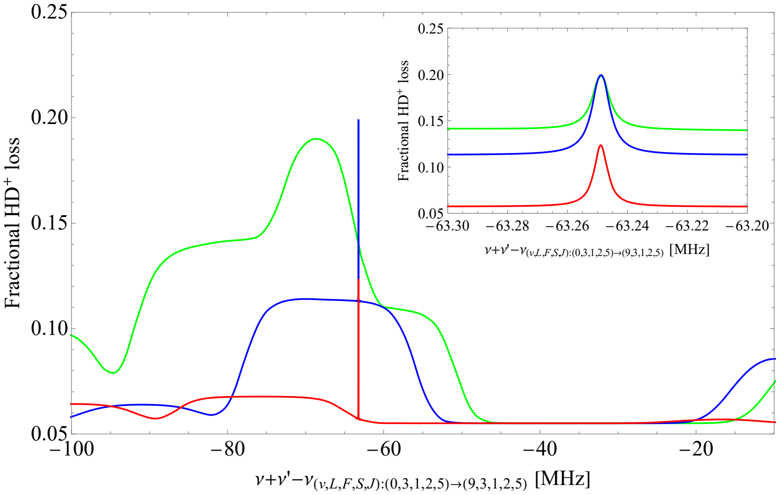

**Figure 4.4:** The same figure as in Fig. 4.3, but with the two-photon spectra shown in a narrow range centred around the Doppler-free two-photon resonance in the **inset**.

interacts weakly with the Doppler-broadened hyperfine transitions, thereby suppressing sequential two-photon excitations. As the detuning is decreased, the overall signal increases at the cost of decreasing visibility of the two-photon peak on top of a significantly higher Doppler-broadened background. With the detuning decreased further towards the chosen resonance, the 1442 nm laser interacts strongly not only with the chosen hyperfine component, but also with adjacent closely spaced ones, leading to considerable additional sequential excitation and subsequent dissociation (green curve in Fig. 4.3). As can be seen from Fig. 4.3, a larger detuning of the 1442 nm laser leads to a favourable signal-to-background ratio, although at the expense of the Doppler-free two-photon signal strength. The decrease in the two-photon excitation rate due to large detuning can in principle be compensated by either increasing the intensities of the probe radiation (albeit at the expense of increased power broadening) or by increasing the duration of REMPD. The latter option is discussed below in some more detail.

In Figure 4.5, the two-photon spectrum is shown for a fixed detuning of the the 1442 nm laser for different HD$^+$ ion secular temperatures. For lower secular temperatures of the HD$^+$ ions, the Doppler widths of individual hyperfine components decrease, leading to smaller backgrounds even for smaller detunings of the laser at 1442 nm.

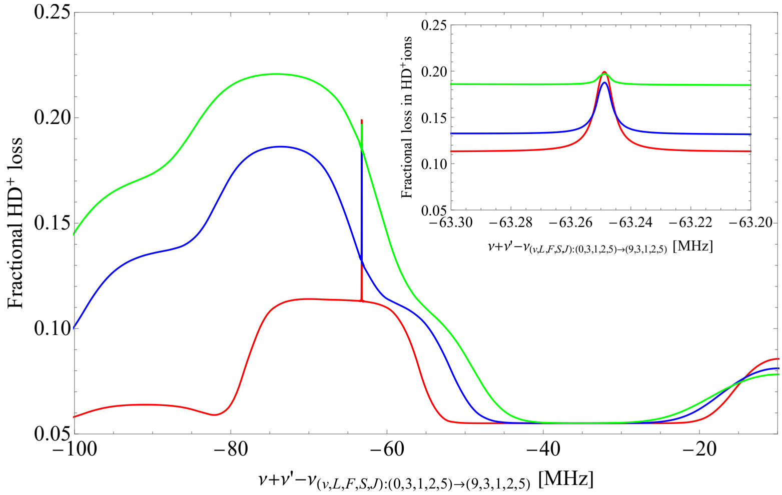

**Figure 4.5:** Simulated two-photon spectra for a fixed detuning of the 1442 nm laser ($-60$ MHz from spin-averaged frequency of the $(v, L) : (0, 3) \rightarrow (4, 2)$ transition) at different secular temperatures of the HD$^+$ ions. The green, blue and red spectra correspond to HD$^+$ ion secular temperatures of 30 mK, 20 mK and 10 mK respectively. All other parameters are the same as used in Figure 4.3. **Inset:** Same spectra shown in a narrow range centred around the Doppler-free two-photon resonance.

It would also be useful to know *a priori* the optimum time for which the transition needs to be probed to obtain an observable dissociation signal corresponding to the Doppler-free transition. With this motivation, in Figure 4.6, simulated two-photon spectra are plotted for different probe durations. As can be expected, the signal increases for longer REMPD durations, which makes it easier to detect.

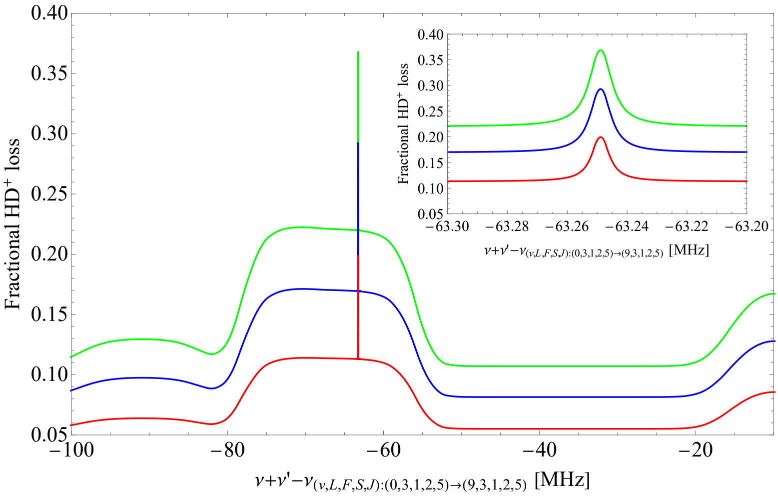

**Figure 4.6:** Simulated two-photon spectra for a fixed detuning of 1442 nm laser (−60 MHz from spin-averaged frequency of the $(v, L) : (0, 3) \rightarrow (4, 2)$ transition) and different REMPD durations. All other parameters are same as in Figure 4.3. The green, blue and red spectra correspond to REMPD durations of 30 seconds, 20 seconds and 10 seconds respectively. **Inset:** Same spectra shown in a narrow range centred around the Doppler-free two-photon resonance.

However, the ∼350 s lifetime of the HD$^+$ ions in the trap (due to loss of ions following collisions with background-gas molecules) should be taken into consideration while choosing the optimum probe duration. For example, for a hypothetical REMPD probe duration of 60 s, the background losses only would lead to a fractional loss of HD$^+$ of about 0.15, which is comparable to (or even larger than) the losses expected from REMPD. As also pointed out in [87], the optimum probe duration therefore depends on the REMPD rate and the population redistribution rate relative to the loss rate due to background-gas collisions. The simulations developed here offer a quantitative tool to analyse the effect of these phenomena on the expected signal strength and visibility. The choice of optimum REMPD duration used in the experiment is further justified in Appendix 7.A.

### 4.3.3 Estimate of frequency shift due to underlying Doppler-broadened background

From Figure 4.3 it can be observed that the Doppler-free peak lies on a non-zero slope of the Doppler broadened background. If not accounted for properly, it can provide a systematic shift in the determination of the transition frequency. To estimate this shift, the simulated spectrum was fitted with a function $L(\nu)$ of the form

$$L(\nu) = \frac{L_0}{\pi} \frac{\frac{\Gamma}{2}}{(\nu - \nu_0)^2 + (\frac{\Gamma}{2})^2} + a\nu + b, \tag{4.9}$$

where $\nu$ is the sum of the frequencies of the probe lasers, $\nu_0$ is the centre frequency, $\Gamma$ the FWHM of the Doppler-free two-photon resonance, and $a$ and $b$ are slope and offset of the Doppler-broadened background (here it is assumed that higher-order terms describing the background signal are negligibly small). The first term on the right-hand side of Eq. 4.9 represents a Lorentzian lineshape, which describes the Doppler-free two-photon peak. The dominant broadening mechanism for the Doppler-free feature is power broadening, which is much larger than the broadening due to Zeeman and AC Stark effects under the typical experimental conditions of magnetic field, laser intensities (see Secs. 4.4.1 and 4.4.2 for a discussion on the expected Zeeman shift due to the static magnetic field **B** and AC Stark shifts due to the 313 nm and 532 nm lasers). Hence, a Lorentzian lineshape can be used to model the expected Doppler-free two-photon peak as a first approximation.

The potential line shift due to the background slope is estimated as follows. First, the numerical simulation model which was also used to produce the spectra of Fig. 4.3 is used to obtain a discrete REMPD spectrum with step size 2 kHz for the narrow Doppler-free feature, and step size 2 MHz for the Doppler-broadened background. Next, the function of Eq. 4.9 is fitted to the discrete spectrum using the `NonlinearModelFit` algorithm of *Mathematica*. Fitted parameters are $L_0$, $a$, $b$, $\nu_0$, and $\Gamma$. This was repeated for the same three values of the intermediate detuning $\Delta_{12}$ as in Fig. 4.3. In Fig. 4.7, the simulated discrete spectrum of the Doppler-free two-photon peak is shown together with the fitted lineshape function $L(\nu)$ for $\Delta_{12} = -60$ MHz.

A line shift due to the background slope would manifest itself as an offset between the frequency, $\nu_{0,\text{sim}}$, of the two-photon transition which was used in the simulation, and the fitted value, $\nu_{0,\text{fit}}$ of the parameter $\nu_0$. The deviation between $\nu_{0,\text{fit}}$ and $\nu_{0,\text{sim}}$, expressed as an absolute frequency difference is shown in Table 4.2 for each value of $\Delta_{12}$. Also shown in Table 4.2 is the uncertainty $\sigma_{\nu_0}$ of $\nu_{0,\text{fit}}$, expressed relative to $\nu_{0,\text{sim}}$.

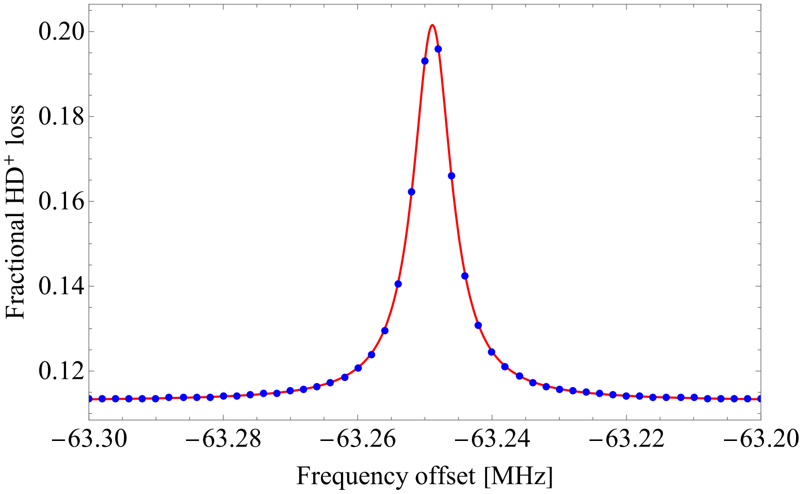

**Figure 4.7:** Simulated spectrum of the Doppler-free two-photon peak (blue dots) for a detuning $\Delta_{12} = -60$ MHz of the 1442 nm laser is shown together with the fitted lineshape function $L(\nu)$ (red curve). All simulation parameters are the same as in Fig. 4.3.

| $\Delta_{12}$ (MHz) | $\nu_{0,\text{fit}} - \nu_{0,\text{sim}}$ (kHz) | $\frac{\sigma_{\nu_0}}{\nu_{0,\text{sim}}}$ |
|---|---|---|
| $-68$ | $-0.0016(23)$ | $5.61 \times 10^{-15}$ |
| $-60$ | $-0.0016(44)$ | $1.06 \times 10^{-14}$ |
| $-55$ | $-0.0021(16)$ | $4.30 \times 10^{-15}$ |

**Table 4.2:** Estimated shift to the position of the Doppler-free peak due to the background slope for various values of $\Delta_{12}$ (first column), obtained using the fit procedure described in the text.

Table 4.2 indicates that no significant line shift is to be expected from the slope of the Doppler-broadened background. To verify this result, the fit was also performed with the slope $a$ set to zero. Table 4.3 displays the difference with the results of Table 4.2 (obtained with $a$ as a free fit parameter).

| $\Delta_{12}$ (MHz) | $\nu_{0,\mathrm{fit}} - (\nu_{0,\mathrm{fit}})_{a=0}$ (kHz) |
|---|---|
| −68 | 0.0007(38) |
| −60 | 0.0002(62) |
| −55 | 0.0121(269) |

**Table 4.3:** Difference in fitted line position for fits treating the slope $a$ as a free fit parameter, and fits assuming $a = 0$. The fit uncertainty is shown between parentheses, and equals the square root of the quadratic sum of the fit uncertainties found in each case. It can be observed that the frequency shift in estimating $\nu_0$ due to the slope of the Doppler-broadened background attains a maximum value of 22.6 Hz for $\Delta_{12} = -55$ MHz. For larger detunings of the 1442 nm laser, the shifts become $\leq 2$ Hz.

As can be seen from Table 4.3, there is no discernible change in the estimation of the centre frequency $\nu_0$ of the two-photon resonance whether the slope of the background is considered or not up to a frequency resolution of $1 \times 10^{-12}$ in relative frequency uncertainty terms. The results of Tables 4.2 and 4.3 imply that the relative line shift due to the background slope, for the range of experimental conditions considered in this experiment, is smaller than $1 \times 10^{-13}$.

## 4.4 Zeeman and AC Stark shifts

### 4.4.1 Zeeman shift

In section 4.2.1, it was mentioned that the selected hyperfine component with $(F = 1, S = 2, J = 5)$ of the $v = 0$ to $v = 9$ two-photon transition has a small net Zeeman shift of about 6.5 Hz at a bias magnetic field of 20 mG. However, in the experiment, such a small bias magnetic field requires carefully shimming out any stray magnetic field in the perpendicular direction to not affect the orientation of the magnetic quantisation axis, and thereby the efficiency of the laser cooling of the Be$^+$ ions. Hence, it would be convenient to use a somewhat larger magnetic field. But at the same time, the Zeeman shift (in particular the Zeeman splitting between the individual Zeeman sub-components) of the transition in question also should be small enough so that all the Zeeman sub-components are addressed by the probe lasers together (i.e. they should all be encompassed by the effective linewidth of the transition) in order to achieve the highest REMPD rate. Based on the discussion in Sec. 3.2.2 of Chapter 3, it can be estimated that the linewidth of the spectroscopy lasers is about 1 kHz. Hence, a magnetic field inducing Zeeman shifts and splittings <1 kHz would be acceptable for the experiment. To find the corresponding acceptable magnetic field value, the Zeeman shifts of the hyperfine components with $(F = 1, S = 2, J = 5)$ in both $(v = 0,\ L = 3)$ and $(9, 3)$ ro-vibrational levels. The Zeeman shifts of the relevant levels were calculated following the method described in Sec. 4.2.1 and the results are plotted in Figs. 4.8-4.9.

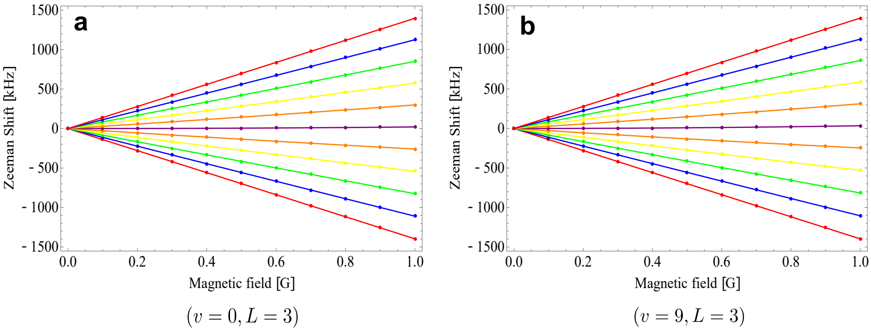

$(v = 0, L = 3)$ $(v = 9, L = 3)$

**Figure 4.8:** Zeeman shifts of the different magnetic components $\Delta M_J = 0$ of hyperfine component $(F = 1, S = 2, J = 5)$ of the ro-vibrational transition $(v = 0, L = 3)$ (a) and $(v = 9, L = 3)$ (b) are shown. Zeeman components with same values of $|M_J|$ are colour-coded as: red, ±5; blue, ±4; green, ±3; yellow, ±2; orange, ±1; purple, 0.

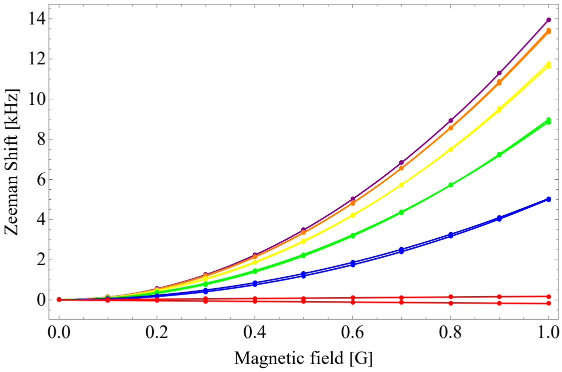

**Figure 4.9:** The differential Zeeman shifts of the various magnetic sub-components with $\Delta M_J = 0$ of the hyperfine component $(F, S, J) : (1, 2, 5) \rightarrow (1, 2, 5)$ of the $(v, L) : (0, 3) \rightarrow (9, 3)$ two-photon ro-vibrational transition are shown. The dots represent Zeeman shifts computed at discrete values of Magnetic field and the curves represent an interpolating function of third order. Zeeman components with same values of $|M_J|$ are colour-coded as: red, ±5; blue, ±4; green, ±3; yellow, ±2; orange, ±1; purple, 0.

As can be seen from Fig. 4.8, the Zeeman shift of the upper ($v = 9$) and lower ($v = 0$) levels is dominated by the linear Zeeman effect, with shifts as large as 1400 kHz for magnetic field strengths of 1 G. However, for the differential Zeeman effect (Fig. 4.9), the linear part cancels out, and a smaller (mostly quadratic) Zeeman shift remains. Figure 4.9 also shows that the magnetic subcomponents of the transition are encapsulated by the 1 kHz laser linewidth for magnetic fields of 0.2 G and below. For comparison, typical magnetic field values used in the experiment are 0.1 G or less, and for these values efficient laser cooling is readily achieved. In addition, at these experimental magnetic field values the overall Zeeman shift is much smaller than 0.5 kHz, which implies that the Zeeman shift due to the bias magnetic field contributes less than $10^{-12}$ to the total two-photon transition frequency.

Since the differential Zeeman effect is quadratic, the Zeeman shift due to AC magnetic fields does not average out to zero over time, and will therefore have to be evaluated too. A possible source of AC magnetic fields is the field produced by the ion trap itself due to rf currents at the trap drive frequency ($\sim$13.2 MHz) [142], the shift due to which is estimated to be $\leq 1$ Hz.

### 4.4.2 AC Stark shift due to the cooling laser at 313 nm and the dissociation laser at 532 nm

The AC Stark effect due to the cooling and dissociation lasers was evaluated theoretically by Jean-Philippe Karr (private communication). The theoretical derivation by Karr is reproduced in Appendix 4.A of this thesis. In Figures 4.10 and 4.11, the AC Stark shifts (due to the 313 nm cooling and 532 nm dissociation lasers) to the lower and upper states of the two-photon transition are plotted for a range of laser intensities.

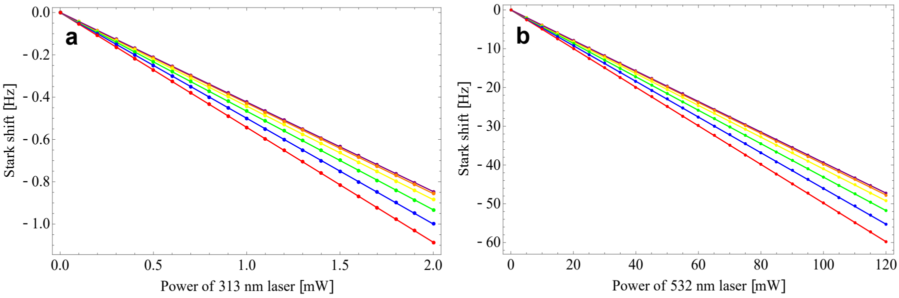

**Figure 4.10:** AC Stark shifts of the different magnetic sub-components of the hyperfine state ($F = 1, S = 2, J = 5$) of the ($v = 0, L = 3$) ro-vibrational level versus laser power due to the Be$^+$ cooling (a) and the dissociation lasers (b) are plotted. A beam waist of 150 $\mu$m is assumed for each laser beam. The dots represent AC Stark shifts calculated for discrete values of laser powers and the curve represents an interpolating function of the second order. The $M_J$ values are colour-coded as follows: red, ±5; blue, ±4; green, ±3; yellow, ±2; orange, ±1; purple, 0.

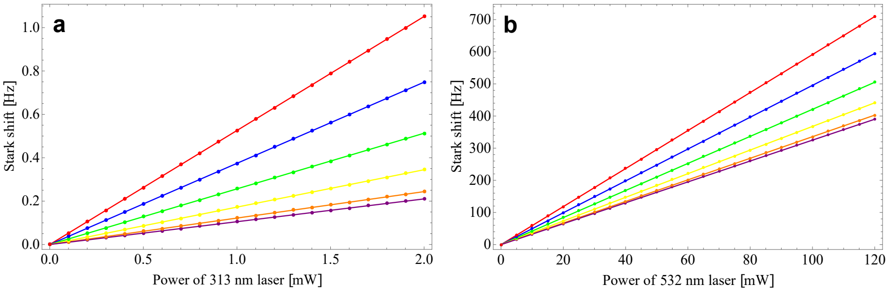

**Figure 4.11:** AC Stark shifts of the different magnetic sub-components of the hyperfine state ($F = 1, S = 2, J = 5$) of the ($v = 9, L = 3$) ro-vibrational level versus laser power due to the Be$^+$ cooling (a) and the dissociation lasers (b) are plotted. A beam waist of 150 $\mu$m is assumed for each laser beam. The dots represent AC Stark shifts calculated for discrete values of laser powers and the curve represents an interpolating function of the second order. The $M_J$ values are colour-coded as follows: red, ±5; blue, ±4; green, ±3; yellow, ±2; orange, ±1; purple, 0.

Figure 4.12 shows the differential AC Stark shifts of the two-photon transition due to the Be$^+$ cooling and the dissociation lasers. For the typical values of the laser power used during the experiment (see Sec. 7.2, Chapter 7), the AC Stark shifts due to the cooling and the dissociation lasers are estimated to be less than 1 kHz.

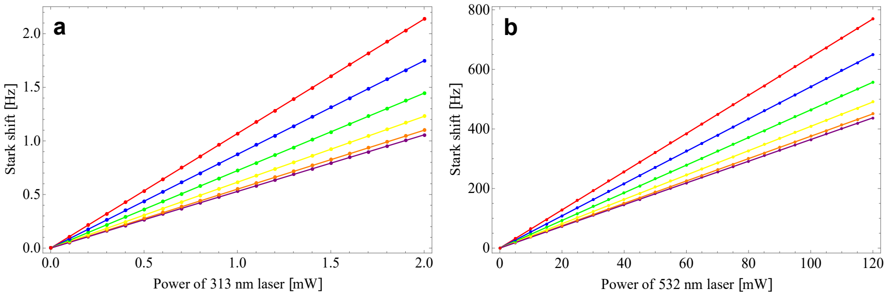

**Figure 4.12:** Differential AC Stark shifts of the various magnetic sub-components of the hyperfine component $(F, S, J) : (1, 2, 5) \rightarrow (1, 2, 5)$ of the $(v, L) : (0, 3) \rightarrow (9, 3)$ two-photon ro-vibrational transition versus laser power due to the Be$^+$ cooling (a) and the dissociation laser (b) are plotted. A beam waist of 150 $\mu$m is assumed for each laser beam. The dots represent AC Stark shifts calculated for discrete values of laser powers and the curve represents an interpolating function of the second order. For ~150 $\mu$W power of the 313 nm laser, the AC Stark shift induced is 0.105 Hz and that for ~90 mW of the dissociation laser is 328.012 Hz for $M_J = 0$. The $M_J$ values are colour-coded as follows: red, ±5; blue, ±4; green, ±3; yellow, ±2; orange, ±1; purple, 0.

## 4.A AC Stark shift due to the cooling laser and the dissociation laser[2]

The AC Stark shift induced by the cooling laser at 313 nm and the dissociation laser at 532 nm can be estimated perturbatively. The change in energy of a particular ro-vibrational level $(v, L, M_L)$ due to a laser of angular frequency $\omega$, intensity $I$ and polarisation state $q$ can be expressed following second order perturbation theory as

$$\Delta E = -\frac{1}{2}\alpha^{q}_{vLM_L}(\omega)\frac{I}{c}, \tag{4.10}$$

where $\alpha^{q}_{vLM_L}(\omega)$ is the dynamic polarisability for the state $(v, L, M_L)$ and $c$ is the speed of light in vacuum. $M_L$ is the magnetic quantum number associated with $L$. The dynamic polarisability $\alpha(\omega)$ can be expressed as

$$\begin{aligned}\alpha^{q}_{vLM_L}(\omega) = 4\pi a_0^3(\, &\langle vLM_L|Q_{qq}(E_{vL}+\hbar\omega)|vLM_L\rangle \\ + \, &\langle vLM_L|Q_{qq}(E_{vL}-\hbar\omega)|vLM_L\rangle).\end{aligned} \tag{4.11}$$

In Eq. 4.11, $Q(E)$ is the two-photon operator (in atomic units)

$$Q_{ij}(E) = \mathbf{d}\cdot\epsilon_{\mathrm{i}}\frac{1}{H-E}\mathbf{d}\cdot\epsilon_{\mathrm{j}}, \tag{4.12}$$

where $H$ is the Hamiltonian of the unperturbed system, $\mathbf{d}$ is the electric dipole operator, and $\epsilon_{\mathrm{k}}(\mathrm{k}=\mathrm{i},\mathrm{j})$ is the polarisation vector. The operator $Q(E)$ can be written as a sum of a scalar component $Q^{(0)}$ and a tensor of second rank $Q^{(2)}$. Then $Q_s$ and $Q_t$ are defined as

$$Q_s = \frac{\langle vL||Q^{(0)}||vL\rangle}{\sqrt{2L+1}} \tag{4.13a}$$

$$Q_t = \frac{\langle vL||Q^{(2)}||vL\rangle}{\sqrt{2L+1}}. \tag{4.13b}$$

In terms of $Q_s$ and $Q_t$, the energy shift $\Delta E$ can be expressed as

$$\Delta E = -\frac{1}{2}\frac{I}{c}4\pi a_0^3\Big[Q_s + \frac{1}{2}(3\cos^2\theta - 1)\frac{3M_L^2 - L(L+1)}{\sqrt{L(L+1)(2L-1)(2L+3)}}Q_t\Big], \tag{4.14}$$

where $\theta$ is the angle of polarisation of the laser light with respect to the quantisation axis. With respect to the static and dynamic polarisabilities $\alpha^{(0)}_{vL}(\omega)$ and $\alpha^{(2)}_{vL}(\omega)$, $\Delta E$ can be expressed as

$$\Delta E = -\frac{1}{2}\frac{I}{c}\Big[\alpha^{(0)}_{vL}(\omega) + \frac{1}{2}(3\cos^2\theta - 1)\frac{3M_L^2 - L(L+1)}{L(2L-1)}\alpha^{(2)}_{vL}(\omega)\Big]. \tag{4.15}$$

---

[2] The derivation of the formulae presented in this section is done by J.-Ph. Karr (private communication) and is reproduced here.

For a hyperfine state $|vLFSJM_J\rangle$, the energy shift $\Delta E$ can be shown to be

$$\Delta E = -\frac{1}{2}\frac{I}{c}4\pi a_0^3 \sum_{F',S'} [\beta_{F'S'}^{vLFSJ}]^2 (-1)^{J+L+S'} \sqrt{(2J+1)(2L+1)} \times \left( \begin{Bmatrix} L & 0 & L \\ J & S' & J \end{Bmatrix} Q_s + \frac{1}{2}(3\cos^2\theta - 1)\frac{3M_J^2 - J(J+1)}{\sqrt{J(J+1)(2J-1)(2J+3)}} \times \begin{Bmatrix} L & 2 & L \\ J & S' & J \end{Bmatrix} Q_t \right) \tag{4.16}$$

Chapter 5

# Ghost features in Doppler-broadened spectra of ro-vibrational transitions in trapped HD$^+$ ions

This chapter has been published earlier in Ref. [143] and is reproduced here without any modifications to the contents. Minor modifications were made in the typesetting.

## 5.1 Introduction

In this chapter, we theoretically study the Doppler-broadened hyperfine structure of the $(v, L) : (0, 3) \rightarrow (4, 2)$ ro-vibrational transition in HD$^+$. This transition is the first step of the two-photon transition proposed by Tran *et al.* [87], which should enable Doppler-free spectroscopy of HD$^+$ at improved resolution. Apart from the Doppler-free signal, a background signal due to Doppler-broadened excitation will be present [59, 87]. To assess the effect of the latter, we employ the model of Biesheuvel *et al.* [33, 86] to study the $(v, L) : (0, 3) \rightarrow (4, 2)$ transition. We find that depending on the conditions (HD$^+$ temperature, transition rates, BBR temperature, and saturation level) this spectrum contains several ghost features, *i.e.* relatively narrow peaks in parts of the spectrum where no signal is expected as there are no nearby hyperfine components. We describe these ghost features in detail and explain their origin, leading us to conclude that such features may be common to any

saturated Doppler-broadened spectroscopy of transitions involving partly overlapping (hyperfine) subcomponents.
This article is organised as follows. In Sec. 5.2, we briefly review the rate equation model that was developed by Biesheuvel *et al.*, followed by the calculation of the $(v, L) : (0, 3) \rightarrow (4, 2)$ spectrum in Sec. 5.3. The ghost features are described in detail in Sec. 5.4, followed by a description of their possible impact in Sec. 5.5 and the conclusions in Sec. 5.6.

## 5.2 Brief review of the rate equation model

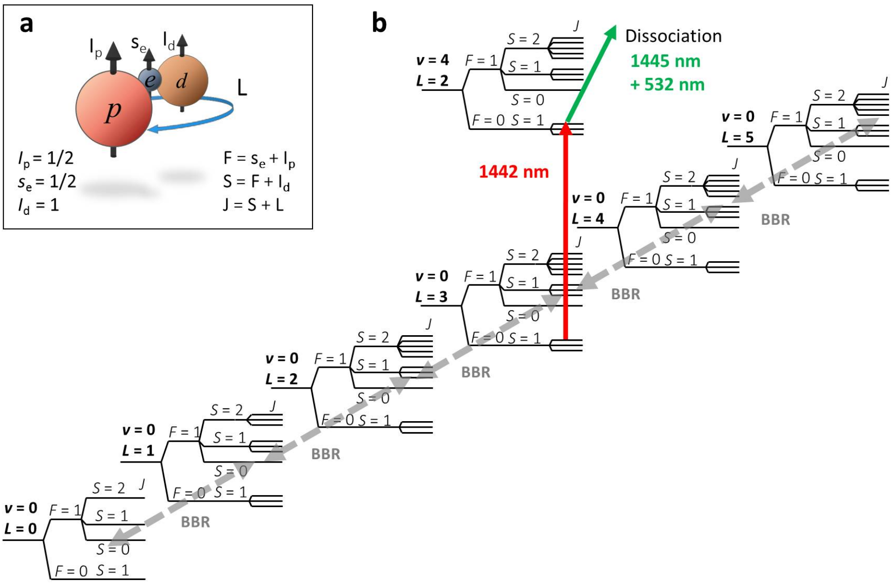

**Figure 5.1:** Partial level scheme (not to scale) of the relevant ro-vibrational and hyperfine levels of HD$^+$ (all in the 1s$\sigma$ ground electronic state), and a schematic representation of the REMPD process. (a) Angular momentum picture of the HD$^+$ molecular ion and the angular momentum coupling scheme used. (b) Rotational levels in $v = 0$ are coupled by BBR and spontaneous emission (gray dashed arrows). The $v = 0, L = 3$ state is probed by the 1442 nm laser, which is subsequently dissociated following a second (resonant) 1445 nm step to $v = 9, L = 3$ and a third 532 nm step which promotes the molecule to the predissociating 2p$\sigma$ electronic state. Although this scheme actually corresponds to $(1+1'+1'')$ REMPD, we treat the final two steps as a single dissociative transition (*i.e.* $(1 + 1')$ REMPD).

The idea here is to describe the sample of $HD^+$ ions by a state vector, $\rho(t)$, describing the population of all 62 hyperfine levels in the $(v = 0, L \leq 5)$ manifold (Fig. 5.1), which contains 97.6% of the population at a BBR temperature of 300 K. Ignoring states with $L > 5$ minimises the computational resources needed for the numerical calculations. A measure of the total number of $HD^+$ ions can be obtained by summing over all elements of $\rho(t)$, from which we can also obtain the spectroscopic REMPD signal (*i.e.* the fractional loss of $HD^+$ due to REMPD). The hyperfine structure arises from magnetic interactions between the proton spin, electron spin, deuteron spin and the molecular rotation, and is described in detail in references [48, 144]. States with $L = 0$, $L = 1$ and $L \geq 2$ possess 4, 10 and 12 hyperfine levels, respectively, each having its own total angular momentum, $J$. We ignore Zeeman splittings and shifts due to typical magnetic fields of $\sim 20$ mG as these are much smaller than the Doppler width of the transition at the 10 mK translational temperature of the $HD^+$ ions. During REMPD, the ions interact both with the probe radiation and the BBR field, and the time evolution of the population in the $v = 0$ manifold is given by the time evolution of the state vector $\rho(t)$ as below,

$$\frac{d}{dt}\rho(t) = M_{\mathrm{REMPD}} \cdot \rho(t) + M_{\mathrm{BBR}} \cdot \rho(t). \tag{5.1}$$

Here, $M_{\mathrm{REMPD}}$ and $M_{\mathrm{BBR}}$ are matrices describing the interactions with the spectroscopy probe laser (which induces the ro-vibrational transition of interest) and the BBR field, respectively. Assuming that the ions which make the transition are instantly dissociated by the dissociation laser allows treating the interaction with the probe radiation as a simple loss process. The matrix $M_{\mathrm{REMPD}}$ is strictly diagonal and its elements can be written as

$$M_{\mathrm{REMPD},\alpha\alpha} = -\sum_{\alpha'} B_{\alpha\alpha'} D_z \left(\omega - \omega_{\alpha\alpha'}, T_{\mathrm{HD}^+}\right) \frac{I_{\mathrm{probe}}}{c}, \tag{5.2}$$

where $B_{\alpha\alpha'}$ is the Einstein coefficient for stimulated absorption between the lower (hyperfine) level $\alpha$ in $(v = 0, L = 3)$ and the upper (hyperfine) level $\alpha'$ in $(v = 4, L = 2)$ with a transition frequency of $\omega_{\alpha\alpha'}$. The summation runs over all upper hyperfine states $\alpha'$ within the target ro-vibrational state. $D_z$ is a normalised response function (typically a Voigt profile), which involves an integration over all probe laser frequencies observed in the frame of the $HD^+$ ions moving with thermally distributed velocities $v_z$ along the z-direction (which coincides with the symmetry axis of the linear Paul trap assumed here, and also with the direction of the wave vector of the cooling laser for $Be^+$ ions). For a thermal velocity distribution characterised by typical translational (secular) $HD^+$ temperatures $T_{\mathrm{HD}^+}$ of several millikelvins, the Doppler width (MHz-range, see Fig. 5.5b) is much larger than the natural linewidth ($\sim 10$ Hz), so that $D_z$ is well described by a Doppler-broadened Gaussian lineshape function. Furthermore, $\omega \equiv 2\pi\nu$ is the angular frequency of the 1442 nm probe laser, $I_{\mathrm{probe}}$ is the intensity of the probe radiation, and $c$ is the speed of light in vacuum.

The matrix $M_{\mathrm{BBR}}$ contains both diagonal and off-diagonal elements, which take into account the rate of exchange of population between all involved levels $\alpha$ and $\alpha'$ mediated through all possible electric-dipole transitions,

$$\begin{aligned} &A_{\alpha'\alpha}, \\ &B_{\alpha'\alpha} W(\omega_{\alpha\alpha'}, T_{\mathrm{BBR}}), \\ &B_{\alpha\alpha'} W(\omega_{\alpha\alpha'}, T_{\mathrm{BBR}}), \end{aligned}$$

which correspond to spontaneous emission, stimulated emission and absorption by BBR, respectively. $W(\omega, T_{\mathrm{BBR}})$ is the energy density for BBR at frequency $\omega$ and temperature $T_{\mathrm{BBR}}$ and can be expressed as

$$W(\omega, T_{\mathrm{BBR}}) = \frac{\hbar\omega^3}{\pi^2 c^3} \left( \mathrm{e}^{\frac{\hbar\omega}{k_B T_{\mathrm{BBR}}}} - 1 \right)^{-1}, \tag{5.3}$$

where $\hbar$ and $k_B$ are the reduced Planck constant and Boltzmann constant, respectively. We will assume $T_{\mathrm{BBR}} = 300$ K unless noted otherwise.

In the following section, we briefly describe the steps involved in the calculation of the $(v, L) : (0, 3) \to (4, 2)$ spectrum in HD$^+$.

## 5.3 Calculation of the $(v, L) : (0, 3) \to (4, 2)$ spectrum

The internal degrees of freedom of the HD$^+$ molecule (rotations and vibrations) have frequencies greater than 1 THz while the external degrees of freedom have frequencies less than 1 MHz. Hence, laser cooling the external degrees of freedom of the molecule effectively does not affect the internal degrees of freedom. However, the molecular rotation interacts relatively strongly with the ambient BBR field, leading to a thermal distribution of rotational-state population corresponding to 300 K [141].

Since the molecules which have made the transition are efficiently dissociated, the probability of them decaying spontaneously to lower levels is negligible [33]. Hence, for the BBR interaction, only the $v = 0$ manifold is considered. The $A_{\alpha\alpha'}$, $B_{\alpha\alpha'}$ and $B_{\alpha'\alpha}$ coefficients between lower and upper levels $\alpha$ and $\alpha'$ are calculated using the radial dipole matrix elements obtained in Ref. [145]. The hyperfine linestrengths are calculated following the approach of Refs. [139,144], and the corresponding Einstein rate coefficients are given in Ref. [87]. A more detailed account of the lineshape model of Biesheuvel *et al.* can be found in ref [86]. Inserting these coefficients in Eq. 5.1 allows quantifying the saturation and the Doppler broadening effects. To obtain highly accurate lineshapes it is in principle also required to take into account other systematic effects, such as possible non-thermal velocity distributions of the HD$^+$ ions, Zeeman splitting, and various line shifts, one of the most significant causes being the AC Stark effect [33]. However, such effects are marginal compared to the effects of Doppler broadening, REMPD and BBR, and for the purpose of the study in this article only the REMPD and the BBR interactions with a thermal ensemble of HD$^+$ are considered.

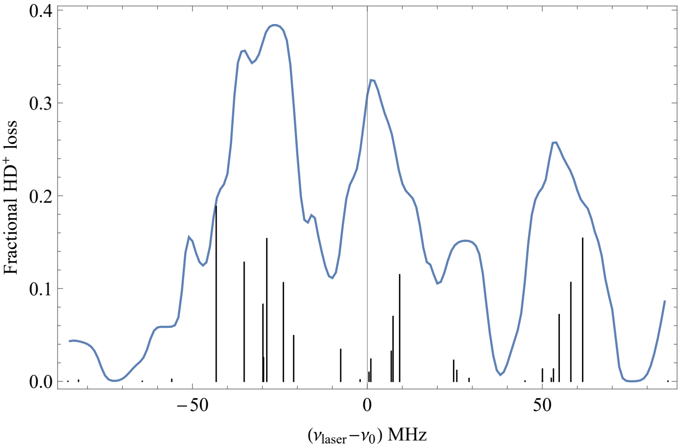

**Figure 5.2:** Doppler-broadened REMPD spectrum of the $(v, L) : (0, 3) \rightarrow (4, 2)$ transition for an ion temperature of 5 mK, laser power of 5 mW focussed in a waist of 100 $\mu$m, and a REMPD duration of 10 s (unless mentioned otherwise, these parameters are used for all figures). $\nu - \nu_0$ denotes the frequency of the probe laser with respect to the spin-averaged ro-vibrational transition frequency $\nu_0$. The positions and relative strengths (in arbitrary units) of the underlying hyperfine components are indicated by the black sticks, which in some cases are barely visible (for example the one at $-64.3$ MHz). Ghost features can be seen at $\nu - \nu_0 = -61$ MHz, $-51$ MHz, and $-15$ MHz. There are other such features in the spectrum, but these are not visible clearly as they are encapsulated by the broader Doppler profile.

Assuming a probe duration of 10 s, the rate equations are solved using the algorithm `NDSolve` of *Mathematica*, resulting into simulated spectra as plotted in Fig. 5.2. In Fig. 5.2, at frequencies of $\nu - \nu_0 = -61$ MHz, $-51$ MHz and $-15$ MHz, relatively narrow peaks can be seen which do not correspond to any hyperfine component. Such ghost features turn out to be a common phenomenon in the simulated spectra, and we describe their origin and characteristics in more detail in the following section.

## 5.4 Ghost features in $(v, L) : (0, 3) \to (4, 2)$ single-photon spectrum

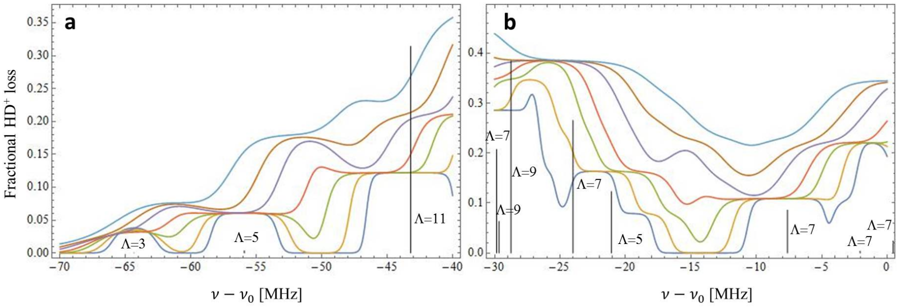

**Figure 5.3:** REMPD signal plotted against frequency $\nu - \nu_0$ for different translational temperatures of the HD$^+$ ions. The hyperfine components are indicated by black sticks. From top to bottom, the curves correspond to ion temperatures 10 mK, 7 mK, 5 mK, 3 mK, 2 mK, 1 mK and 0.5 mK, respectively. Ghost features appear for increasing temperatures near −50 MHz and −61 MHz (a), and near −15 MHz (b).

Figure 5.3a zooms in on the spectrum of Fig. 5.2 in the frequency range (−70 MHz, −40 MHz). If the temperature of the ions is comparatively low (0.5 to 2 mK) such that the Doppler-broadened profiles of individual hyperfine components do not significantly overlap, only 'true' hyperfine lines are visible, while ghost features are completely absent. Note that in our simulations the individual hyperfine lines are heavily saturated near their line centers, as evidenced by the flattened lineshapes. While each hyperfine component has it own transition strength (the relative transition strength is indicated by the size of the stick in the hyperfine stick spectrum of Figs. 5.2 and 5.3), the clipping due to saturation occurs at a signal level which is determined largely by the HD$^+$ population available in the initial hyperfine state. Within the hyperfine manifold of a given ro-vibrational level, this population is essentially equal to the multiplicity, $\Lambda \equiv 2J + 1$, of that hyperfine state. If we now increase the temperature of the ion ensemble to 3 mK, the tails of the Doppler-broadened profiles of adjacent hyperfine components start to overlap, leading to additional signal in the region in between the adjacent hyperfine components. In this region, the laser addresses both adjacent hyperfine states simultaneously, and for sufficiently high saturation levels, the signal can rise *above* the saturation levels of the individual hyperfine lines, thus giving rise to ghost features (Fig. 5.4). The strength of these peaks is proportional to the sum of the lower-state multiplicities of the hyperfine lines between which they show up. This is explained qualitatively in Fig. 5.4. Since these features are not necessarily saturated themselves, they may appear narrow as compared to the saturated, flattened hyperfine lines themselves. If not properly recognized, such ghost features may therefore falsely be identified as 'true' hyperfine lines. The qualitative picture of Fig. 5.4b ascribes the appearance of ghost features to a combination of saturation and partial overlap of Doppler-broadened lines. However, our rate equation model also includes redistribution of population by BBR over various rotational states within the $v = 0$ manifold. To assess the effect of BBR on ghost features, we have reproduced Fig. 5.3a for a BBR temperature of 5 K while leaving all other parameters unchanged; see Fig. 5.5a. At 5 K BBR temperature, only the $(v = 0, L = 0)$ rotational state of HD$^+$ is populated, thereby effectively suppressing the redistribution of population to the $v = 0, L = 3$ lower state of the transition. Note that to produce a REMPD signal at 5 K, an appreciable initial population in $v = 0, L = 3$ is required. Therefore we have calculated the spectra of Fig. 5.5a assuming all population initially being in $v = 0, L = 3$. Figure 5.5a reveals that ghost features appear also in the absence of population redistribution by BBR, and the overall shape of the spectra resembles that of the spectra at $T_{\mathrm{BBR}} = 300$ K of Fig. 5.3a. Also the intensity

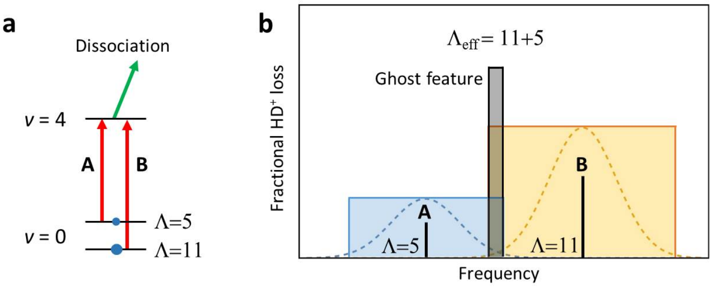

**Figure 5.4:** Qualitative explanation of the origin of ghost features in saturated spectra consisting of partly overlapping lines. (a) Simplified three-level model of the $v = 0 \rightarrow v = 4$ transition in HD$^+$, characterised by two individual transitions, A and B, with different frequencies, linestrengths and lower-state multiplicities ($\Lambda = 5$ and $\Lambda = 11$, respectively). Excitation through transitions A and B is induced by a first laser, while the upper level is dissociated by a second laser to generate a signal (in the form of loss of HD$^+$). The dashed curves in the main plot indicate the Doppler-broadened response function $D_z$ for each line (Eq. 5.2). Clipping due to saturation is here exaggerated for clarity, and occurs at a signal level proportional to the multiplicity of the lower states addressed by the spectroscopy and dissociation lasers. In the region where the two clipped lineshapes overlap, the REMPD lasers address a larger population of HD$^+$ (proportional to the 'effective' multiplicity $\Lambda_{\mathrm{eff}}$), leading to enhanced signals and seemingly narrow ghost features.

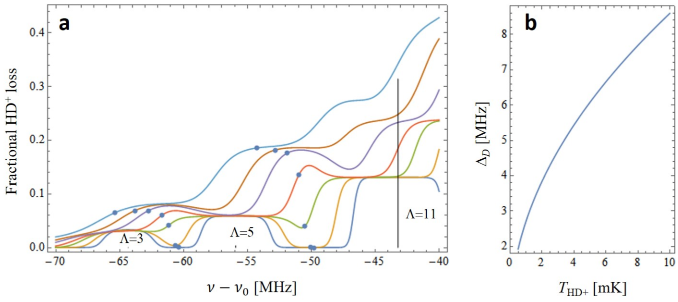

**Figure 5.5:** (a) REMPD signal plotted against $\nu - \nu_0$ for HD$^+$ ion temperatures (from top to bottom) of 10 mK, 7 mK, 5 mK, 3 mK, 2 mK, 1 mK and 0.5 mK, respectively. The curves are obtained for a BBR temperature of 5 K, which effectively suppresses the population redistribution between rotational states in $v = 0$ vibrational level. For each ion temperature, the data points indicate the values of $\nu_X$ computed for two pairs of hyperfine transitions, namely those involving the transitions at −64.3 MHz and −55.9 MHz, and the transitions at −55.9 MHz and −43.2 MHz. Ghost features occur for HD$^+$ temperatures in excess of 2 mK, and shift as the Doppler width increases. (b) Doppler width $\Delta_D$ of the $(v, L) : (0, 3) \rightarrow (4, 2)$ transition at 1442 nm in HD$^+$ in the temperature range considered here.

of the probe laser has some effect on the strength and position of the ghost features. In Fig. 5.6, the signal is plotted for different probe laser intensities. It can be seen that at relatively low laser intensity (100 $\mu$W in a 100 $\mu$m beam waist), the peaks are weak. If the laser power is increased to $\geq 1$ mW so as to dissociate the excited molecules more efficiently (and thereby induce more saturation), the ghost features not only increase in strength but may also shift spectrally (towards more negative frequency in Fig. 5.6a). As the laser intensity is increased further, the shifting of these features becomes smaller. Figure 5.6a also illustrates that random laser intensity variations may translate to additional signal noise with a spread that is enhanced at the location of a ghost feature, and reduced in between the ghost feature and a true hyperfine line (for example near −46.5 MHz in Fig. 5.6a). Another parameter that may affect the ghost features is the time for which the transition is probed. The longer the transitions are probed and the individual transitions get saturated, the more prominent these features become (Fig. 5.7), until the duration becomes long enough to nearly deplete the entire initial population and spectral flattening occurs (Fig. 5.7b). This can be attributed to the redistribution of population among rotational levels in the $v = 0$ manifold, which initially replenishes the population of the lower states of the transition (thereby limiting saturation), but on longer timescales leads to depletion of the sample of HD$^+$ ions and,

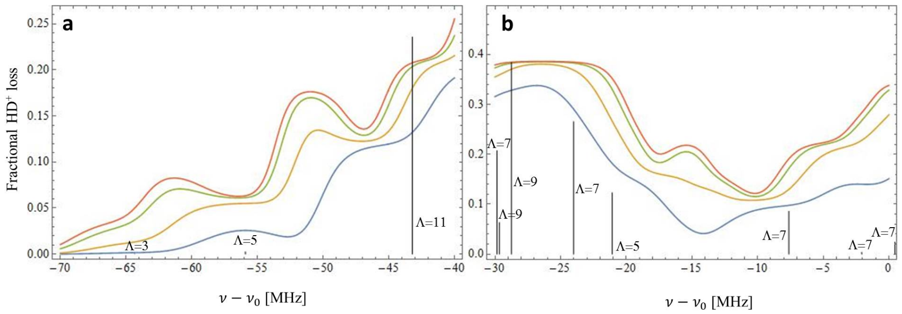

**Figure 5.6:** (a,b) REMPD signal plotted against $\nu - \nu_0$ for different laser intensities and an ion temperature of 5 mK. From top to bottom, plots correspond to laser powers of 10 mW, 5 mW, 1 mW and 100 $\mu$W, respectively, focused in a 100 $\mu$m Gaussian beam waist. The hyperfine components are indicated by black sticks. The position of one of the ghost features in (a) appears to shift from $-48$ MHz at 100 $\mu$W to $-51$ MHz at 10 mW. The hyperfine line at $-55.9$ MHz undergoes an even larger apparent shift: if the power increases from 100 $\mu$W to 10 mW, the peak moves from $-55.9$ MHz to $-62$ MHz, meanwhile transforming from a true hyperfine feature into a ghost feature. Also in (b), a ghost feature near $-15$ MHz becomes visible as the laser intensity is increased.

thus, to enhanced saturation. Below we will show that for spectroscopy of molecular ions with a permanent electric dipole moment (such as HD$^+$), the appearance of ghost features is under certain conditions not determined by the probe duration, but by the lifetime of the initial state under the influence of BBR-driven rotational transitions and spontaneous decay. The ghost features reported here bear some resemblance with the cross-over features seen in saturated absorption spectroscopy. However, the origin and nature of these ghost features are completely different. Ghost peaks arise from interaction with a single photon only, whereas cross-over features in saturated absorption spectroscopy involve two counter-propagating photons. Also, unlike the cross-over resonances in saturated absorption scheme, the ghost features reported here do not lie exactly halfway between two transitions. Moreover, their positions depend on probe laser intensity, saturation, and the temperature of the HD$^+$ ions. In the remainder of this Section, we explain the frequency shift of ghost features with changes in the HD$^+$ temperature and Doppler width, and we quantify the conditions under which ghost features may occur.
Let us consider two hyperfine transitions with center frequencies $\nu_1$ and $\nu_2$, coupling lower hyperfine levels $1, 2$ to excited states $1', 2'$ respectively. We assume that neither transitions from state 1 to state $2'$ nor from 2 to $1'$ are allowed, and that there are no other transitions nearby. In this case we can denote the

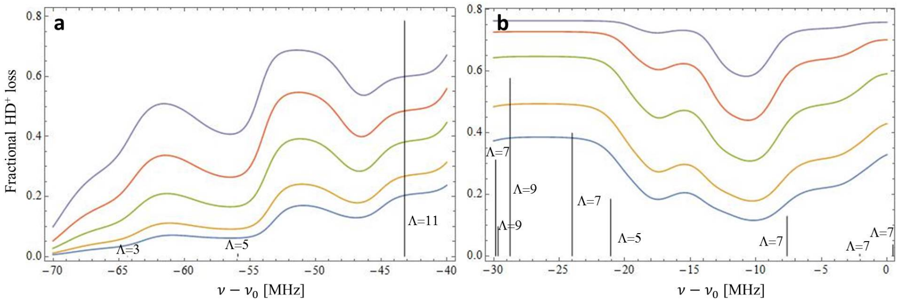

**Figure 5.7:** REMPD signal plotted against $\nu - \nu_0$ for different probe times, 5 mK ion temperature and 5 mW laser power focused in a 100 $\mu$m waist. From top to bottom, plots correspond to 200 s, 100 s, 50 s, 20 s and 10 s probe times, respectively. Ghost features at −51 MHz and −62 MHz in (a) and −15 MHz in (b) become more prominent for longer probe durations, until the duration becomes long enough to nearly deplete the entire initial population, and spectral flattening occurs.

corresponding absorption rate coefficients by $B_1$ and $B_2$. If we consider only levels 1 and 2 and ignore interaction with BBR, then it follows from Eqs. 5.1 and 5.2 that the interaction of the probe laser (having frequency $\nu$) with the two lines leads to a REMPD rate proportional to

$$-\sum_{i=1}^{2} \Lambda_i B_i D_z \left(2\pi(\nu - \nu_i), T_{\mathrm{HD}^+}\right) \frac{I_{\mathrm{probe}}}{c}. \tag{5.4}$$

As before, we assume that any excited-state population is dissociated with unit probability. We can study the appearance and behavior of ghost features in between these two hyperfine components by considering the saturation levels near the point where the two lineshapes in Eq. 5.4 intersect as follows. The two terms in Eq. 5.4 correspond to Gaussian lineshape functions centered at $\nu_1$ and $\nu_2$, respectively, both having a full-width-at-half-maximum Doppler width $\Delta_D$, for which the intersection occurs at a frequency $\nu_X$ given by

$$\nu_X = \frac{\nu_1 + \nu_2}{2} - \frac{\Delta_D^2}{8(\nu_1 - \nu_2)\ln 2} \ln \frac{\Lambda_1 B_1}{\Lambda_2 B_2}. \tag{5.5}$$

Note that $\nu_X$, through the Doppler width $\Delta_D = \left(8 \ln 2\, k_B T_{\mathrm{HD}^+}/m\right)^{1/2}/\lambda$, depends on $T_{\mathrm{HD}^+}$ (here $k_B$ is Boltzmann's constant and $\lambda = c/\nu$). We furthermore point out that Eq. 5.5 requires only relative linestrengths. In Fig. 5.5a, we show the positions $\nu_X$ for two pairs of transitions and for various HD$^+$ temperatures. While the peak position of a ghost feature often is displaced slightly from $\nu_X$ (depending on the relative strengths and lower-state multiplicities of the hyperfine transitions involved), it is typically found in the vicinity of $\nu_X$. Equation 5.5 therefore also gives some quantitative insight in the shift of the ghost feature frequency with Doppler width and transition strength.

Knowing the value of $\nu_X$, we can also estimate the conditions under which ghost features may occur. By definition, at $\nu = \nu_X$, the populations in levels 1 and 2 are dissociated at the same rate. Therefore, with $n(t)$ being the sum of the populations in levels 1 and 2, the population in each level $i = 1, 2$ is given by $n(t)\Lambda_i/(\Lambda_1+\Lambda_2)$, and $n(t)$ can be described by as a single exponential decay as follows,

$$n(t) = n(0)\exp\left\{\left(-t\frac{2\Lambda_1}{\Lambda_1+\Lambda_2}B_1 D_z\left(2\pi\left(\nu_X-\nu_1\right), T_{\mathrm{HD}^+}\right)\frac{I_{\mathrm{probe}}}{c}\right)\right\}, \tag{5.6}$$

again emphasising that $\nu_X$ is a function of $T_{\mathrm{HD}^+}$. Replacing $t$ with the total interaction time, $\tau$, reveals whether significant saturation due to depletion occurs (*i.e.* $n(\tau)/n(0) \ll 1$). In the absence of spontaneous decay of the initial state or interaction with BBR, $\tau$ is simply the total probe duration. However, in the case of molecular ions with a permanent electric dipole moment (such as HD$^+$), the value of $\tau$ also depends on the lifetime of the initial state under the influence of BBR-induced rotational transitions and spontaneous decay. The above example of an ensemble of HD$^+$, initially being prepared in the $(v = 0, L = 3)$ rotational state and interacting with 5 K BBR and the REMPD lasers, is illustrative in this respect. In this case, the initial $(v = 0, L = 3)$ state has a spontaneous lifetime of 4.4 s, which is considerably shorter than the 10 s probe duration used in most calculations in this work. Let us consider the hyperfine transitions located at $\nu - \nu_0 = -55.9$ MHz and $\nu - \nu_0 = -43.2$ MHz in Fig. 5.5a (which we label 1 and 2, respectively), having absorption rate coefficients $B_1 = 6.4 \times 10^{11}$ m$^3$(rad/s)/(J s) and $B_2 = 2.5 \times 10^{13}$ m$^3$(rad/s)/(J s), and multiplicities $\Lambda_1 = 5$ and $\Lambda_2 = 11$. Inserting these values into Eq. 5.5 and combining the result with Eq. 5.6, we find for $\tau = 4.4$ s that $n(\tau)/n(0) \approx 1$ for $T_{\mathrm{HD}^+} < 1.3$ mK (*i.e.* no saturation and therefore no ghost features), while $n(\tau)/n(0) \approx 0$ for $T_{\mathrm{HD}^+} > 2.3$ mK, indicating strong saturation so that ghost features may be expected (see also Fig. 5.9). These findings, obtained from the relatively simple Eqs. 5.5 and 5.6, is in agreement with the curves shown in Fig. 5.5a obtained from the full model. We also find that for intermediate values, $0.05 \lesssim n(\tau)/n(0) \lesssim 0.95$, individual hyperfine components start to overlap significantly, but ghost features typically remain absent. To provide more insight into the role of spontaneous decay and BBR-induced rotational transitions involving the $(v = 0, L = 3)$ initial state in relation to Eq. 5.6, we have plotted the same part of the spectrum, for various probe times, for four different scenarios in Fig. 5.8. A relatively low HD$^+$ temperature of 1.5 mK is used for all four scenarios. In Fig. 5.8a, we fully disable spontaneous decay and BBR by removing the term $M_{\mathrm{BBR}} \cdot \rho(t)$ from

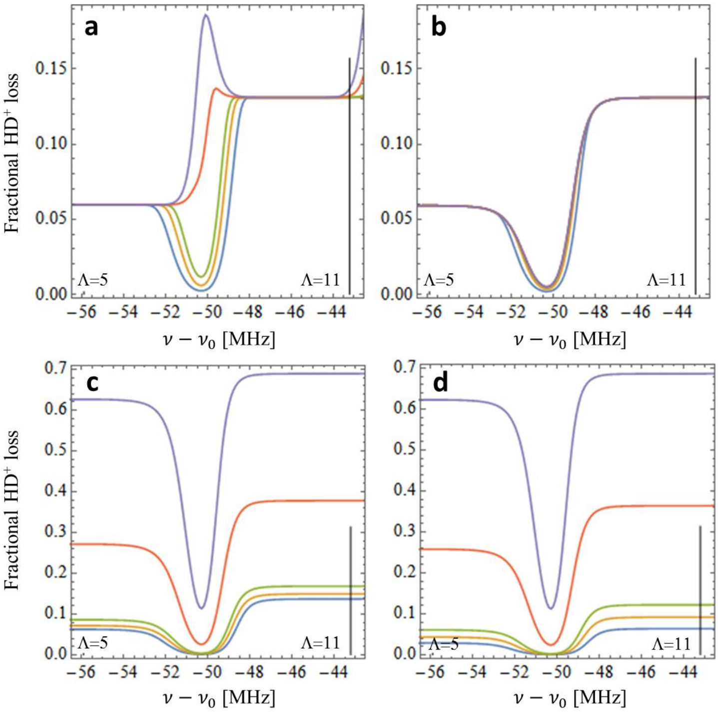

**Figure 5.8:** REMPD signal plotted against $\nu - \nu_0$ at 5 mK ion temperature and 5 mW laser power focussed in a 100 $\mu$m waist, for varying probe time (from top to bottom, 500 s, 100 s, 10 s, 5 s, and 2 s, respectively) and for four different scenarios. (a) Initial population in $(v = 0, L = 3)$ only. No spontaneous decay of the initial state and no interaction with BBR included. (b) Initial population in $(v = 0, L = 3)$ only. Spontaneous decay from $(v = 0, L = 3)$ to $(v = 0, L = 2)$ allowed, but population redistribution by BBR is not included. (c) Initial population in $(v = 0, L = 3)$ only. Spontaneous decay and interaction with 300-K BBR are included. (d) Initial population corresponding to a thermal distribution at 300 K (covering $(v = 0, L =$ 0-5)), and spontaneous decay and interaction with 300 K BBR are included.

Eq. 5.1. As a consequence, $\tau$ is determined entirely by the probe duration. We note that this scenario is similar to laser spectroscopy of trapped molecular ions without a permanent electric dipole moment, such as $H_2^+$ or $N_2^+$. For shorter probe times the two hyperfine components at −55.9 MHz and −43.2 MHz are resolved, but for longer probe durations ($\geq$ 100 s) a ghost feature appears. This is fully in line with Eq. 5.6, which predicts that ghost features appear at 1.5 mK for probe times of 100 s and longer (see Fig. 5.9). This situation changes drastically when spontaneous emission from the $(v = 0, L = 3)$ initial state to $(v = 0, L = 2)$ is introduced, as shown in Fig. 5.8b. In this case, the interaction time $\tau$ is effectively limited to the 4.4 s lifetime of the $(v = 0, L = 3)$ state, and probing for 10 s or longer does not change the spectrum. In Fig. 5.8c we again solve the rate equations starting from an initial population in $(v = 0, L = 3)$ only (as was also done for Figs. 5.8a and b), but now the $HD^+$ ensemble is allowed to fully interact with the 300 K BBR and to undergo spontaneous emission. In this scenario, spontaneous emission initially leads to depletion of $(v = 0, L = 3)$, but this is counteracted by BBR-induced transitions back from $(v = 0, L = 2)$ to $(v = 0, L = 3)$. This population redistribution occurs independently of the frequency $\nu$ of the probe laser, and therefore it merely leads to an overall vertical scaling of the spectral signal towards higher signal levels (and not to the formation of ghost features). A similar vertical scaling is visible in Fig. 5.7. This behaviour suggests that for $\tau$ in Eq.5.6 we must use the typical timescale at which BBR-induced depletion and population redistribution occurs, if the goal is to predict whether ghost features appear or not. This timescale can be computed by summing all the depopulation rates (BBR-induced and spontaneous) from the $(v = 0, L = 3)$ level and taking the inverse, yielding $\tau = 0.96$ s at 300 K. Figure 5.8d is similar to Fig. 5.8c, with the only difference being that here the initial rotational distribution corresponds to a thermal distribution at 300 K, so that also states with $(v = 0, L = 0, 1, 2, 4, 5)$ are populated significantly. As a consequence, the redistribution to $(v = 0, L = 3)$ takes longer, which manifests itself as a smaller overall increase of the signal with increasing probe time. Nevertheless, in both scenarios of Fig. 5.8c and d, the signals at long probe times (500 s and longer) saturate at nearly the same level. Also for the conditions used to obtain Fig. 5.8d, we must use $\tau = 0.96$ s, and in Fig. 5.9 we plot $n(\tau = 0.96\text{ s})/n(0)$, predicting well resolved lines for $T_{\mathrm{HD}^+} < 1.5$ mK, and ghost features for $T_{\mathrm{HD}^+} > 2.8$ mK, in good agreement with the curves of Fig. 5.3 and Fig. 5.8d.

## 5.5 Significance of ghost features for spectroscopy of trapped ions

Obviously, the ghost features reported here may lead to false line identifications if the observed spectra are not analysed with an adequate lineshape model. We emphasise that this phenomenon is not limited to trapped molecular ions: in principle any system, atomic or molecular, with partly overlapping hyperfine or fine structure may exhibit ghost features in the case of strong saturation and resulting depletion of the sample. The possible influence of ghost features should also be observed in two-photon spectroscopic schemes such as that proposed

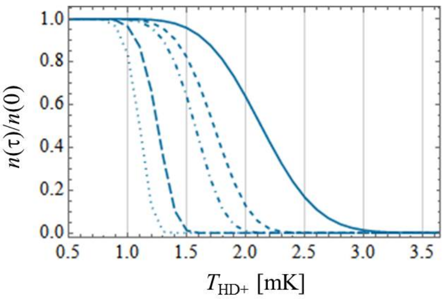

**Figure 5.9:** Value of $n(\tau)/n(0)$ versus $T_{\mathrm{HD}^+}$ as given by Eq. (5.6), for $\tau = 0.96$ s (solid curve), $\tau = 4.4$ s (dashed curve), $\tau = 10$ s (dot-dashed curve), $\tau = 100$ s (long-dashed curved), and $\tau = 500$ s (dotted curve). A value of $n(\tau)/n(0) \approx 1$ implies that individual hyperfine components are well resolved and ghost features are absent, while $n(\tau)/n(0) \approx 0$ indicates that ghost features may be expected to occur. Intermediate values ($0.05 \lesssim n(\tau)/n(0) \lesssim 0.95$) typically imply that hyperfine components start to overlap significantly, while ghost features remain absent.

by Tran *et al.* [87], which involves quasi-degenerate photons inducing near-resonant transitions between $(v, L) : (0, 3) \rightarrow (4, 2)$ and $(v, L) : (4, 2) \rightarrow (9, 3)$. As pointed out by Tran *et al.*, the REMPD signal in this case will consist of a Doppler-free two-photon contribution on top of a Doppler-broadened background. To suppress the latter, it is important to tune the first laser in the wing of the single-photon $(v, L) : (0, 3) \rightarrow (4, 2)$ spectrum, more than one Doppler width away from each hyperfine component [87]. Turning now to Fig. 5.3a, we note that the hyperfine sticks at −56 MHz and −43 MHz are 13 MHz apart, which is more than twice the 6 MHz Doppler width at 5 mK. One might therefore naively guess that the Doppler-broadened signal should be suppressed near −49.5 MHz, and that this might be a suitable frequency for the first laser in the two-photon spectroscopy to be tuned to. However, at 5 mK this region of the spectrum exhibits an *enhanced* Doppler-broadened signal in the form of a ghost feature. In Ref. [58] we identified suitable positions in the $(v, L) : (0, 3) \rightarrow (4, 2)$ spectrum for the two-photon spectroscopy envisaged by Tran *et al.* [87].

## 5.6 Summary and conclusion

In this article, we have used the rate equation model developed by Biesheuvel *et al.* in Ref. [33] to study the $(v, L) : (0, 3) \rightarrow (4, 2)$ single-photon transition in a finite-sized sample of HD$^+$ molecular ions. We analyse and explain, for the first time to our knowledge, the appearance of ghost features in the Doppler-broadened hyperfine structure of the above transition. Our analysis reveals a dependence of ghost feature prominence and position on the Doppler width, relative transition strengths, and saturation levels, and we quantify the conditions under which ghost features may appear, as well as their frequency dependence on Doppler width and relative linestrengths. We find that ghost features may manifest themselves in ro-vibrational spectra of molecular ions with and without a permanent electric dipole moment (which exhibit interaction and no interaction with BBR, respectively), albeit under different conditions. We conclude that knowledge of these spectral features is important for assigning lines in any precision spectroscopy of finite-sized samples of atoms in which a significant fraction of the sample becomes depleted, and where the values of the transition frequencies are not known accurately enough *a priori*, or the samples not cold enough to rule out overlap of the Doppler-broadened line-profiles of adjacent transitions. Our conclusion not only pertains to composite lineshapes in vibrational spectroscopy of cold trapped ions in the optical domain, but to any Doppler-broadened and strongly saturated spectroscopy of finite samples of trapped particles, including laser-induced transitions between atomic or molecular electronic states, and rotational spectroscopy of molecular ions at THz frequencies. We also point out that our results may be extended with no restrictions to other (higher) temperature domains. This highlights the general importance of a rate-equation model to properly understand and interpret the data obtained from precision spectroscopy with finite-sized samples having a rich structure with overlapping line profiles.

Chapter 6

# Proton-electron mass ratio from HD$^+$ revisited

This Chapter has been published earlier in Ref. [60] and is reproduced here only with minor typesetting modifications.

## 6.1 Introduction

Hydrogen molecular ions, on account of their simple three-body structure, are the simplest molecules in nature. Because of this, they are benchmark systems for testing molecular theory. *Ab initio* calculations of the ro-vibrational transition frequencies in the ground electronic state of these molecules can be done with very high accuracy. Recently, the fundamental ro-vibrational transition frequencies of $H_2^+$ and HD$^+$ were calculated with relative uncertainties of about $8 \times 10^{-12}$ [47]. These calculations include relativistic, radiative (QED) and nuclear finite-size corrections to the non-relativistic energies of the ro-vibrational levels. An experiment performed with similar or better accuracy than the theoretical predictions would not only allow a stringent test of the calculations, but also of the theoretical framework within which the calculations were done. Moreover, as suggested by Wing *et al.* more than four decades ago, such an experiment might lead to an improved determination of several fundamental constants, in particular the proton-electron mass ratio, $\mu_{\mathrm{pe}}$ [32]. On the experimental front, with the advances in charged particle trapping combined with laser-cooling techniques and high-resolution laser spectroscopy, progress has been made towards achieving an accuracy comparable to (and ultimately better than) the theoretical predictions. In 2007, the $(v, L) : (0, 2) \rightarrow (4, 3)$ overtone in HD$^+$ was measured with a relative frequency uncertainty of 2 parts-per-billion (ppb) [84]. In 2012, the fundamental transition $(v, L) : (0, 0) \rightarrow (1, 1)$ in HD$^+$ was measured with a relative uncertainty of 1.1 ppb [85]. In this case, the experimentally determined spin-averaged ro-vibrational transition frequency was found to be offset from the more accurate theoretical prediction by $2.5\sigma$. More recently, a measurement of the $(v, L) : (0, 2) \rightarrow (8, 3)$ transition in the same molecule with 1.1 ppb relative uncertainty agreed with the theoretical predictions within the combined experimental and theoretical uncertainty [33, 86]. Because of the agreement between the theoretical prediction and the experimental determination, the authors could for the first time extract the value of $\mu_{\mathrm{pe}}$ as a single parameter with a relative uncertainty of 2.9 ppb [33].

In this article, we revisit the determination of $\mu_{\mathrm{pe}}$ from HD$^+$ taking into account all existing measurements of ro-vibrational transitions in HD$^+$, similar as done by Karshenboim and Ivanov [146]. Since the publication of Ref. [33, 86, 146], theoretical calculations were improved by including previously unaccounted higher-order QED correction terms [47]. The improvement in theoretical calculations by itself forms a reason to re-enumerate its agreement with the previously measured transitions. Also, since the improved calculations were performed using newly published CODATA-14 recommended values of the fundamental constants, in this article we present a consistent determination of $\mu_{\mathrm{pe}}$ from HD$^+$. As we will explain further below, the strongly improved value of the new CODATA-14 value of the electron mass (in atomic mass units) makes it more appropriate to include it as input data instead of the proton mass value, which affects the sensitivity coefficients used in previous determinations of $\mu_{\mathrm{pe}}$ from HD$^+$. We subsequently present a revised value of $\mu_{\mathrm{pe}}$ here.

This article is structured as follows: In Section 6.2, we briefly review the recent improvements in the theoretical calculation of ro-vibrational transitions in the ground electronic state of HD$^+$, followed by a comparison between the existing measurements with the improved theory in Section 6.3. In Section 6.4, we determine the proton-to-electron mass ratio $\mu_{\mathrm{pe}}$ from the measurements considered in Section 6.3. In Section 6.5, we discuss the prospects of an improved determination of $\mu_{\mathrm{pe}}$ from Doppler-free two-photon spectroscopy of HD$^+$ and H$_2^+$.

## 6.2 Improvement in theory

The energy of a ro-vibrational level of HD$^+$, calculated in the framework of QED, may be written as

$$E = R_\infty hc \left[ E_{\mathrm{nr}}(\mu_{\mathrm{pe}}, \mu_{\mathrm{de}}) + \alpha^2 F_{\mathrm{QED}}(\alpha) + A_{\mathrm{p}}^{\mathrm{fs}} \left( \frac{r_{\mathrm{p}}}{a_0} \right)^2 + A_{\mathrm{d}}^{\mathrm{fs}} \left( \frac{r_{\mathrm{d}}}{a_0} \right)^2 \right] \tag{6.1}$$

where $R_\infty$ and $\alpha$ are the Rydberg and fine-structure constant respectively, and $a_0 = \alpha/4\pi R_\infty$ is the Bohr radius. The main contribution to $E$ is the non-relativistic (Schrödinger) energy $E_{\rm nr}$, which depends on the proton-electron ($\mu_{\rm pe}$) and deuteron-electron ($\mu_{\rm de}$) mass ratios. The next term corresponds to the relativistic and QED corrections. The function $F_{\rm QED}(\alpha)$ is a non-analytic expansion which, beyond powers of $\alpha$, also contains logarithmic terms like $\alpha^p \ln^q(\alpha)$. The last two terms are the leading-order nuclear finite-size corrections, with $r_{\rm p}$ and $r_{\rm d}$ respectively standing for the proton and deuteron charge radii. The coefficients $A^{\rm fs}_{\rm p,d}$ are proportional to the squared density of the wave function at the electron-nucleus coalescence point. Higher-order nuclear size and structure corrections are negligible at the current level of theoretical accuracy.

The non-relativistic energy $E_{\rm nr}$ and its dependence on the mass ratios can be calculated with very high accuracy by numerical solution of the Schrödinger equation for the exact three-body Coulomb Hamiltonian using a variational method (see e.g. [88–91]). The theoretical accuracy of the energy levels $E$ has been steadily improved over the last decade through a systematic evaluation, in ascending powers of $\alpha$, of the QED contributions appearing in $F_{\rm QED}(\alpha)$ in the framework of non-relativistic QED (NRQED). The main steps of this work have been published in the successive papers [47,92–95]. The first step [92] was the calculation of leading relativistic and radiative corrections at the $R_\infty\alpha^2$ and $R_\infty\alpha^3$ orders within an exact three-body approach, with a partial consideration of contributions at the following order ($R_\infty\alpha^4$). This was later pursued [93] by a calculation of relativistic corrections at this order in the framework of the adiabatic approximation. The first high-precision comparisons between theory and experiment involving the ro-vibrational spectrum of HD$^+$ [84,85] were done with the predictions from [92,93].

A few years later, the theory was further refined by the calculation of $R_\infty\alpha^5$-order corrections [94,95] within the adiabatic approach. These results were used in the analysis of the recently measured $(v, L) = (0, 2) \to (8, 3)$ transition [33,86].

However, it has since been realised [49] that the treatment of second-order perturbation terms in the adiabatic approximation as done in these previous works was incomplete. This type of contribution is present in the $R_\infty\alpha^4$-order relativistic correction, and also appears at higher orders like in the $R_\infty\alpha^5$-order one-loop corrections. Since this gives the largest contribution to the difference between earlier works [92–95] and the updated predictions used here [47], it is worth explaining this point in more detail.

The general structure of such terms is

$$\Delta E = \langle\Psi|\, AQ(E_0 - H)^{-1}QB\, |\Psi\rangle + \langle\Psi|\, H^{(n)}\, |\Psi\rangle \tag{6.2}$$

where $A$, $B$ and $H^{(n)}$ are effective operators acting on the electron, $Q$ is a projection operator onto a subspace orthogonal to the non-relativistic wavefunction $\Psi$, $E_0, H$ the non-relativistic energy and Hamiltonian. For example, a term of the type in Eq. 6.2 with $A = B = H_B$, where $H_B$ is the electronic Breit-Pauli Hamiltonian, appears in the $R_\infty\alpha^4$ relativistic correction [93]. Similarly, a term with $A = H_B$ and $B = U_{\rm vp}$ (and an additional factor of 2), where $U_{\rm vp}$ is the electron-nuclei Uehling interaction, appears in the one-loop vacuum polarization at the $R_\infty\alpha^5$ order (see Eq. 4 of [147]). In the adiabatic approximation, the molecular wave function is taken in a form

$$\Psi(\mathbf{r}, R) = \phi_{\rm el}(\mathbf{r}; R)\chi_{\rm ad}(R) \tag{6.3}$$

where $\phi_{\rm el}(\mathbf{r}; R)$ and $\chi_{\rm ad}(R)$ are respectively the electronic and nuclear wave functions. Then Eq. 6.2 can be written as a sum over intermediate states which may be separated into three terms. The first term involves only electronic excitations:

$$\Delta E_{\rm el} = \langle\chi_{\rm ad}|\, \Delta\mathcal{E}_{\rm el}(R)\, |\chi_{\rm ad}\rangle\,, \tag{6.4a}$$

$$\Delta\mathcal{E}_{\rm el}(R) = \langle\phi_{\rm el}|\, AQ_{\rm el}(E_{\rm el} - H_{\rm el})^{-1}Q_{\rm el}B\, |\phi_{\rm el}\rangle + \langle\phi_{\rm el}|\, H^{(n)}\, |\phi_{\rm el}\rangle\,. \tag{6.4b}$$

Here $Q_{\rm el}$ is a projection operator onto a subspace orthogonal to $\phi_{\rm el}$, and $E_{\rm el}, H_{\rm el}$ the electronic energy and Hamiltonian. The second term involves vibrational excitations:

$$\Delta E_{\rm vb} = \langle\chi_{\rm ad}|\, \mathcal{A}(R)Q_{\rm vb}(E_{\rm vb} - H_{\rm vb})^{-1}Q_{\rm vb}\mathcal{B}(R)\, |\chi_{\rm ad}\rangle\,, \tag{6.5}$$

with $\mathcal{A}(R) = \langle\phi_{\rm el}|A|\phi_{\rm el}\rangle$, $\mathcal{B}(R) = \langle\phi_{\rm el}|B|\phi_{\rm el}\rangle$, $Q_{\rm vb}$ is a projection operator onto a subspace orthogonal to $\chi_{\rm ad}$, and $E_{\rm vb}, H_{\rm vb}$ the vibrational energy and Hamiltonian. Finally, the third term is the contribution beyond the adiabatic approximation, involving simultaneous electronic and vibrational excitations. This term is very small and may be neglected at the current level of theoretical accuracy, as has been explicitly verified in the case of the $R_\infty\alpha^5$-order one loop vacuum polarisation contribution [147] by comparing the sum of Eqs. 6.4a and 6.5 to a full calculation of Eq. 6.2 performed in an exact three-body approach.

The vibrational contribution of Eq. 6.5 is the term which had been neglected in previous treatments. Although its value for individual ro-vibrational states is significantly smaller than the respective electronic contribution of Eq. 6.4a (by typically one order of magnitude), its contribution to ro-vibrational transition frequencies is more important because it has a stronger dependence on the ro-vibrational state leading to a much less pronounced cancellation. For example, the vibrational part of the $R_\infty\alpha^4$ relativistic correction contributes to the transition frequencies at a relative level of about $7 \times 10^{-10}$, which is comparable to the experimental uncertainties.

In addition to a systematic evaluation of vibrational terms at the $R_\infty \alpha^4$ and $R_\infty \alpha^5$ orders, the work of Ref. [47] improved the theoretical accuracy further through a partial calculation of the following order $R_\infty \alpha^6$. It has also proved necessary to improve the numerical accuracy of the leading-order relativistic and radiative corrections (especially the Bethe logarithm) [148,149], since their initial evaluation [92] targeted a lower theoretical precision. Updated theoretical predictions for the three most accurately measured transitions in $\mathrm{HD}^+$ are given in Table 6.1. The relative theoretical uncertainty is about $8 \times 10^{-12}$ in all cases.

## 6.3 Comparison between experiment and theory

Experimentally measured spin-averaged frequencies of the different ro-vibrational transitions in $\mathrm{HD}^+$ are tabulated along with their respective experimental uncertainties in Table 6.2, together with the corresponding theoretical transition frequencies. Figure 6.1 graphically shows the level of agreement between the measured transition frequencies and their respective theoretical predictions. Here it should be noted that the error bars represent the combined uncertainty of experiment and theory, given by $\sigma_c = (\sigma_e^2 + \sigma_t^2)^{1/2}$. It can be observed that the $(v, L) : (0, 2) \rightarrow (4, 3)$ measurement (henceforth indicated by the shorthand $v : 0 \rightarrow 4$ , and with similar notations for the other two transitions) has the largest relative (combined) uncertainty of 2.3 ppb, while the offset from the theoretical prediction is 1.7 ppb. The transitions $v : 0 \rightarrow 1$ and $v : 0 \rightarrow 8$ have similar experimental uncertainties of 1.1 ppb. However, the former deviates from theory by 2.7 ppb ($2.5\sigma$). The experiments are described in detail elsewhere [84–86].

| Transition | $(0,0) \rightarrow (1,1)$ | $(0,2) \rightarrow (4,3)$ | $(0,2) \rightarrow (8,3)$ |
|---|---|---|---|
| $\Delta E_{\mathrm{nr}}$ | 58 604 301 246.9 | 214 976 047 255.7 | 383 403 254 198.4 |
| $\Delta E_{\alpha^2}$ | 1 003 551.5 | 3 411 243.9 | 5 470 087.2 |
| $\Delta E_{\alpha^3}$ | −250 978.4 | −891 610.9(3) | −1 536 834.7(5) |
| $\Delta E_{\alpha^4}$ | −1 770.8 | −6 307.9(1) | −10 914.3(1) |
| $\Delta E_{\alpha^5}$ | 110.3 | 352.8(1) | 684.1(2) |
| $\Delta E_{\alpha^6}$ | −2.1(5) | −7.6(17) | −13.7(29) |
| $\Delta E_{\mathrm{tot}}$ | 58 605 052 157.5(5) | 214 978 560 967.8(17) | 383 407 177 208.0(30) |

**Table 6.1:** Theoretical transition frequencies for the three most accurately measured ro-vibrational transitions in HD$^+$ (in kHz). The first line is the non-relativistic transition frequency, and next are QED corrections in ascending powers of $\alpha$. The final result given in the last line is the sum of all the above terms with an additional (very small) muonic vacuum polarisation contribution. Nuclear finite-size corrections have been included in $\Delta E_{\alpha^2}$ for simplicity. The CODATA-14 recommended values of fundamental constants are used. Estimated theoretical uncertainties, when significant, are given between parentheses.

| Transition | $\nu_{\text{theo}}$ [MHz] | $\nu_{\text{exp}}$ [MHz] | $S^{fi}_{\text{pe(de)}}$ |
|---|---|---|---|
| $(v,L):(0,0)\rightarrow(1,1)$ | 58 605 052.1575(5) | 58 605 052.000(64) | −0.32296 |
| $(v,L):(0,2)\rightarrow(4,3)$ | 214 978 560.9678(17) | 214 978 560.6(5) | −0.29190 |
| $(v,L):(0,2)\rightarrow(8,3)$ | 383 407 177.208(3) | 383 407 177.38(41) | −0.24998 |

**Table 6.2:** Comparison of the frequencies of the three most accurately measured ro-vibrational transitions in $HD^+$ with their corresponding theoretical predictions. The second column presents the transition frequencies calculated from first principles, while the third column presents the corresponding measured transition frequencies. The uncertainties are shown in parentheses. The last column gives the values of the sensitivity coefficient to $\mu_{\text{pe}}$, which is defined and discussed in Sec. 6.4.

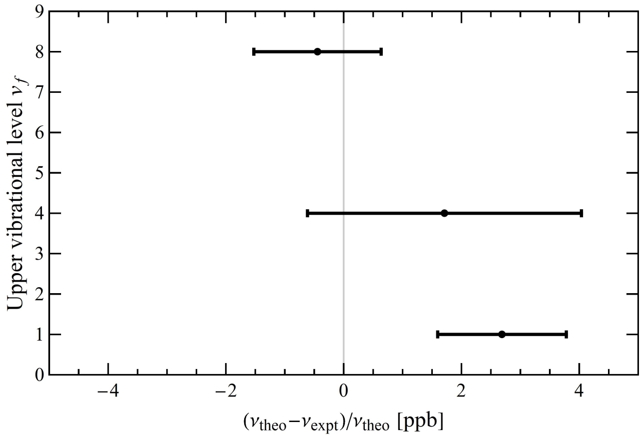

**Figure 6.1:** Relative offsets of the measured frequencies of the three ro-vibrational transitions in HD$^+$ with respect to their respective theoretical predictions. Error bars represent the combined theoretical and experimental uncertainty, $\sigma_c$.

## 6.4 Determination of the proton-electron mass ratio $\mu_{\rm pe}$

From Eq. 6.1 it may be observed that the ro-vibrational transition frequencies in HD$^+$ depend on no less than six fundamental constants: the Rydberg constant $R_\infty$, the fine structure constant $\alpha$, the nuclear radii $r_{\rm p}, r_{\rm d}$ and the nucleus-to-electron mass ratios $\mu_{\rm pe}, \mu_{\rm de}$. However, four of them ($R_\infty$, $\alpha$, $r_{\rm p}$ and $r_{\rm d}$) have been determined by other experiments with an accuracy that is several order of magnitude higher than could be obtained from HD$^+$ spectroscopy experiments performed so far. We thus fix their values as equal to the CODATA recommended ones and focus on determination of nucleus-to-electron mass ratios.

It may seem that the three measurements compiled in Table 6.2 are sufficient to simultaneously constrain the two independent parameters $\mu_{\rm pe}$ and $\mu_{\rm de}$. However, it is important to realise that all the HD$^+$ ro-vibrational spacings essentially depend on the ratio $\mu_{\rm re}$ of the nuclear reduced mass $m_{\rm r} = m_{\rm p}m_{\rm d}/(m_{\rm p}+m_{\rm d})$ to the electron mass. Consequently, measurements in HD$^+$ only allow determining $\mu_{\rm re}$, but not $\mu_{\rm pe}$ and $\mu_{\rm de}$ separately (see also the discussion in Ref. [88]). This issue could potentially be solved in the future by combining the HD$^+$ measurements with the measurement of one or several transitions in $H_2^+$, whose frequencies only depend on $\mu_{\rm pe}$ [59]. Here, having only HD$^+$ data at our disposal, we need to set one of the mass ratios to its CODATA value in order to determine another one.

Note that the choice of variables $(\mu_{\mathrm{pe}}, \mu_{\mathrm{de}})$ made in Eq. 6.1 is arbitrary: in principle, we could fix any one of the three mass ratios $(\mu_{\mathrm{pe}}, \mu_{\mathrm{de}}, \mu_{\mathrm{dp}})$. The most relevant choice depends on the current state of knowledge, since we should set the value of the most accurately known mass ratio in order get a new determination of another, less accurately known one. In this regard, an important evolution has occurred in the latest adjustment of fundamental constants (CODATA-14). In the CODATA-10 set of recommended values, the electron mass (in atomic mass units) had a relative uncertainty of $4.0 \times 10^{-10}$, while the relative uncertainties in the values of $m_{\mathrm{p}}$ and $m_{\mathrm{d}}$ were $8.9 \times 10^{-11}$ and $3.8 \times 10^{-11}$ respectively [19]. Thus the most accurately known mass ratio was $\mu_{\mathrm{dp}}$; this has led to fix $\mu_{\mathrm{dp}}$ in previous adjustments of $\mu_{\mathrm{pe}}$. However, with the publication of the CODATA-14 recommended values, the relative uncertainty of $m_{\mathrm{e}}$ was reduced to $2.9 \times 10^{-11}$, while the relative uncertainties in $m_{\mathrm{p}}$ and $m_{\mathrm{d}}$ were reported to be $9.0 \times 10^{-11}$ and $2.0 \times 10^{-11}$ respectively [18]. The most accurately known mass ratio is now $\mu_{\mathrm{de}}$, so that it makes more sense to set it to its CODATA-14 value in adjusting $\mu_{\mathrm{pe}}$. We will follow this new approach in the present work.

For a deeper understanding of the reasons for this choice, it is useful to observe that the CODATA values of the mass ratios are essentially obtained from separate determinations of the particle masses, by mass spectrometry ($m_{\mathrm{p}}$, $m_{\mathrm{d}}$) or $g$-factor measurements ($m_{\mathrm{e}}$). Fixing the value of $\mu_{\mathrm{dp}}$, as done in previous treatments, is equivalent to taking into account the measurements of $m_{\mathrm{d}}$ and $m_{\mathrm{p}}$, while ignoring that of $m_{\mathrm{e}}$. In this case, the value of $\mu_{\mathrm{pe}}$ extracted from HD$^+$ spectroscopy may be interpreted as a cross-check of the electron mass measurement. Here, we will fix $\mu_{\mathrm{de}}$, meaning that we take into account the measurements of $m_{\mathrm{d}}$ and $m_{\mathrm{e}}$, but ignore that of $m_{\mathrm{p}}$. Our subsequent determination of $\mu_{\mathrm{pe}}$ can be seen as a consistency check of the proton mass value, as obtained from mass spectrometry and from molecular spectroscopy. In the present state of knowledge, it is more relevant to cross-check the proton mass than the electron mass since the latter has been determined to higher accuracy.

In order to derive the proton-electron mass ratio from the data of Table 6.2, we need to calculate the dependence of the ro-vibrational transition frequencies on $\mu_{\mathrm{pe}}$. This can be expressed in terms of a normalised sensitivity coefficient, $S^{fi}_{\mathrm{pe}(n)}$, as

$$S^{fi}_{\mathrm{pe}(n)} = \frac{\mu_{\mathrm{pe}}}{\nu_{fi}} \left.\frac{\partial \nu_{fi}}{\partial \mu_{\mathrm{pe}}}\right|_{\mu_n} \tag{6.6}$$

$$= \frac{1}{(E_f - E_i)} \left( \mu_{\mathrm{pe}} \left.\frac{\partial E_f}{\partial \mu_{\mathrm{pe}}}\right|_{\mu_n} - \mu_{\mathrm{pe}} \left.\frac{\partial E_i}{\partial \mu_{\mathrm{pe}}}\right|_{\mu_n} \right). \tag{6.7}$$

Here $\nu_{fi}$ is the frequency of a transition from a lower level $i$ with energy $E_i$ to an upper level $f$ with energy $E_f$, and $\mu_n$ ($n =$ dp or de) denotes the mass ratio that is kept fixed while varying $\mu_{\mathrm{pe}}$.

The main dependence of the energy levels given by Eq. 6.1 on mass ratios arises from the non-relativistic contribution $E_{\mathrm{nr}}$. Although the QED correction terms also depend on the mass ratios, their contribution to the overall dependence can be neglected since they are smaller by a factor of $\alpha^2$. The sensitivity coefficients $S^{fi}_{\mathrm{pe}(n)}$ can thus be obtained with sufficient accuracy from a calculation of nonrelativistic energy levels as done in [88, 89]. These works used the variables $(\mu_{\mathrm{pe}}, \mu_{\mathrm{dp}})$ and provide the coefficients $\mu_{\mathrm{pe}} \left.\frac{\partial E}{\partial \mu_{\mathrm{pe}}}\right|_{\mu_{\mathrm{dp}}}$ for individual ro-vibrational levels, from which the sensitivities $S^{fi}_{\mathrm{pe(dp)}}$ of ro-vibrational transitions were obtained by applying Eq. 6.7 and used in previous determinations of $\mu_{\mathrm{pe}}$ from HD$^+$ [33, 146]. Since in our new approach we fix $\mu_{\mathrm{de}}$, we use a different coefficient, $S^{fi}_{\mathrm{pe(de)}}$. To obtain this coefficient, it is convenient to write the non-relativistic three-body Hamiltonian in terms of $\mu_{\mathrm{pe}}$ and $\mu_{\mathrm{de}}$, following the notations of Eq. (6) in [88]:

$$H_0 = -\frac{1}{2}\left(\mu_{\mathrm{pe}}^{-1} + \mu_{\mathrm{de}}^{-1}\right)\nabla^2_{\mathbf{r_1}} - \frac{1}{2}\left(1 + \mu_{\mathrm{de}}^{-1}\right)\nabla^2_{\mathbf{r_2}} - \mu_{\mathrm{de}}^{-1}\,\nabla_{\mathbf{r_1}}\cdot\nabla_{\mathbf{r_2}} + V_C, \tag{6.8}$$

where $\mathbf{r_1}$ and $\mathbf{r_2}$ are the position vectors of proton and electron with respect to the deuteron, and $V_C$ the Coulomb interaction potential. Using Eqs. 10 of [88] one immediately gets

$$\mu_{\mathrm{pe}} \left.\frac{\partial E}{\partial \mu_{\mathrm{pe}}}\right|_{\mu_{\mathrm{de}}} = \frac{1}{2}\,\mu_{\mathrm{pe}}^{-1}\left\langle \nabla^2_{\mathbf{r_1}} \right\rangle \tag{6.9}$$

The quantity on the LHS of Eq. 6.9 can also be expressed as shown below using the chain rule of differential calculus,

$$\mu_{\mathrm{pe}} \left.\frac{\partial E}{\partial \mu_{\mathrm{pe}}}\right|_{\mu_{\mathrm{de}}} = \mu_{\mathrm{pe}} \left.\frac{\partial E}{\partial \mu_{\mathrm{pe}}}\right|_{\mu_{\mathrm{dp}}} - \mu_{\mathrm{dp}} \left.\frac{\partial E}{\partial \mu_{\mathrm{dp}}}\right|_{\mu_{\mathrm{pe}}} \tag{6.10}$$

The quantities appearing on the RHS of Eq. 6.10 are given in Tables II and III of [88] for a range of ro-vibrational states. We used these values to get the sensitivity coefficients for the $v : 0 \to 1$ and $v : 0 \to 4$ transitions. For the $v : 0 \to 8$ transition we directly determined the sensitivity of the $(v = 8, L = 3)$ level from Eq. 6.9. The values of the sensitivity coefficients for the three transitions can be found in Table 6.2.

As discussed in [88], the underlying dependence of ro-vibrational energies on the ratio $\frac{\mu_{\mathrm{re}}}{m_{\mathrm{e}}}$ results in a fixed ratio between the various sensitivity coefficients for a given level. For example, in Eq. 6.10 the first term is almost exactly three times larger than the second one [88]. This implies that $\left.\frac{\partial E}{\partial \mu_{\mathrm{pe}}}\right|_{\mu_{\mathrm{de}}}$ is about 2/3 times $\left.\frac{\partial E}{\partial \mu_{\mathrm{pe}}}\right|_{\mu_{\mathrm{dp}}}$, and therefore the sensitivities of the transition frequencies used in our approach, $S^{fi}_{\mathrm{pe(de)}}$ are also smaller by a factor of 2/3 with respect to the coefficients used in previous work, $S^{fi}_{\mathrm{pe(dp)}}$. It then follows that the error bar and displacement of the found value of $\mu_{\mathrm{pe}}$ from the CODATA-14 value are about 3/2 times those published by Biesheuvel *et al.* [33] and Karshenboim and Ivanov [146]. As justified above, the value and uncertainty of $\mu_{\mathrm{pe}}$ reported in this work supersede the previously reported values.

From a single transition measurement, a new value of $\mu_{\mathrm{pe}}$ is deduced using the relation

$$\mu_{\mathrm{pe}}(\nu_{fi}) = \mu_{\mathrm{pe},0} + \frac{\mu_{\mathrm{pe},0}}{S^{fi}_{\mathrm{pe(de)}}} \frac{\nu_{fi,\mathrm{exp}} - \nu_{fi,\mathrm{theo}}}{\nu_{fi,\mathrm{theo}}}, \tag{6.11}$$

and if we choose to combine several transition measurements, then the resulting value of $\mu_{\mathrm{pe}}$ is obtained by a standard least-squares adjustment procedure. Before other transitions are included, it is important to consider the two key assumptions that underpin the determination of fundamental constants from the comparison of experiment and theory, as done here for $\mu_{\mathrm{pe}}$. These assumptions are that the theory predicts the observable properties of the system under consideration faithfully, and that the experimental measurement is performed without any uncorrected biases. Consequently, any significant disagreement between theory and experiment (in terms of the combined experimental and statistical uncertainty) indicates that at least one of the two key assumptions is likely not met (depending on a pre-specified minimum required confidence level). Of the three transitions in HD$^+$ considered here, the $v: 0 \to 4$ and $v: 0 \to 8$ measurements agree with theory within one sigma ($\sigma_c$). Of these two transitions, the $v: 0 \to 4$ transition contributes relatively little given its 2.3 ppb uncertainty (to be compared with 1.1 ppb for the $v: 0 \to 8$ transition). The $v: 0 \to 1$ transition has a small combined relative uncertainty of 1.1 ppb, but displays a (hitherto unresolved) discrepancy of $2.5\sigma_c$ (see Fig. 6.1). Depending on the minimum confidence level required (a subject which we will not address here) this transition therefore may or may not be taken into account in the determination of $\mu_{\mathrm{pe}}$. We therefore provide results for both scenarios. In Table 6.3, an overview of the determination of $\mu_{\mathrm{pe}}$ from different combinations of the measurements as well as individual transitions considered is presented. A visual representation of the deviations of $\mu_{\mathrm{pe}}$ extracted from HD$^+$ from the CODATA-14 recommended value is provided in Fig. 6.2.

| Transition | $\mu_{\mathrm{pe}}$ | $\mu_{\mathrm{pe}}$-$\mu_{\mathrm{pe}}$(C14) | $\frac{\delta\mu_{\mathrm{pe}}}{\mu_{\mathrm{pe}}}$ [ppb] | $\frac{\mu_{\mathrm{pe}}-\mu_{\mathrm{pe}}(\mathrm{C14})}{\delta\mu_{\mathrm{pe}}}$ |
|---|---|---|---|---|
| $v: 0 \rightarrow 1$ | 1 836.152 689 2(62) | 0.000 015 | 3.4 | 2.5 |
| $v: 0 \rightarrow 4$ | 1 836.152 684 6(148) | 0.000 011 | 8.0 | 0.74 |
| $v: 0 \rightarrow 8$ | 1 836.152 670 6(79) | −0.000 003 3 | 4.3 | −0.41 |
| $v: 0 \rightarrow 4$ and $v: 0 \rightarrow 8$ | 1 836.152 673 8(70) | −0.000 000 08 | 3.8 | −0.012 |
| All transitions | 1 836.152 682 4(46) | 0.000 008 5 | 2.5 | 1.8 |

**Table 6.3:** Overview of $\mu_{\mathrm{pe}}$ determination from HD$^+$ from the three measurements considered in this article. The second column lists the values of $\mu_{\mathrm{pe}}$ derived from the corresponding transition or combination of transitions, with their uncertainties in parentheses. The third column presents the deviations of the extracted values of $\mu_{\mathrm{pe}}$ from the CODATA-14 recommended value, $\mu_{\mathrm{pe}}$(C14). In the fourth column, the uncertainties of the $\mu_{\mathrm{pe}}$ determinations are written in relative terms. Finally in the fifth column, the deviations of the determined values of $\mu_{\mathrm{pe}}$ from $\mu_{\mathrm{pe}}$(C14) are listed in terms relative to the uncertainty of the determined $\mu_{\mathrm{pe}}$.

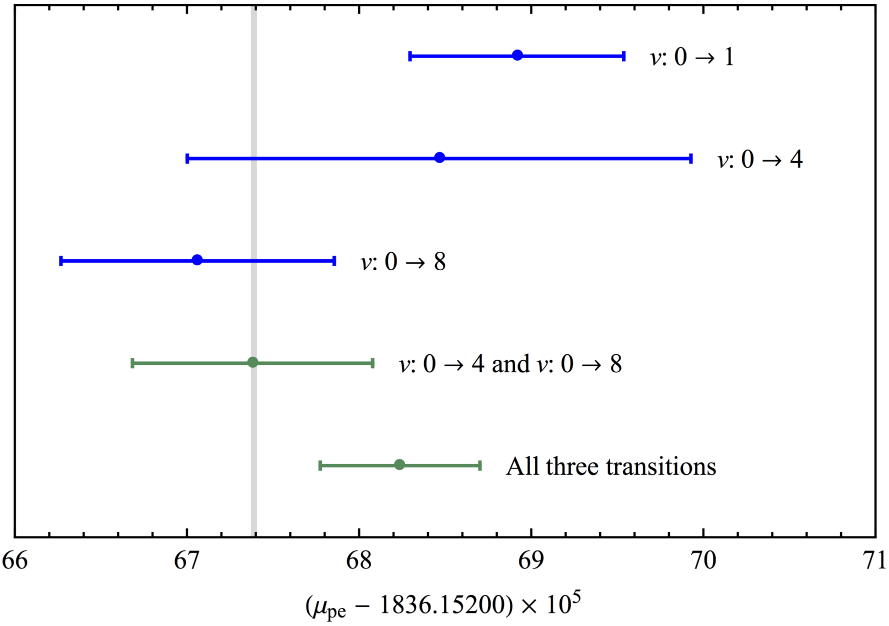

**Figure 6.2:** Visual representation of the results of the various $\mu_{\mathrm{pe}}$ values determined from measurements in $\mathrm{HD}^+$, as compared to the CODATA-14 recommended value $\mu_{\mathrm{pe}}(\mathrm{C14})$ (value and error bar indicated by the position and width of the vertical grey line).

## 6.5 Outlook and conclusion

The uncertainty of $\mu_{\mathrm{pe}}$ determined from the three ro-vibrational transitions of $\mathrm{HD}^+$ considered in this article is still 27 times larger than the CODATA-14 adjustment of the same. However, the prospects for determination of fundamental constants from spectroscopy of hydrogen molecular ions indicate a substantial possible improvement. In $\mathrm{HD}^+$, an experiment towards Doppler-free two-photon spectroscopy of $(v, L) : (0, 3) \to (4, 2) \to (9, 3)$ is underway in Amsterdam [87]. An experimental accuracy better than the theoretical uncertainty of $\sim 1 \times 10^{-11}$ would allow a determination of $\mu_{\mathrm{pe}}$ (or equivalently, of the proton atomic mass $m_{\mathrm{p}}$) with an uncertainty comparable to the CODATA-14 recommended value. Furthermore, $m_{\mathrm{p}}$ has recently been measured with a relative uncertainty of 32 parts-per-trillion (ppt) from Penning trap mass measurements [31]. However, the measured value of $m_{\mathrm{p}}$ is $3\sigma$ off from the CODATA-14 value of $m_{\mathrm{p}}$. In this context, a precise determination of $m_{\mathrm{p}}$ from

HD$^+$ may allow a comparison with the $m_\mathrm{p}$ determination in Ref. [31] and serve as a consistency check for the measurements of the same quantity from different physical systems. A further step would be to combine HD$^+$ and H$_2^+$ spectroscopy at the few-ppt accuracy level in order to constrain not only the $\mu_\mathrm{pe}$ and $\mu_\mathrm{dp}$ mass ratios, but also the Rydberg constant $R_\infty$ and the nuclear radii $r_\mathrm{p}, r_\mathrm{d}$, thus shedding light on the curent discrepancies between different determinations of these constants, coloquially known as the proton-radius puzzle [59].

In conclusion, in this article we have revisited the determination of $\mu_\mathrm{pe}$ from HD$^+$ as done in Refs. [33, 146] in light of improved theoretical calculations and updated CODATA-14 recommended values of the fundamental constants. The significant improvement in the knowledge of $m_\mathrm{e}$ from CODATA-10 to CODATA-14 has led to the realization that it is more relevant to use the CODATA value of $\mu_\mathrm{de}$ in the adjustment, rather than that of $\mu_\mathrm{dp}$. Hence, we derived the appropriately modified sensitivity coefficients of the transitions concerned and determine the value of $\mu_\mathrm{pe}$. The thus found value of $\mu_\mathrm{pe}$ in this work not only differs significantly from the values reported of the same quantity determined from HD$^+$ in Refs. [33, 146], but also possesses a larger error bar. In a similar way we also determine values of $\mu_\mathrm{pe}$ from other transitions in HD$^+$, based on previously reported experimental results, and we obtain an overall value of $\mu_\mathrm{pe}$ from all available data in HD$^+$ by a least-squares adjustment. The procedure outlined here could be used for the interpretation of future Doppler-free spectroscopy experiments on HD$^+$.

## 6.6 Acknowledgments

This work received support from the French-Dutch bilateral EP Nuffic-Van Gogh program. The work of S.P., M.G. and J.C.J.K. was financed by Netherlands Organization for Scientific Research (NWO) through projects 13PR3109, Vidi 12346 and FOM-program 'The Mysterious Size of the Proton'. J.-Ph.K. and L.H. acknowledge funding from Agence Nationale de la Recherche (grant ANR-13-IS04-0002-01). J.-Ph.K. acknowledges support from a Fellowship of the Institut Universitaire de France. V.I.K. acknowledges support from the Russian Foundation for Basic Research under Grant No. 15-02-01906-a.

Chapter 7

# Observation of the $(v, L) : (0, 3) \rightarrow (9, 3)$ two-photon transition in HD$^+$

---

In this Chapter the preliminary results of the first observation of the $v = 0 \rightarrow v = 9$ vibrational overtone transition in cold, trapped HD$^+$ ions are presented. The experimental setup and procedure for this experiment is described briefly in the following paragraphs, starting with Doppler-broadened two-photon spectroscopy.

## 7.1 Doppler-broadened $(v, L) : (0, 3) \rightarrow (9, 3)$ ro-vibrational transition in HD$^+$

The starting point for two-photon excitation is a Coulomb crystal of ∼700. . .1000 laser-cooled Be$^+$ ions. The detuning of the cooling laser was fixed to $-300$ MHz relative to the resonance of the Be$^+$ laser cooling transition. The bias magnetic field was set to a high value (∼3.5 G corresponding to a current of ∼1.3 A through the main coils) to ensure efficient cooling of the Be$^+$ ions in the ion trap. The spectroscopy lasers at 1442 nm and 1445 nm were phase-locked to the OFC. While the frequency of the 1442 nm laser was fixed near the maximum ($-30$ MHz from the spin-averaged transition frequency) of the simulated spectrum of the $(v, L) : (0, 3) \rightarrow (4, 2)$ ro-vibrational transition (Fig. 4.1), the frequency of the 1445 nm laser was scanned to record a spectrum spanning 120 MHz (from $-100$ MHz to $+20$ MHz from the spin-averaged frequency of the $(v, L) : (0, 3) \rightarrow (9, 3)$ ro-vibrational transition) in steps of 10 MHz. This frequency range was based on a simulated Doppler-broadened $(v, L) : (0, 3) \rightarrow (9, 3)$ spectrum to include the strongest hyperfine components (Fig. 7.1). The $(v, L) : (0, 3) \rightarrow (4, 2)$ and $(v, L) : (4, 2) \rightarrow (9, 3)$ ro-vibrational transition frequencies were calculated from the energy values of the relevant states given in Ref. [46]. The hyperfine structure of the $(v = 0, L = 3)$ level was calculated by diagonalising the spin Hamiltonian $H_{\text{eff}}$ with coefficients taken from Ref. [48]. Similarly, the coefficients for diagonalising $H_{\text{eff}}$ for $(v = 9, L = 3)$ were obtained from [150]. The spectroscopy lasers at 1442 nm and 1445 nm were coupled into a single optical fibre and impinged on the trapped $HD^+$ ions by co-alignment with the 313 nm laser. A mechanical shutter was used to control the exposure of the trapped $HD^+$ ions to the spectroscopy lasers. The dissociation laser at 532 nm was made incident on the ions by overlapping the beam with the 313 nm laser, but in counter propagating manner. In each measurement sequence, after the $HD^+$ ions were loaded in the ion trap to form a two-component Coulomb crystal together with the laser-cooled $Be^+$ ions (with the spectroscopy lasers blocked) a secular excitation spectrum was recorded for 10 s. A scan was made by varying the frequency of the excitation electric field between 600 kHz and 1050 kHz to include the motional resonance of the trapped $HD^+$ ions. This was followed by a REMPD duration of 10 s, after which another secular excitation spectrum for 10 s was recorded. The REMPD signal was derived using Eq. 2.4. The resulting ro-vibrational spectrum is shown in Fig. 7.1.

The rate equation model as described in Chapter 4 for simulating the $(v, L) : (0, 3) \rightarrow (9, 3)$ ro-vibrational spectrum was employed to simulate the measured spectrum. As can be seen from Fig. 7.1, the measured and the simulated spectra agree qualitatively.

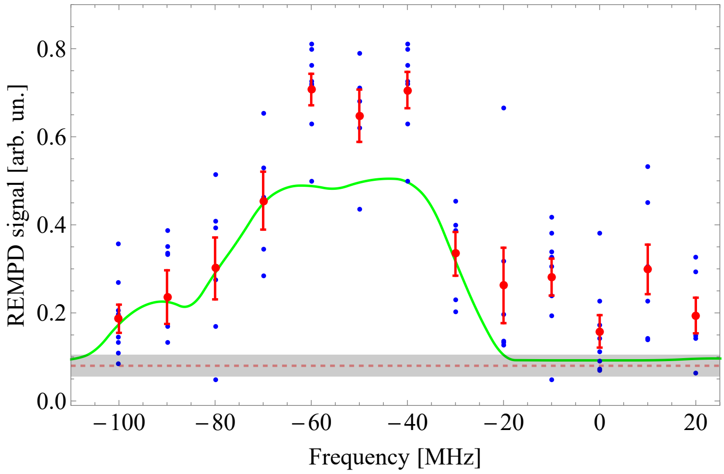

**Figure 7.1:** Measured Doppler-broadened spectrum of the $(v, L) : (0, 3) \rightarrow (9, 3)$ ro-vibrational transition in HD$^+$. The origin of the frequency axis represents the theoretically predicted spin-averaged frequency of the $(v, L) : (0, 3) \rightarrow (9, 3)$ ro-vibrational transition. Individual data points are represented by blue dots. The mean and standard deviation of the measurements at each frequency are represented by red dots and error bars, respectively. The dashed red line and the area enclosed by the grey rectangle represent the mean and standard deviation of the measured REMPD signal in absence of the probe radiation fields. For comparison, a simulated spectrum of the same transition is shown (green trace) for an HD$^+$ ion secular temperature of 20 mK, and a REMPD duration of 10 s.

## 7.2 Doppler-free two-photon $(v, L) : (0, 3) \rightarrow (9, 3)$ transition in HD$^+$

### 7.2.1 Experimental protocol and measured spectrum

The hyperfine component of the $(v, L) : (0, 3) \rightarrow (9, 3)$ overtone, which was chosen for the Doppler-free two-photon spectroscopy experiment is the one which joins states with the quantum numbers $(F = 1, S = 2, J = 5)$ in both $(v = 0, L = 3)$ and $(v = 9, L = 3)$ states. This choice was based on the analysis presented in Chapter 2, Chapter 4 and Refs. [58, 87]. The intermediate hyperfine state is the one with the quantum numbers $(F = 1, S = 2, J = 4)$ in the $(v = 4, L = 2)$ ro-vibrational state. The detuning of the 1442 nm laser was fixed to $-60$ MHz from the $(v, L) : (0, 3) \rightarrow (4, 2)$ spin-averaged transition frequency (about $-17$ MHz detuned from the chosen hyperfine component of the $(v, L) : (0, 3) \rightarrow (4, 2)$ single-photon spectrum). The frequency of the 1445 nm laser was scanned to search for the Doppler-free two-photon resonance. The frequency range over which the 1445 nm laser was scanned was obtained from an accurate *ab initio* calculation of the $(v, L) : (0, 3) \rightarrow (9, 3)$ ro-vibrational transition frequency [150]. The configuration of the laser beams used for this experiment is shown in Fig. 7.2.

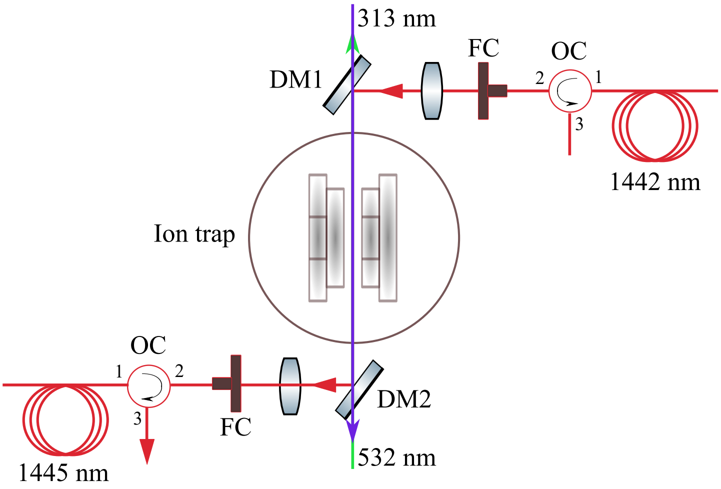

**Figure 7.2:** Schematic of the configuration of the $Be^+$ cooling laser beam at 313 nm, the dissociation laser beam at 532 nm, and the spectroscopy laser beams at 1442 nm (red arrows) and 1445 nm through the ion trap. The direction of the 1445 nm beam is opposite to that of the 1442 nm. FC, Fibre collimator; OC, Optical circulator; DM, Dichroic mirror.

The 313 nm laser beam was aligned to the $Be^+$ Coulomb crystal and the ion trap axis. A pair of irises were used to fix the alignment of the 313 nm laser and for co-aligning other laser beams to the Coulomb crystal. As can be seen in Fig. 7.2, the 1442 nm and the 1445 nm laser were made incident on the $HD^+$ ions in counter-propagating manner to suppress the first-order Doppler effect. The dissociation laser running at 532 nm was also co-aligned with the 313 nm laser, but in a counter-propagating manner. The 1442 nm laser was combined with the 313 nm laser on a dichroic mirror, while the 1445 nm laser was combined with the 532 nm dissociation laser on another dichroic mirror. Overlap of both the spectroscopy lasers with the $HD^+$ ions is crucial for efficient excitation of the Doppler-free two-photon transition. This was ensured in the following manner. The light from both the 1442 nm and the 1445 nm laser was transported to the ion trap via separate 40 m long optical fibres (see

Chapter 3). They were then collimated and focussed on the ions in the ion trap with an optical circulator in between. The light from the 1442 nm laser was co-aligned with the 313 nm laser and then coupled back into the optical fibre carrying the 1445 nm laser light into the port 2 of the optical circulator as shown in Fig. 7.2. The optical circulator ensured that the thus coupled-in 1442 nm light could not travel back to the 1445 nm ECDL and thereby destabilise the operation of the latter. Moreover, the 1442 nm light emitted from port 3 of the circulator was used to optimise the coupling efficiency ($\geq 50\%$) into the optical fibre. The principle of reversibility of light rays then ensures that the 1445 nm light is also overlapped with the 1442 nm beam and hence also with the $\mathrm{HD}^+$ ions in the trap.

During secular excitation, the detuning of the 313 nm laser was fixed to $-300$ MHz relative to the resonance of the $\mathrm{Be}^+$ laser cooling transition, and the maximum available UV power ($\sim$2 mW) was used. During REMPD, the detuning of the 313 nm laser was reduced to $-50$ MHz (with respect to the $\mathrm{Be}^+$ cooling resonance) and the power was limited to $\sim$150 $\mu$W. Similarly, during secular excitation, a high bias magnetic field was used ($\sim$1.1 G, corresponding to a current of 393 mA through the main coils) while during REMPD a low field was used ($\sim$125 mG, corresponding to a current of 46 mA). The typical values of the power used during the experiment are $\sim$6 mW, $\sim$8 mW and $\sim$85 mW for the 1442 nm, 1445 nm and the 532 nm lasers, respectively. A REMPD duration of 30 s was used as justified in Appendix 7.A. Each measurement sequence started with the creation of a bicomponent $\mathrm{Be}^+/\mathrm{HD}^+$ Coulomb crystal (typically consisting of 1000...1500 $\mathrm{Be}^+$ ions and 40...80 $\mathrm{HD}^+$ ions), followed by a secular excitation scan of 10 s, a REMPD duration of 30 s, and finally another secular excitation scan of 10 s. The bias magnetic field, 313 nm laser power and detuning were also tuned accordingly as mentioned above. The secular excitation spectrum was recorded by both a PMT and an EMCCD camera. In this manner, a spectrum was recorded in a frequency range of 60 kHz in steps of 2 kHz. The order in which the frequencies were measured was randomised using a random number sequence generator in *Mathematica* to randomise the effect of drift of parameters such as laser power, beam alignment, background losses in the ion trap during REMPD, etc. The resulting spectrum, recorded in a period of about 8 weeks (end of August 2018 to end of October 2018) is shown in Fig. 7.3.

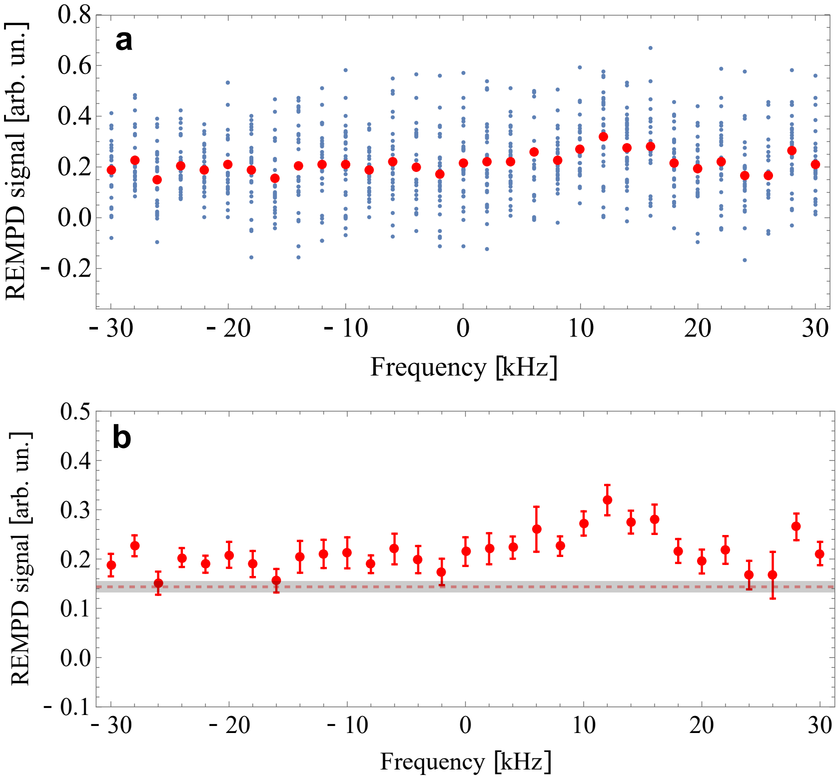

**Figure 7.3:** Recorded Doppler-free two-photon spectrum of a single hyperfine component of the $(v, L) : (0,3) \rightarrow (9,3)$ ro-vibrational transition. The target hyperfine component connects states with same spin quantum numbers $(F = 1, S = 2, J = 5)$ in the $(v = 0, L = 3)$ and $(v = 9, L = 3)$ ro-vibrational levels. Individual data points are represented by blue dots and the means of the dataset at each frequency are represented by black dots in (a). In (b), only the average and standard deviation (error bar) at each frequency is plotted. The dashed red line and the area enclosed by the grey rectangle in (b) represent the mean and standard deviation of the measured REMPD signal in absence of the probe radiation fields.

As can be seen from Fig. 7.3a, in the raw data without averaging, there is no clear resonance visible. However, for the averaged signal in Fig. 7.3b, a possible peak can be observed centred at ≈12 kHz. To further analyse whether there is indeed a Doppler-free two-photon feature in the measured spectrum, a statistical procedure based on Welch's $t$-test [151] was developed to identify whether there is any signal underlying the noise in the measured spectrum.

This method is described in further detail in the following section.

### 7.2.2 Statistical test to distinguish "signal" from "noise"

**The statistical test**

The spectrum was recorded in a range of 60 kHz, of which ~50 kHz is expected to contribute to the Doppler-broadened background and ~8...10 kHz to the lineshape of the Doppler-free two-photon transition based on the discussions in Chapter 4. The essence of the statistical model is as follows. A window of 8 kHz is scanned over the entire spectrum which is considered to contain the "signal", while at the same time regarding the rest as "background". Mean and standard deviation of the signal, $\overline{X}_\mathrm{s}$ and $\sigma_\mathrm{s}$, as well as those of the background, $\overline{X}_\mathrm{bg}$ and $\sigma_\mathrm{bg}$, are calculated. The statistical significance of the difference between $\overline{X}_\mathrm{s}$ and $\overline{X}_\mathrm{bg}$ is then tested using Welch's *t*-test. If the signal window indeed contains the signal, then the background constitutes only the Doppler-broadened background, and its mean is known with high precision as the number of data points in the background is much larger than that of the signal. It should be noted here that this test is designed to only identify the difference in the means of the signal and the background with some statistical significance, and assumes no implicit lineshape for the signal. In Fig. 7.4, this is explained with a simulated two-photon spectrum.

The simulated Doppler-free two-photon spectrum as shown in Fig. 7.4 is generated as follows. The finite number of $HD^+$ ions during REMPD leads to signal variation according to a Poisson distribution. A REMPD datum can be generated by taking a random number from a Poisson distribution with the mean $\eta \cdot N_{\mathrm{HD}^+}$ and normalising to $N_{\mathrm{HD}^+}$, where $\eta$ is the average fractional loss of $HD^+$ ions and $N_{\mathrm{HD}^+}$ is the initial number of $HD^+$ ions. Measurement noise is added in the form of Gaussian noise. In this manner, a set of $n$ REMPD data can be generated. A Lorentzian lineshape function[1], together with a knowledge of the initial number of $HD^+$ ions during a measurement sequence, noise level and number of measurements were used to generate a set of REMPD data to mimic an expected experimentally recorded spectrum as shown in Fig. 7.4.

---

[1] The choice of a Lorentzian lineshape is justified in Chapter 4.

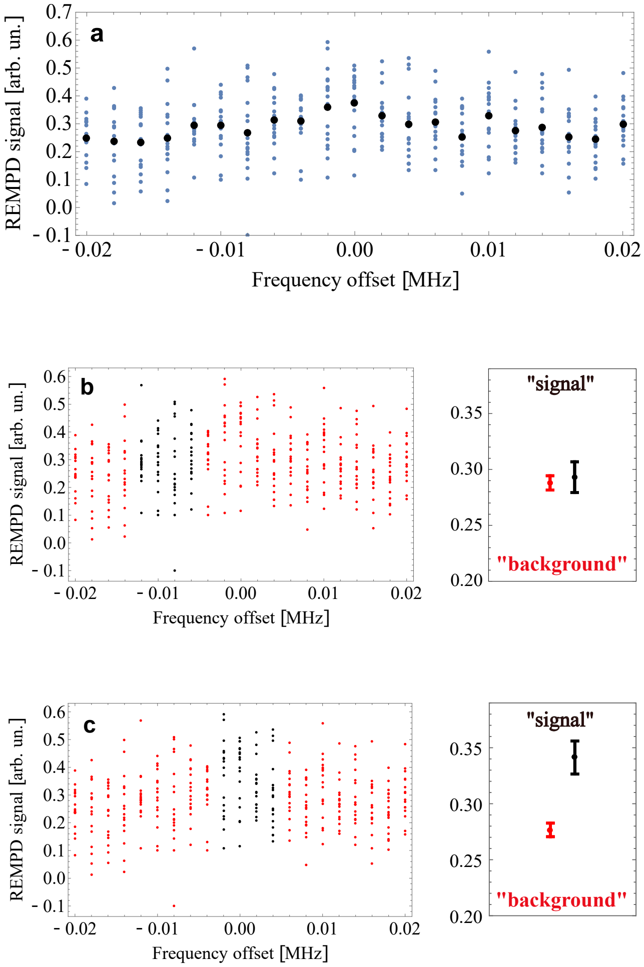

**Figure 7.4:** A simulated REMPD data set in a 40 kHz frequency range with an underlying Lorentzian lineshape (individual datapoints in blue and the mean values in black) is shown in (a) with the peak of the lineshape at 0 MHz with an amplitude of 0.37 and an FWHM of 8 kHz. A signal window of 8 kHz (corresponding to the FWHM of the Lorentzian) is moved over the entire 40 kHz range of the simulated spectrum. In (b) the signal window is selected such that it does not include the peak of the lineshape. It can be seen that the mean of the signal window (represented by black points) is similar to the background (represented by red points). In (c), it can be observed that when the signal window includes the peak of the Lorentzian lineshape, that its mean is significantly higher than that of the background.

In the next subsection, the Welch's $t$-test is briefly introduced and applied on the simulated two-photon spectrum shown in Fig. 7.4a.

### Welch's *t*-test

Welch's $t$-test is an adaptation of the Student's $t$-test [152], commonly used in Statistical hypothesis testing [153]. The Welch's $t$-test is more reliable than the Student's $t$-test in cases where the samples to be compared have different sample sizes and variances. However, both require the condition that both the populations from which the samples are from are normally distributed.
The statistic $t$ used for the Welch's $t$-test is defined as

$$t = \frac{\overline{X}_1 - \overline{X}_2}{\sqrt{\frac{s_1^2}{N_1} + \frac{s_2^2}{N_2}}}, \tag{7.1}$$

where $\overline{X}_n$, $s_n^2$ and $N_n$ $(n = 1, 2)$ are the sample means, sample variances and sample sizes, respectively of the two samples to be compared. The degrees of freedom corresponding to this statistic is defined as

$$\nu \approx \frac{\left(\frac{s_1^2}{N_1} + \frac{s_2^2}{N_2}\right)^2}{\frac{s_1^4}{N_1^2 \nu_1} + \frac{s_2^4}{N_2^2 \nu_2}}, \tag{7.2}$$

where $\nu_n = N_n - 1$ $(n = 1, 2)$ represents the degrees of freedom associated with the variance estimates of the two samples. The statistic $t$ and the degrees of freedom $\nu$ can then be inserted in the cumulative distribution function of the Student's $t$-distribution to find a $p$-value. In statistical hypothesis testing, the $p$-value gives the probability that a certain test statistic (mean, variance etc.), for a given null hypothesis (statistical model resulting in a data set due to random processes only) is equal to or more extreme than what is actually observed. The $p$-value can be converted to a $Z$ value via the relation

$$Z = \sqrt{2}\,\mathrm{erf}^{-1}(1 - 2p). \tag{7.3}$$

The $Z$ value gives the number of Gaussian standard deviations ($\sigma$) that the observation is away from the mean, given the null hypothesis is valid [154].
In Fig 7.5, results are shown for the Welch's $t$-test applied to the simulated two-photon spectrum (shown in Fig. 7.4a) and for a spectrum simulated with pure noise.

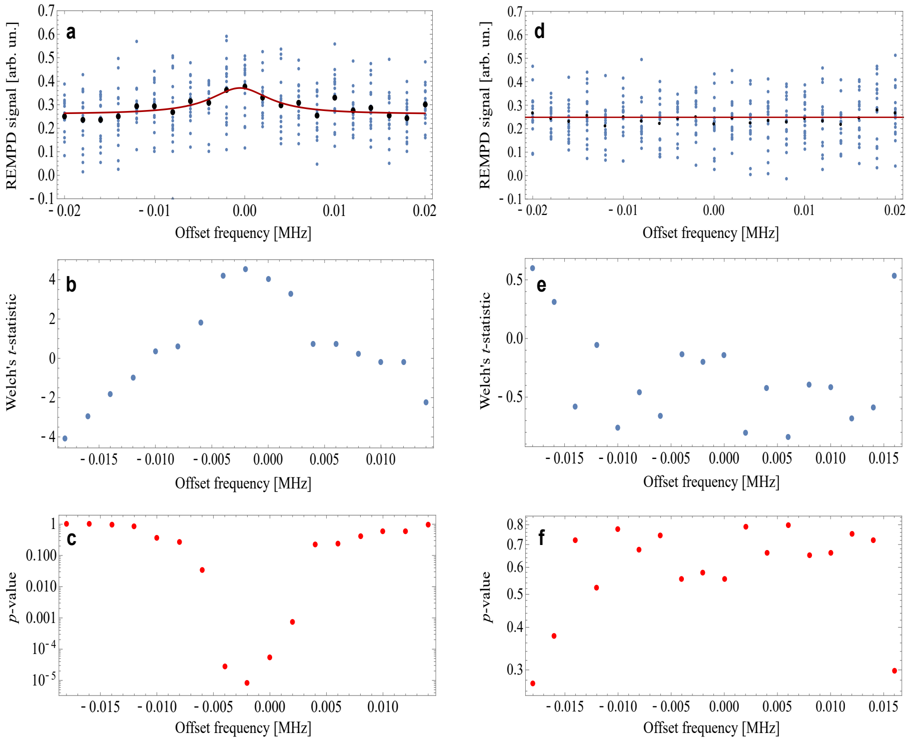

**Figure 7.5:** Welch's $t$-test applied to a simulated spectrum consisting of a Lorentzian lineshape (a-c) and pure noise (d-f) is shown. Note the difference in the vertical scales.

From Fig. 7.5, it is evident that only with a signal present, the $p$-value thus calculated becomes $\sim 10^{-5}$ at the frequency position of the peak of the Lorentzian lineshape, whereas for pure noise, the $p$-value remains significantly larger. The statistical test thus developed, can be reliably used to provide "evidence" for the existence of the Doppler-free two-photon transition in the measured spectrum.

### Statistical analysis of the measured spectrum: Evidence of Doppler-free feature in the measured spectrum

The results of applying the Welch's $t$-test to the measured spectrum are shown in Fig 7.6.

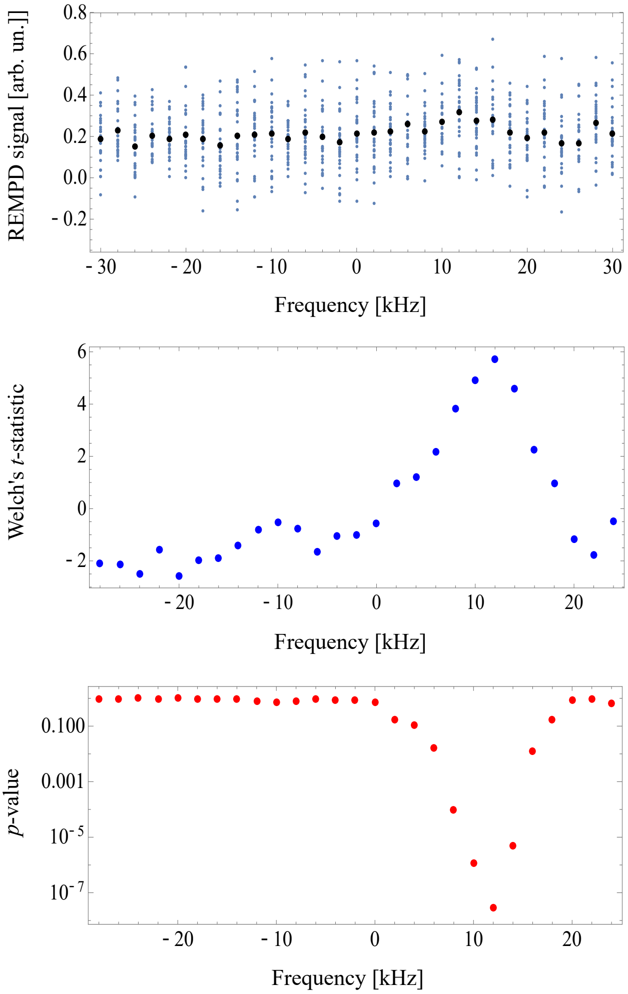

**Figure 7.6:** The measured spectrum, the Welch's $t$-statistic, and the $p$-value are shown. A $p$-value of $2.9 \times 10^{-8}$ was obtained at a frequency of 12 kHz.

From Fig 7.6, it can be inferred that statistically, there is "evidence" of a Doppler-free two-photon peak of the $(v, L) : (0, 3) \rightarrow (9, 3)$ ro-vibrational transition in HD$^+$ in the measured spectrum. The minimum $p$-value of $2.9 \times 10^{-8}$ corresponds to a $Z$ value of 5.4 ($5.4\sigma$).
Additionally, simulations with noise level similar to that observed in the measured spectrum were performed to find out the probability of "false positives".

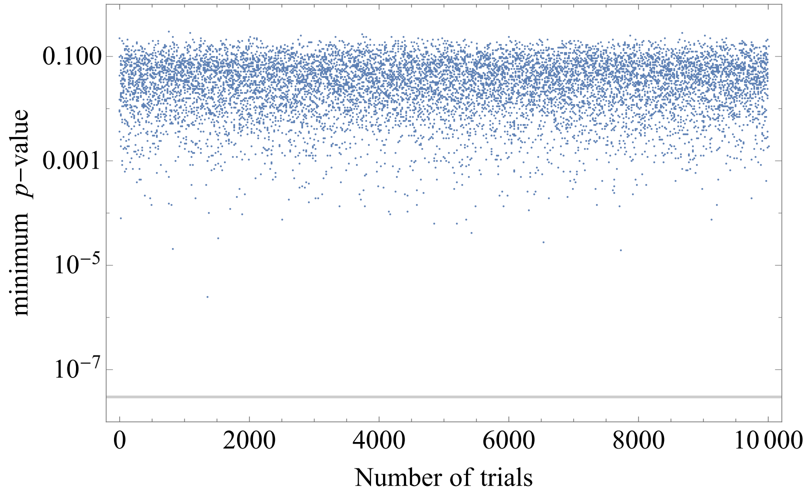

**Figure 7.7:** Minimum $p$-values of 10000 trials of simulated spectra with pure noise with levels comparable to the measured spectrum is shown. The grey line indicates the minimum $p$-value calculated for the measured spectrum.

A false positive is an instance where a feature as observed in the measured spectrum is generated due to pure noise with a $p$-value similar to, or less than, that calculated for the measured spectrum. Of the 10000 trials performed, no instance was observed to have a $p$-value $< 3 \times 10^{-8}$ (Fig. 7.7).

In Fig. 7.8, the measured spectrum is fitted with a Lorentzian lineshape function as described in Sec. 4.3.3 of Chapter 4. The fit routine is found to be robust with respect to initial fit parameters. The fitted Lorentzian lineshape function also leads to a width and amplitude of the peak in agreement with expected values from the simulated two-photon spectrum.

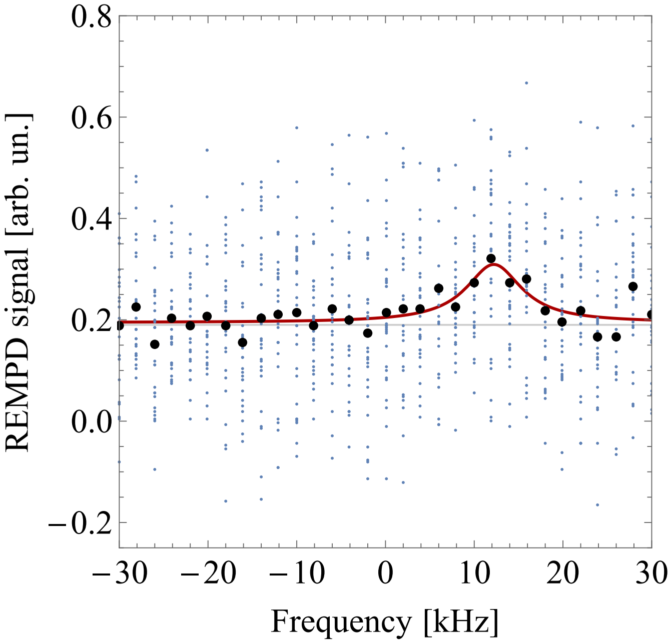

**Figure 7.8:** Measured spectrum of the hyperfine component $(F, S, J) : (1, 2, 5) \rightarrow (1, 2, 5)$ of the two-photon $(v, L) : (0, 3) \rightarrow (9, 3)$ ro-vibrational transition in HD$^+$ is fitted with a Lorentzian lineshape model as mentioned in the text. The width of the fitted lineshape is found to be $7.63 \pm 2.53$ kHz and the uncertainty (standard deviation) of the fitted centre frequency is 0.75 kHz. The origin of the frequency axis is at an arbitrary position as more measurements are required to assess all the systematic effects.

The observation of an isolated hyperfine component (Fig. 7.8) is a promising step towards an experimental determination of the spin-averaged frequency of the $(v, L) : (0, 3) \rightarrow (9, 3)$ ro-vibrational transition at the parts-per-trillion level, provided all the systematic effects are estimated correctly. Evaluation of the systematic effects and a precise determination of the spin-averaged transition frequency is part of a future endeavour.

## 7.A Choice of optimum REMPD duration for the Doppler-free two-photon spectroscopy experiment

As mentioned in Chapter 4, it is useful to determine *a priori* experimental parameters such as laser detunings and intensities, optimum REMPD duration, magnetic fields etc. as experimental optimisation of these quantities can be tedious. Here we discuss the method to determine the optimum REMPD duration for the Doppler-free two-photon spectroscopy experiment.

A signal $s(\tau)$, which is used to find an optimum REMPD duration is defined as

$$s(\tau) = \eta_{\mathrm{peak}}(\tau) - \eta_{\mathrm{bg}}(\tau), \tag{7.4}$$

where $\eta_{\mathrm{peak}}(\tau)$ and $\eta_{\mathrm{bg}}(\tau)$ are the fractional $\mathrm{HD}^+$ losses after a REMPD duration of $\tau$, at the peak of the Doppler-free feature and 50 kHz away from it (i.e., only background signal), respectively. $\eta_{\mathrm{peak}}(\tau)$ and $\eta_{\mathrm{bg}}(\tau)$ include both the losses due to REMPD and collisions with background gas molecules. They are obtained using the rate equation model developed in Chapter 4. In Fig. 7.9, $\eta_{\mathrm{peak}}(\tau)$ and $\eta_{\mathrm{bg}}(\tau)$ are plotted for REMPD durations ranging from 5 s to 200 s.

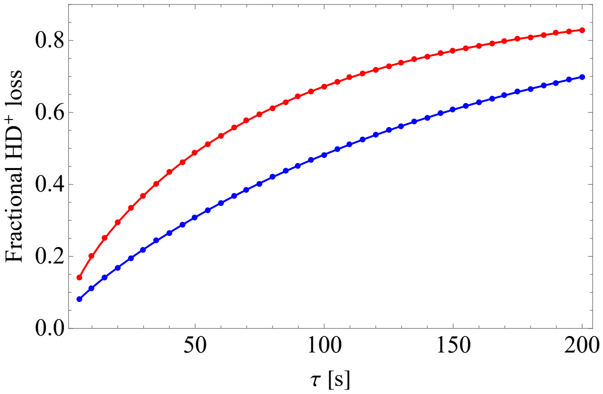

**Figure 7.9:** Time evolution of $\eta_{\mathrm{peak}}(\tau)$ (red) and $\eta_{\mathrm{bg}}(\tau)$ (blue) is plotted versus REMPD duration $\tau$. An $\mathrm{HD}^+$ ion secular temperature of 10 mK, a BBR temperature of 300 K and a detuning of $-60$ MHz from the spin-averaged frequency of the $(v, L) : (0, 3) \rightarrow (4, 2)$ ro-vibrational transition of the 1442 nm laser were assumed for the simulations. The laser beam parameters were assumed to be same for both the 1442 nm and 1445 nm lasers: 5 mW of laser light focussed in a beam of waist 150 $\mu$m. Individual data points represent fractional losses of $\mathrm{HD}^+$ ions simulated for REMPD durations ranging from 5 s to 200 s at intervals of 5 s. The smooth curves are generated by fitting a third-order interpolating function to the data points.

A signal-to-noise ratio in this case can then be defined as

$$\chi(\tau) = \frac{s(\tau)}{\sqrt{2\sigma_{\mathrm{instr}}^2 + \frac{\eta_{\mathrm{peak}}}{N_{\mathrm{HD}^+}} + \frac{\eta_{\mathrm{bg}}}{N_{\mathrm{HD}^+}}}}, \tag{7.5}$$

where $\sigma_{\mathrm{instr}}^2$ is the variance of the instrumental noise and $\frac{\eta_{\mathrm{peak}}}{N_{\mathrm{HD}^+}}$ and $\frac{\eta_{\mathrm{bg}}}{N_{\mathrm{HD}^+}}$ are the variances of the Poissionian noise distribution, which underlies the REMPD data (see Sec. 7.2.2 of Chapter 7). $N_{\mathrm{HD}^+}$ is the initial number of $\mathrm{HD}^+$ ions in the sample. The factor of 2 before $\sigma_{\mathrm{instr}}^2$ is due to the fact that the instrumental noise is present both in the peak and the background REMPD data. A plot of the signal-to-noise ratio versus REMPD duration is shown in Fig. 7.10.

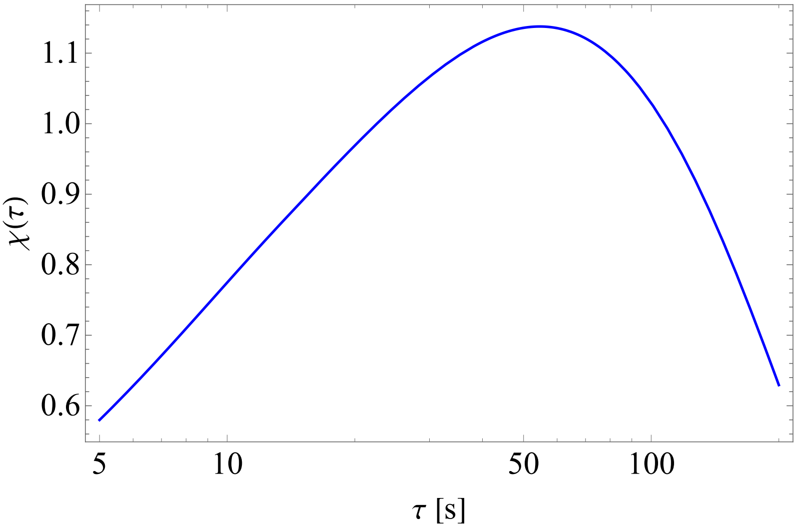

**Figure 7.10:** The signal-to-noise ratio $\chi(\tau)$ is plotted against REMPD duration $\tau$. $\sigma_{\mathrm{instr}}$ is assumed to be 0.05 and $N_{\mathrm{HD}^+}$ is assumed to be 40.

A figure of merit $\mathcal{L}(\tau)$ may now be defined as [87]

$$\mathcal{L}(\tau) = \chi(\tau)\sqrt{\left\lfloor \frac{T_{\mathrm{exp}}}{\tau + \tau_{\mathrm{oh}}} \right\rfloor}, \tag{7.6}$$

where $T_{\mathrm{exp}}$ is the duration of a measurement campaign, $\tau$ is the REMPD duration and $\tau_{\mathrm{oh}}$ is the overhead for each measurement (i.e., $\tau_{\mathrm{oh}}$ represents the time

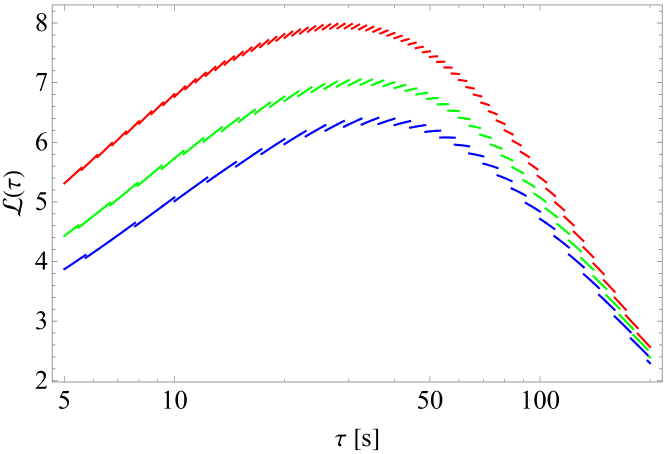

**Figure 7.11:** The figure of merit $\mathcal{L}(\tau)$ is plotted against $\tau$ for different $\tau_{\mathrm{oh}}$. The red, green and blue traces correspond to $\tau_{\mathrm{oh}} = 40$ s, 60 s and 80 s respectively. For each case, the optimum REMPD duration corresponds to the maximum of each curve. The curves also indicate the degradation of the overall data acquisition efficiency for sub-optimum REMPD duration. The discontinuous structures of the traces are due to the floor function in Eq. 7.6.

required in one experimental cycle other than the REMPD duration, which includes the time required for loading HD$^+$ ions, secular excitations, switching of magnetic fields, opening and closing of mechanical shutters, tuning the frequencies of the cooling and spectroscopy lasers, etc.).

The figure of merit $\mathcal{L}(\tau)$ can then be optimised for a range of different experimental parameters to find out the optimum REMPD duration. In Figs. 7.11-7.13, the figure of merit function is plotted for different $\tau_{\mathrm{oh}}$, $N_{\mathrm{HD^+}}$ and $\sigma_{\mathrm{instr}}$, respectively.

From Figs. 7.11-7.13, it can be observed that the optimum REMPD duration is at about 40 s. However, it must be noted here that aspects such as random unlocking of the lasers used in the experiments has not been taken into account in this optimisation process due to lack of statistical data. Hence, a slightly shorter REMPD duration of 30 s was chosen, as the SNR does not degrade significantly compared to the optimal REMPD duration and at the same time makes the experimental cycles more robust with respect to random unlocking of the lasers involved.

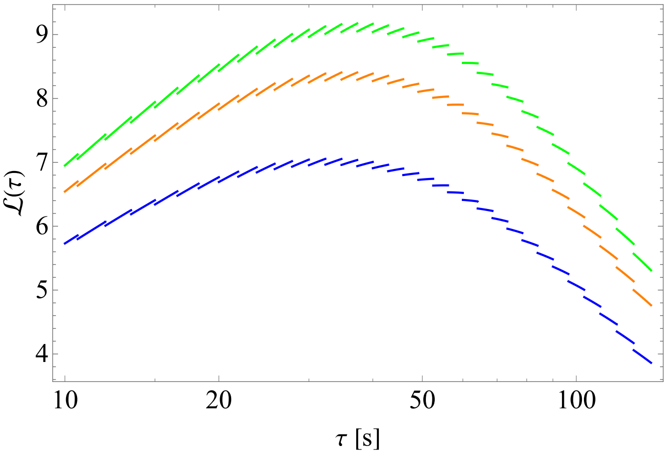

**Figure 7.12:** The figure of merit $\mathcal{L}(\tau)$ is plotted against $\tau$ for different ion numbers $N_{\mathrm{HD+}}$. The green, orange and blue traces correspond to $N_{\mathrm{HD+}} = 100$, 75 and 45, respectively.

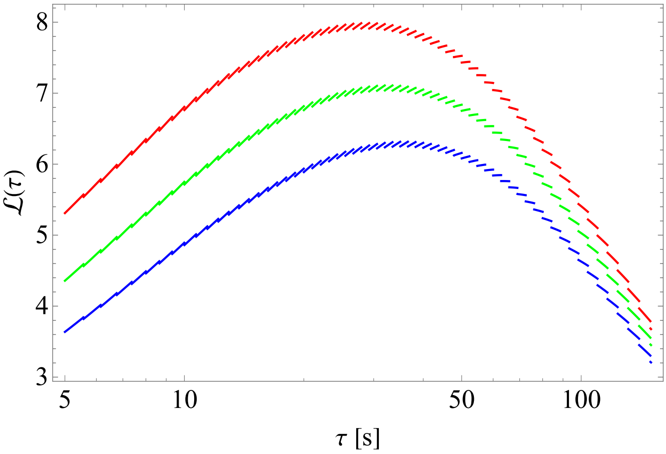

**Figure 7.13:** $\mathcal{L}(\tau)$ is plotted against $\tau$ for different values of $\sigma_{\mathrm{instr}}$. The red, green and blue traces correspond to $\sigma_{\mathrm{instr}} = 0.05$, 0.07 and 0.09 respectively.

## Chapter 8

# Conclusion and Outlook

In this thesis, the design, development and progress of an experiment towards Doppler-free two-photon spectroscopy of the $(v, L) : (0, 3) \rightarrow (9, 3)$ ro-vibrational transition in trapped and cooled $\mathrm{HD}^+$ molecular ions has been discussed. The target precision of this experiment is $\sim 10^{-12}$ in relative frequency uncertainty terms, which would allow the most stringent test of molecular theory (at the parts-per-trillion level) in molecules. Comparison with *ab initio* calculation of the transition frequencies holds some interesting prospects. Some of them are discussed briefly below.

Of particular interest is the determination of the values of any fundamental constants from the set $\{R_\infty, \mu_{\mathrm{pe}}, \mu_{\mathrm{de}}, r_{\mathrm{p}}, r_{\mathrm{d}}\}$ from ro-vibrational spectroscopy of hydrogen molecular ions, as was described in Ref. [59]. The present experiment, with its target precision of 12 decimal places would contribute towards that goal.

Recently, the experiments described in Refs. [31, 62–64] have questioned the accuracy of several of these fundamental constants as given by the CODATA recommended values. For example, in Ref. [62, 63], the authors have measured the proton and deuteron charge radii $r_{\mathrm{p}}$ and $r_{\mathrm{d}}$ via spectroscopy of muonic hydrogen and deuterium, respectively. These measurements are more precise than CODATA-14 and showed discrepancies of $5.4\sigma$ [1] [62] and $6.0\sigma$ ($7.5\sigma$ with respect to CODATA-10 [19]) [63] on $r_{\mathrm{p}}$ and $r_{\mathrm{d}}$ respectively from the CODATA-14 recommendations. Following up on that, in 2016, an updated value of $r_{\mathrm{p}}$ from muonic hydrogen was published in Ref. [156], leading to a discrepancy of $5.6\sigma$ with the CODATA-14 recommendation of $r_{\mathrm{p}}$. In 2017, a measurement of

---

[1] The $5.0\sigma$ uncertainty mentioned in Ref. [62] is with respect to CODATA-06 [155], which was the latest CODATA recommendation of the fundamental constants at the time of the publication.

the $2S$-$4P$ transition in atomic hydrogen determined $r_\mathrm{p}$ with a precision comparable to the CODATA-14 recommended value, but with a $3.3\sigma$ discrepancy from the world average of $r_\mathrm{p}$ data from atomic hydrogen spectroscopy [64]. More recently, in 2018, a measurement of the $1S$-$3S$ two-photon transition in atomic electronic hydrogen with a fractional frequency uncertainty of $9 \times 10^{-13}$ has led to the determination of the proton charge radius, $r_\mathrm{p} = 0.877(13)$ fm, consistent with CODATA-14 [65], thereby further intesifying the debate on the value of the proton charge radius. The anomaly in the proton charge radius $r_\mathrm{p}$ as determined from muonic hyrdogen in Ref. [62] provides a frequency shift of $\sim +5.3$ kHz on the $(v, L) : (0, 3) \to (9, 3)$ transition in HD$^+$. Hence, a combined experimental and theoretical uncertainty of the present experiment in HD$^+$ smaller than 5.3 kHz would allow us to contribute to this "proton radius puzzle".

In 2017, the proton atomic mass $m_\mathrm{p}$ was also determined with 3 times more precision than its CODATA-14 recommended value, but with more than $3\sigma$ discrepancy from the latter [31]. The dependence of the $(v, L) : (0, 3) \to (9, 3)$ transition frequency in HD$^+$ to a change in the proton atomic mass $m_\mathrm{p}$ can be expressed as

$$\frac{\delta m_\mathrm{p}}{m_\mathrm{p}} = -4.25 \frac{\delta \nu}{\nu}, \tag{8.1}$$

where the sensitivity coefficient $-4.25$ has been calculated following the approach of Ref. [60]. This leads to a frequency shift of $\sim +28.7$ kHz on the $(v, L) : (0, 3) \to (9, 3)$ two-photon transition. However, according to Eq. 1.2, the relevant parameter for comparison is the proton-electron mass ratio $\mu_\mathrm{pe}$, which is also determined in Ref. [31] with a relative uncertainty of 43 ppt. A combined experimental and theoretical relative frequency uncertainty[2] $\sim 1 \times 10^{-11}$ of the Doppler-free two-photon spectroscopy of $(v, L) : (0, 3) \to (9, 3)$ ro-vibrational transition in HD$^+$ would allow a consistency check of the $m_\mathrm{p}$ determination from Ref. [31]. The 7.6 kHz FWHM of a single hyperfine component of the $(v, L) : (0, 3) \to (9, 3)$ transition (Fig. 7.8) is an encouraging first step towards that direction.

Doppler-free two-photon spectroscopy of ro-vibrational transitions in HD$^+$ therefore provides a promising route towards determination of fundamental constants, thereby allowing for consistency checks on their determination from different systems.

---

[2] Theoretical uncertainty of the spin-averaged $(v, L) : (0, 3) \to (9, 3)$ ro-vibrational transition frequency in HD$^+$ is $\sim 8 \times 10^{-12}$ in fractional frequency uncertainty terms (Jean-Philippe Karr, private communication).

# Bibliography

[1] P. A. M. Dirac, "The quantum theory of the emission and absorption of radiation," *Proceedings of the Royal Society of London A: Mathematical, Physical and Engineering Sciences*, vol. 114, no. 767, pp. 243–265, 1927.

[2] P. A. M. Dirac, "The quantum theory of the electron," *Proceedings of the Royal Society of London A: Mathematical, Physical and Engineering Sciences*, vol. 117, no. 778, pp. 610–624, 1928.

[3] P. A. M. Dirac, "A theory of electrons and protons," *Proceedings of the Royal Society of London A: Mathematical, Physical and Engineering Sciences*, vol. 126, no. 801, pp. 360–365, 1930.

[4] C. D. Anderson, "The positive electron," *Physical Review*, vol. 43, pp. 491–494, 1933.

[5] J. R. Oppenheimer, "Note on the theory of the interaction of field and matter," *Physical Review*, vol. 35, pp. 461–477, 1930.

[6] F. Bloch and A. Nordsieck, "Note on the radiation field of the electron," *Physical Review*, vol. 52, pp. 54–59, 1937.

[7] V. F. Weisskopf, "On the self-energy and the electromagnetic field of the electron," *Physical Review*, vol. 56, pp. 72–85, 1939.

[8] H. M. Foley and P. Kusch, "On the intrinsic moment of the electron," *Physical Review*, vol. 73, pp. 412–412, 1948.

[9] P. Kusch and H. M. Foley, "Precision measurement of the ratio of the atomic '$g$ values' in the ${}^2p_{\frac{3}{2}}$ and ${}^2p_{\frac{1}{2}}$ states of gallium," *Physical Review*, vol. 72, pp. 1256–1257, 1947.

[10] P. Kusch and H. M. Foley, "The magnetic moment of the electron," *Physical Review*, vol. 74, pp. 250–263, 1948.

[11] W. E. Lamb and R. C. Retherford, "Fine structure of the hydrogen atom by a microwave method," *Physical Review*, vol. 72, pp. 241–243, 1947.

[12] J. E. Nafe, E. B. Nelson, and I. I. Rabi, "The hyperfine structure of atomic hydrogen and deuterium," *Physical Review*, vol. 71, pp. 914–915, 1947.

[13] H. A. Bethe, "The electromagnetic shift of energy levels," *Physical Review*, vol. 72, pp. 339–341, 1947.

[14] J. Schwinger, "On quantum-electrodynamics and the magnetic moment of the electron," *Physical Review*, vol. 73, pp. 416–417, 1948.

[15] R. P. Feynman, "The theory of positrons," *Physical Review*, vol. 76, pp. 749–759, 1949.

[16] F. J. Dyson, "The radiation theories of Tomonaga, Schwinger, and Feynman," *Physical Review*, vol. 75, pp. 486–502, 1949.

[17] E. R. Cohen and B. N. Taylor, "The 1973 leastsquares adjustment of the fundamental constants," *Journal of Physical and Chemical Reference Data*, vol. 2, no. 4, pp. 663–734, 1973.

[18] P. J. Mohr, D. B. Newell, and B. N. Taylor, "CODATA recommended values of the fundamental physical constants: 2014," *Review of Modern Physics*, vol. 88, p. 035009, 2016.

[19] P. J. Mohr, B. N. Taylor, and D. B. Newell, "CODATA recommended values of the fundamental physical constants: 2010," *Review of Modern Physics*, vol. 84, pp. 1527–1605, 2012.

[20] A. Wicht, J. M. Hensley, E. Sarajlic, and S. Chu, "A preliminary measurement of the fine structure constant based on atom interferometry," *Physica Scripta*, vol. 2002, no. T102, p. 82, 2002.

[21] R. Bouchendira, P. Cladé, S. Guellati-Khélifa, F. Nez, and F. Biraben, "New determination of the fine structure constant and test of the quantum electrodynamics," *Physical Review Letters*, vol. 106, p. 080801, 2011.

[22] A. Jeffery, R. E. Elmquist, J. Q. Shields, L. H. Lee, M. E. Cage, S. H. Shields, and R. F. Dziuba, "Determination of the von Klitzing constant and the fine-structure constant through a comparison of the quantized hall resistance and the ohm derived from the NIST calculable capacitor," *Metrologia*, vol. 35, no. 2, p. 83, 1998.

[23] D. Hanneke, S. Fogwell, and G. Gabrielse, "New measurement of the electron magnetic moment and the fine structure constant," *Physical Review Letters*, vol. 100, p. 120801, 2008.

[24] R. H. Parker, C. Yu, W. Zhong, B. Estey, and H. Müller, “Measurement of the fine-structure constant as a test of the standard model,” *Science*, vol. 360, no. 6385, pp. 191–195, 2018.

[25] G. Gräff, H. Kalinowsky, and J. Traut, “A direct determination of the proton electron mass ratio,” *Zeitschrift für Physik A Atoms and Nuclei*, vol. 297, no. 1, pp. 35–39, 1980.

[26] R. V. Dyck, F. Moore, D. Farnham, and P. Schwinberg, “New measurement of the proton-electron mass ratio,” *International Journal of Mass Spectrometry and Ion Processes*, vol. 66, no. 3, pp. 327 – 337, 1985.

[27] D. L. Farnham, R. S. Van Dyck, and P. B. Schwinberg, “Determination of the electron’s atomic mass and the proton/electron mass ratio via Penning trap mass spectroscopy,” *Physical Review Letters*, vol. 75, pp. 3598–3601, 1995.

[28] J. Verdú, S. Djekić, S. Stahl, T. Valenzuela, M. Vogel, G. Werth, T. Beier, H.-J. Kluge, and W. Quint, “Electronic $g$ factor of hydrogenlike oxygen $^{16}O^{7+}$,” *Physical Review Letters*, vol. 92, p. 093002, 2004.

[29] M. Hori, A. Sótér, D. Barna, A. Dax, R. Hayano, S. Friedreich, B. Juhász, T. Pask, E. Widmann, D. Horváth, L. Venturelli, and N. Zurlo, “Two-photon laser spectroscopy of antiprotonic helium and the antiproton-to-electron mass ratio,” *Nature*, vol. 475, p. 484, 2011.

[30] S. Sturm, F. Köhler, J. Zatorski, A. Wagner, Z. Harman, G. Werth, W. Quint, C. H. Keitel, and K. Blaum, “High-precision measurement of the atomic mass of the electron,” *Nature*, vol. 506, p. 467, 2014.

[31] F. Heiße, F. Köhler-Langes, S. Rau, J. Hou, S. Junck, A. Kracke, A. Mooser, W. Quint, S. Ulmer, G. Werth, K. Blaum, and S. Sturm, “High-precision measurement of the proton’s atomic mass,” *Physical Review Letters*, vol. 119, p. 033001, 2017.

[32] W. H. Wing, G. A. Ruff, W. E. Lamb, and J. J. Spezeski, “Observation of the infrared spectrum of the hydrogen molecular ion $HD^+$,” *Physical Review Letters*, vol. 36, pp. 1488–1491, 1976.

[33] J. Biesheuvel, J. P. Karr, L. Hilico, K. S. E. Eikema, W. Ubachs, and J. C. J. Koelemeij, “Probing QED and fundamental constants through laser spectroscopy of vibrational transitions in $HD^+$,” *Nature Communications*, vol. 7, p. 10385, 2016.

[34] C. G. Parthey, A. Matveev, J. Alnis, B. Bernhardt, A. Beyer, R. Holzwarth, A. Maistrou, R. Pohl, K. Predehl, T. Udem, T. Wilken, N. Kolachevsky, M. Abgrall, D. Rovera, C. Salomon, P. Laurent, and T. W. Hänsch, "Improved measurement of the hydrogen $1s - 2s$ transition frequency," *Physical Review Letters*, vol. 107, p. 203001, 2011.

[35] A. Matveev, C. G. Parthey, K. Predehl, J. Alnis, A. Beyer, R. Holzwarth, T. Udem, T. Wilken, N. Kolachevsky, M. Abgrall, D. Rovera, C. Salomon, P. Laurent, G. Grosche, O. Terra, T. Legero, H. Schnatz, S. Weyers, B. Altschul, and T. W. Hänsch, "Precision measurement of the hydrogen $1s{-}2s$ frequency via a 920-km fiber link," *Physical Review Letters*, vol. 110, p. 230801, 2013.

[36] P. Czachorowski, M. Puchalski, J. Komasa, and K. Pachucki, "Nonadiabatic relativistic correction in $H_2$, $D_2$, and HD," *Physical Review A*, vol. 98, p. 052506, 2018.

[37] C.-F. Cheng, J. Hussels, M. Niu, H. L. Bethlem, K. S. E. Eikema, E. J. Salumbides, W. Ubachs, M. Beyer, N. Hölsch, J. A. Agner, F. Merkt, L.-G. Tao, S.-M. Hu, and C. Jungen, "Dissociation energy of the hydrogen molecule at $10^{-9}$ accuracy," *Physical Review Letters*, vol. 121, p. 013001, 2018.

[38] C.-F. Cheng, Y. R. Sun, H. Pan, J. Wang, A.-W. Liu, A. Campargue, and S.-M. Hu, "Electric-quadrupole transition of $H_2$ determined to $10^{-9}$ precision," *Physical Review A*, vol. 85, p. 024501, 2012.

[39] M. Niu, E. Salumbides, G. Dickenson, K. Eikema, and W. Ubachs, "Precision spectroscopy of the $X^1\Sigma_g^+, v = 0 \rightarrow 1(J = 02)$ rovibrational splittings in $H_2$, HD and $D_2$," *Journal of Molecular Spectroscopy*, vol. 300, pp. 44 – 54, 2014.

[40] F. M. J. Cozijn, P. Dupré, E. J. Salumbides, K. S. E. Eikema, and W. Ubachs, "Sub-Doppler frequency metrology in HD for tests of fundamental physics," *Physical Reviw Letters*, vol. 120, p. 153002, 2018.

[41] L.-G. Tao, A.-W. Liu, K. Pachucki, J. Komasa, Y. R. Sun, J. Wang, and S.-M. Hu, "Toward a determination of the proton-electron mass ratio from the lamb-dip measurement of HD," *Physical Review Letters*, vol. 120, p. 153001, 2018.

[42] M. Puchalski, J. Komasa, P. Czachorowski, and K. Pachucki, "Complete $\alpha^6\ m$ corrections to the ground state of $H_2$," *Physical Review Letters*, vol. 117, p. 263002, 2016.

[43] M. Puchalski, J. Komasa, and K. Pachucki, “Relativistic corrections for the ground electronic state of molecular hydrogen,” *Physical Review A*, vol. 95, p. 052506, 2017.

[44] K. Pachucki and J. Komasa, “Schrödinger equation solved for the hydrogen molecule with unprecedented accuracy,” *The Journal of Chemical Physics*, vol. 144, no. 16, p. 164306, 2016.

[45] R. E. Moss, “Calculations for the vibration-rotation levels of $H_2^+$ in its ground and first excited electronic states,” *Molecular Physics*, vol. 80, no. 6, pp. 1541–1554, 1993.

[46] R. E. Moss, “Calculations for vibration-rotation levels of $HD^+$, in particular for high N,” *Molecular Physics*, vol. 78, no. 2, pp. 371–405, 1993.

[47] V. I. Korobov, L. Hilico, and J.-P. Karr, “Fundamental transitions and ionization energies of the hydrogen molecular ions with few ppt uncertainty,” *Physical Review Letters*, vol. 118, p. 233001, 2017.

[48] D. Bakalov, V. I. Korobov, and S. Schiller, “High-precision calculation of the hyperfine structure of the $HD^+$ ion,” *Physical Review Letters*, vol. 97, p. 243001, 2006.

[49] V. I. Korobov, J. C. J. Koelemeij, L. Hilico, and J.-P. Karr, “Theoretical hyperfine structure of the molecular hydrogen ion at the 1 ppm level,” *Physical Review Letters*, vol. 116, p. 053003, 2016.

[50] A. D. J. Critchley, A. N. Hughes, and I. R. McNab, “Direct measurement of a pure rotation transition in $H_2^+$,” *Physical Review Letters*, vol. 86, pp. 1725–1728, 2001.

[51] A. D. J. Critchley, A. N. Hughes, I. R. McNab, and R. E. Moss, “Energy shifts and forbidden transitions in $H_2^+$ due to electronic g/u symmetry breaking,” *Molecular Physics*, vol. 101, no. 4-5, pp. 651–661, 2003.

[52] A. Carrington, I. R. McNab, and C. A. Montgomerie, “Microwave electronic spectrum of the $H_2^+$ ion,” *Chemical Physics Letters*, vol. 160, no. 3, pp. 237 – 242, 1989.

[53] A. Carrington, I. R. McNab, and C. A. Montgomerie, “Spectroscopy of the hydrogen molecular ion at its dissociation limit,” *Philosophical Transactions of the Royal Society of London A: Mathematical, Physical and Engineering Sciences*, vol. 324, no. 1578, pp. 275–287, 1988.

[54] F. Bielsa, A. Douillet, T. Valenzuela, J.-P. Karr, and L. Hilico, "Narrow-line phase-locked quantum cascade laser in the 9.2 $\mu$m range," *Optics Letters*, vol. 32, no. 12, pp. 1641–1643, 2007.

[55] J.-P. Karr, F. Bielsa, A. Douillet, J. Pedregosa Gutierrez, V. I. Korobov, and L. Hilico, "Vibrational spectroscopy of $H_2^+$: Hyperfine structure of two-photon transitions," *Physical Review A*, vol. 77, p. 063410, 2008.

[56] L. Hilico, A. Douillet, J.-P. Karr, and E. Tourni, "Note: A high transmission faraday optical isolator in the 9.2 m range," *Review of Scientific Instruments*, vol. 82, no. 9, p. 096106, 2011.

[57] J.-P. Karr, A. Douillet, and L. Hilico, "Photodissociation of trapped $H_2^+$ ions for REMPD spectroscopy," *Applied Physics B*, vol. 107, no. 4, pp. 1043–1052, 2012.

[58] J.-P. Karr, S. Patra, J. C. J. Koelemeij, J. Heinrich, N. Sillitoe, A. Douillet, and L. Hilico, "Hydrogen molecular ions: new schemes for metrology and fundamental physics tests," *Journal of Physics: Conference Series*, vol. 723, no. 1, p. 012048, 2016.

[59] J.-P. Karr, L. Hilico, J. C. J. Koelemeij, and V. I. Korobov, "Hydrogen molecular ions for improved determination of fundamental constants," *Physical Review A*, vol. 94, p. 050501, 2016.

[60] S. Patra, J.-P. Karr, L. Hilico, M. Germann, V. I. Korobov, and J. C. J. Koelemeij, "Proton-electron mass ratio from $HD^+$ revisited," *Journal of Physics B: Atomic, Molecular and Optical Physics*, vol. 51, no. 2, p. 024003, 2018.

[61] S. Alighanbari, M. G. Hansen, V. I. Korobov, and S. Schiller, "Rotational spectroscopy of cold and trapped molecular ions in the Lamb-Dicke regime," *Nature Physics*, vol. 14, no. 6, pp. 555–559, 2018.

[62] R. Pohl, A. Antognini, F. Nez, F. D. Amaro, F. Biraben, J. M. R. Cardoso, D. S. Covita, A. Dax, S. Dhawan, L. M. P. Fernandes, A. Giesen, T. Graf, T. W. Hänsch, P. Indelicato, L. Julien, C.-Y. Kao, P. Knowles, E.-O. Le Bigot, Y.-W. Liu, J. A. M. Lopes, L. Ludhova, C. M. B. Monteiro, F. Mulhauser, T. Nebel, P. Rabinowitz, J. M. F. dos Santos, L. A. Schaller, K. Schuhmann, C. Schwob, D. Taqqu, J. F. C. A. Veloso, and F. Kottmann, "The size of the proton," *Nature*, vol. 466, p. 213, 2010.

[63] R. Pohl, F. Nez, L. M. P. Fernandes, F. D. Amaro, F. Biraben, J. M. R. Cardoso, D. S. Covita, A. Dax, S. Dhawan, M. Diepold, A. Giesen, A. L. Gouvea, T. Graf, T. W. Hänsch, P. Indelicato, L. Julien, P. Knowles,

F. Kottmann, E.-O. Le Bigot, Y.-W. Liu, J. A. M. Lopes, L. Ludhova, C. M. B. Monteiro, F. Mulhauser, T. Nebel, P. Rabinowitz, J. M. F. dos Santos, L. A. Schaller, K. Schuhmann, C. Schwob, D. Taqqu, J. F. C. A. Veloso, and A. Antognini, "Laser spectroscopy of muonic deuterium," *Science*, vol. 353, no. 6300, pp. 669–673, 2016.

[64] A. Beyer, L. Maisenbacher, A. Matveev, R. Pohl, K. Khabarova, A. Grinin, T. Lamour, D. C. Yost, T. W. Hänsch, N. Kolachevsky, and T. Udem, "The Rydberg constant and proton size from atomic hydrogen," *Science*, vol. 358, no. 6359, pp. 79–85, 2017.

[65] H. Fleurbaey, S. Galtier, S. Thomas, M. Bonnaud, L. Julien, F. Biraben, F. Nez, M. Abgrall, and J. Guéna, "New measurement of the $1s-3s$ transition frequency of hydrogen: Contribution to the proton charge radius puzzle," *Physical Review Letters*, vol. 120, p. 183001, 2018.

[66] P. A. M. Dirac, "The cosmological constants," *Nature*, vol. 139, p. 323, 1937.

[67] T. Rosenband, D. B. Hume, P. O. Schmidt, C. W. Chou, A. Brusch, L. Lorini, W. H. Oskay, R. E. Drullinger, T. M. Fortier, J. E. Stalnaker, S. A. Diddams, W. C. Swann, N. R. Newbury, W. M. Itano, D. J. Wineland, and J. C. Bergquist, "Frequency ratio of $\mathrm{Al}^+$ and $\mathrm{Hg}^+$ single-ion optical clocks; metrology at the 17th decimal place," *Science*, vol. 319, no. 5871, pp. 1808–1812, 2008.

[68] R. M. Godun, P. B. R. Nisbet-Jones, J. M. Jones, S. A. King, L. A. M. Johnson, H. S. Margolis, K. Szymaniec, S. N. Lea, K. Bongs, and P. Gill, "Frequency ratio of two optical clock transitions in $^{171}\mathrm{Yb}^+$ and constraints on the time variation of fundamental constants," *Physical Review Letters*, vol. 113, p. 210801, 2014.

[69] N. Huntemann, B. Lipphardt, C. Tamm, V. Gerginov, S. Weyers, and E. Peik, "Improved limit on a temporal variation of $m_p/m_e$ from comparisons of $\mathrm{Yb}^+$ and Cs atomic clocks," *Physical Review Letters*, vol. 113, p. 210802, 2014.

[70] S. M. Kotu, M. T. Murphy, and R. F. Carswell, "High-precision limit on variation in the fine-structure constant from a single quasar absorption system," *Monthly Notices of the Royal Astronomical Society*, vol. 464, no. 3, pp. 3679–3703, 2017.

[71] P. Langacker, G. Segrè, and M. J. Strassler, "Implications of gauge unification for time variation of the fine structure constant," *Physics Letters B*, vol. 528, no. 1, pp. 121 – 128, 2002.

[72] X. Calmet and H. Fritzsch, “A time variation of proton-electron mass ratio and grand unification,” *Europhysics Letters*, vol. 76, no. 6, pp. 1064–1067, 2006.

[73] J. Bagdonaite, P. Jansen, C. Henkel, H. L. Bethlem, K. M. Menten, and W. Ubachs, “A stringent limit on a drifting proton-to-electron mass ratio from alcohol in the early universe,” *Science*, vol. 339, no. 6115, pp. 46–48, 2013.

[74] A. Shelkovnikov, R. J. Butcher, C. Chardonnet, and A. Amy-Klein, “Stability of the proton-to-electron mass ratio,” *Physical Review Letters*, vol. 100, p. 150801, 2008.

[75] J.-P. Karr, “$H_2^+$ and $HD^+$: Candidates for a molecular clock,” *Journal of Molecular Spectroscopy*, vol. 300, pp. 37 – 43, 2014.

[76] E. J. Salumbides, J. C. J. Koelemeij, J. Komasa, K. Pachucki, K. S. E. Eikema, and W. Ubachs, “Bounds on fifth forces from precision measurements on molecules,” *Physical Review D*, vol. 87, p. 112008, 2013.

[77] N. Arkani-Hamed, S. Dimopoulos, and G. Dvali, “The hierarchy problem and new dimensions at a millimeter,” *Physics Letters B*, vol. 429, no. 3, pp. 263 – 272, 1998.

[78] E. J. Salumbides, A. N. Schellekens, B. Gato-Rivera, and W. Ubachs, “Constraints on extra dimensions from precision molecular spectroscopy,” *New Journal of Physics*, vol. 17, no. 3, p. 033015, 2015.

[79] W. Ubachs, J. Koelemeij, K. Eikema, and E. Salumbides, “Physics beyond the standard model from hydrogen spectroscopy,” *Journal of Molecular Spectroscopy*, vol. 320, pp. 1 – 12, 2016.

[80] A. Carrington and R. A. Kennedy, “Vibration-rotation spectroscopy of the $HD^+$ ion near the dissociation limit,” *Molecular Physics*, vol. 56, no. 4, pp. 935–975, 1985.

[81] A. Carrington, I. R. McNab, and C. A. Montgomerie, “Vibration-rotation spectroscopy of the $HD^+$ ion near the dissociation limit,” *Molecular Physics*, vol. 64, no. 4, pp. 679–689, 1988.

[82] A. Carrington, I. R. McNab, and C. A. Montgomerie, “Spectroscopy of the hydrogen molecular ion,” *Journal of Physics B: Atomic, Molecular and Optical Physics*, vol. 22, no. 22, p. 3551, 1989.

[83] A. Carrington, C. A. Leach, A. J. Marr, R. E. Moss, C. H. Pyne, M. R. Viant, Y. D. West, R. A. Kennedy, and I. R. McNab, “Spectroscopy of $HD^+$ in high angular momentum states,” *Chemical Physics*, vol. 166, no. 1, pp. 145 – 166, 1992.

[84] J. C. J. Koelemeij, B. Roth, A. Wicht, I. Ernsting, and S. Schiller, “Vibrational spectroscopy of $HD^+$ with 2-ppb accuracy,” *Physical Review Letters*, vol. 98, p. 173002, 2007.

[85] U. Bressel, A. Borodin, J. Shen, M. Hansen, I. Ernsting, and S. Schiller, “Manipulation of individual hyperfine states in cold trapped molecular ions and application to $HD^+$ frequency metrology,” *Physical Review Letters*, vol. 108, p. 183003, 2012.

[86] J. Biesheuvel, J.-P. Karr, L. Hilico, K. S. E. Eikema, W. Ubachs, and J. C. J. Koelemeij, “High-precision spectroscopy of the $HD^+$ molecule at the 1-p.p.b. level,” *Applied Physics B*, vol. 123, no. 1, p. 23, 2016.

[87] V. Q. Tran, J.-P. Karr, A. Douillet, J. C. J. Koelemeij, and L. Hilico, “Two-photon spectroscopy of trapped $HD^+$ ions in the Lamb-Dicke regime,” *Physical Review A*, vol. 88, p. 033421, 2013.

[88] S. Schiller and V. Korobov, “Tests of time independence of the electron and nuclear masses with ultracold molecules,” *Physical Review A*, vol. 71, p. 032505, 2005.

[89] J. P. Karr and L. Hilico, “High accuracy results for the energy levels of the molecular ions $H_2^+$, $D_2^+$ and $HD^+$ , up to $J = 2$,” *Journal of Physics B: Atomic, Molecular and Optical Physics*, vol. 39, no. 8, p. 2095, 2006.

[90] H. Li, J. Wu, B.-L. Zhou, J.-M. Zhu, and Z.-C. Yan, “Calculations of energies of the hydrogen molecular ion,” *Physical Review A*, vol. 75, p. 012504, 2007.

[91] Y. Ning and Z.-C. Yan, “Variational energy bounds for the hydrogen molecular ion,” *Physical Review A*, vol. 90, p. 032516, 2014.

[92] V. I. Korobov, “Leading-order relativistic and radiative corrections to the rovibrational spectrum of ${H_2}^+$ and $HD^+$ molecular ions,” *Physical Review A*, vol. 74, p. 052506, 2006.

[93] V. I. Korobov, “Relativistic corrections of $m\alpha^6$ order to the rovibrational spectrum of ${H_2}^+$ and $HD^+$ molecular ions,” *Physical Review A*, vol. 77, p. 022509, 2008.

[94] V. I. Korobov, L. Hilico, and J.-P. Karr, “Theoretical transition frequencies beyond 0.1 ppb accuracy in $H_2^+$, $HD^+$, and antiprotonic helium,” *Physical Review A*, vol. 89, p. 032511, 2014.

[95] V. I. Korobov, L. Hilico, and J.-P. Karr, “$m\alpha^7$-order corrections in the hydrogen molecular ions and antiprotonic helium,” *Physical Review Letters*, vol. 112, p. 103003, 2014.

[96] J. C. J. Koelemeij, D. W. E. Noom, D. de Jong, M. A. Haddad, and W. Ubachs, “Observation of the $v = 8 \leftarrow v = 0$ vibrational overtone in cold trapped $HD^+$,” *Applied Physics B*, vol. 107, no. 4, pp. 1075–1085, 2012.

[97] J. Biesheuvel, D. W. E. Noom, E. J. Salumbides, K. T. Sheridan, W. Ubachs, and J. C. J. Koelemeij, “Widely tunable laser frequency offset lock with 30 GHz range and 5 THz offset,” *Optics Express*, vol. 21, no. 12, pp. 14008–14016, 2013.

[98] J. Biesheuvel, “Probing QED and fundamental constants through vibrational spectroscopy of $HD^+$”. PhD thesis, Vrije Universiteit Amsterdam, 2016.

[99] D. J. Wineland and W. M. Itano, “Laser cooling of atoms,” *Physical Review A*, vol. 20, pp. 1521–1540, 1979.

[100] P. Blythe, B. Roth, U. Fröhlich, H. Wenz, and S. Schiller, “Production of ultracold trapped molecular hydrogen ions,” *Physical Review Letters*, vol. 95, p. 183002, 2005.

[101] S. Earnshaw, “On the nature of the molecular forces which regulate the constitution of the luminferous ether,” *Transactions of the Cambridge Philosophical Society*, vol. 7, pp. 97–112, 1842.

[102] F. M. Penning, “Die glimmentladung bei niedrigem druck zwischen koaxialen zylindern in einem axialen magnetfeld,” *Physica*, vol. 3, no. 9, pp. 873 – 894, 1936.

[103] R. S. Van Dyck Jr., P. B. Schwinberg, and H. G. Dehmelt, “Electron magnetic moment from geonium spectra,” in *New frontiers in high-energy physics* (A. Perlmutter and L. F. Scott, eds.), New York: Plenum Press, 1978.

[104] W. Paul and H. Steinwedel, “Notizen: Ein neues massenspektrometer ohne magnetfeld,” *Zeitschrift für Naturforschung A*, vol. 8, pp. 448–450, 1953.

[105] F. G. Major, V. N. Gheorghe, and G. Werth, *Charged Particle Traps*, ch. Introduction, pp. 10–11. Springer Series on Atomic, Optical and Plasma Physics, Springer-Verlag Berlin Heidelberg, 1 ed., 2005.

[106] M. G. Raizen, J. M. Gilligan, J. C. Bergquist, W. M. Itano, and D. J. Wineland, "Ionic crystals in a linear Paul trap," *Physical Review A*, vol. 45, pp. 6493–6501, 1992.

[107] R. Blümel, C. Kappler, W. Quint, and H. Walther, "Chaos and order of laser-cooled ions in a paul trap," *Physical Review A*, vol. 40, pp. 808–823, 1989.

[108] G. Birkl, S. Kassner, and H. Walther, "Multiple-shell structures of laser-cooled $^{2}4\mathrm{Mg}^{+}$ ions in a quadrupole storage ring," *Nature*, vol. 357, p. 310, 1992.

[109] R. G. DeVoe, J. Hoffnagle, and R. G. Brewer, "Role of laser damping in trapped ion crystals," *Physical Review A*, vol. 39, pp. 4362–4365, 1989.

[110] J. D. Prestage, G. J. Dick, and L. Maleki, "New ion trap for frequency standard applications," *Journal of Applied Physics*, vol. 66, no. 3, pp. 1013–1017, 1989.

[111] M. Drewsen, C. Brodersen, L. Hornekær, J. S. Hangst, and J. P. Schifffer, "Large ion crystals in a linear paul trap," *Physical Review Letters*, vol. 81, pp. 2878–2881, 1998.

[112] D. Noom, "A tunable frequency-stabilised laser for cooling and detection of beryllium ions in a trap," Master's thesis, Vrije Universiteit Amsterdam, 2011.

[113] D. J. Larson, J. C. Bergquist, J. J. Bollinger, W. M. Itano, and D. J. Wineland, "Sympathetic cooling of trapped ions: A laser-cooled two-species nonneutral ion plasma," *Physical Review Letters*, vol. 57, pp. 70–73, 1986.

[114] S. Willitsch, M. T. Bell, A. D. Gingell, and T. P. Softley, "Chemical applications of laser- and sympathetically-cooled ions in ion traps," *Physical Chemistry Chemical Physics*, vol. 10, no. 48, pp. 7200–7210, 2008.

[115] Spectra Physics Laser Products Division, *Model 380D Frequency Stabilized Dye Laser Instruction Manual*, 1987.

[116] F. M. J. Cozijn, "Design and construction of a 313 nm diode-laser based system for cooling of trapped beryllium ions," Master's thesis, Vrije Universiteit Amsterdam, 2016.

[117] T. W. Hänsch and B. Couillaud, "Laser frequency stabilization by polarization spectroscopy of a reflecting reference cavity," *Optics Communications*, vol. 35, no. 3, pp. 441 – 444, 1980.

[118] M. Drewsen, I. Jensen, J. Lindballe, N. Nissen, R. Martinussen, A. Mortensen, P. Staanum, and D. Voigt, "Ion coulomb crystals: a tool for studying ion processes," *International Journal of Mass Spectrometry*, vol. 229, no. 1, pp. 83 – 91, 2003.

[119] P. Blythe, B. Roth, U. Fröhlich, H. Wenz, and S. Schiller, "Production of ultracold trapped molecular hydrogen ions," *Physical Review Letters*, vol. 95, p. 183002, 2005.

[120] A. D. Ludlow, X. Huang, M. Notcutt, T. Zanon-Willette, S. M. Foreman, M. M. Boyd, S. Blatt, and J. Ye, "Compact, thermal-noise-limited optical cavity for diode laser stabilization at $1 \times 10^{-15}$," *Optics Letters*, vol. 32, no. 6, pp. 641–643, 2007.

[121] R. W. P. Drever, J. L. Hall, F. V. Kowalski, J. Hough, G. M. Ford, A. J. Munley, and H. Ward, "Laser phase and frequency stabilization using an optical resonator," *Applied Physics B*, vol. 31, no. 2, pp. 97–105, 1983.

[122] C. Hagemann, C. Grebing, C. Lisdat, S. Falke, T. Legero, U. Sterr, F. Riehle, M. J. Martin, and J. Ye, "Ultrastable laser with average fractional frequency drift rate below $5 \times 10^{-19}$/s," *Optics Letters*, vol. 39, no. 17, pp. 5102–5105, 2014.

[123] J. Reichert, R. Holzwarth, T. Udem, and T. W. Hänsch, "Measuring the frequency of light with mode-locked lasers," *Optics Communications*, vol. 172, no. 1, pp. 59 – 68, 1999.

[124] D. J. Jones, S. A. Diddams, M. S. Taubman, S. T. Cundiff, L.-S. Ma, and J. L. Hall, "Frequency comb generation using femtosecond pulses and cross-phase modulation in optical fiber at arbitrary center frequencies," *Optics Letters*, vol. 25, no. 5, pp. 308–310, 2000.

[125] Microsemi Corporation, *Cs*III *Cesium Frequency Standard Datasheet.* 2014.

[126] T. Udem, R. Holzwarth, and T. W. Hänsch, "Optical frequency metrology," *Nature*, vol. 416, p. 233, 2002.

[127] W. Zhang, M. Lours, M. Fischer, R. Holzwarth, G. Santarelli, and Y. L. Coq, "Characterizing a fiber-based frequency comb with electro-optic modulator," *IEEE Transactions on Ultrasonics, Ferroelectrics, and Frequency Control*, vol. 59, no. 3, pp. 432–438, 2012.

[128] H. Telle, B. Lipphardt, and J. Stenger, “Kerr-lens, mode-locked lasers as transfer oscillators for optical frequency measurements,” *Applied Physics B*, vol. 74, no. 1, pp. 1–6, 2002.

[129] L.-S. Ma, M. Zucco, S. Picard, L. Robertsson, and R. S. Windeler, “A new method to determine the absolute mode number of a mode-locked femtosecond-laser comb used for absolute optical frequency measurements,” *IEEE Journal of Selected Topics in Quantum Electronics*, vol. 9, no. 4, pp. 1066–1071, 2003.

[130] J. Zhang, Z. H. Lu, Y. H. Wang, T. Liu, A. Stejskal, Y. N. Zhao, R. Dumke, Q. H. Gong, and L. J. Wang, “Exact frequency comb mode number determination in precision optical frequency measurements,” *Laser Physics*, vol. 17, no. 7, pp. 1025–1028, 2007.

[131] R. v. Rooij, Frequency metrology in quantum degenerate helium. PhD thesis, Vrije Universiteit Amsterdam, 2012.

[132] Open Hardware Repository, *Wiki: White Rabbit*, 2017 (accessed September 27, 2018). https://www.ohwr.org/projects/white-rabbit/wiki.

[133] S. F. Jacobs, “Optical heterodyne (coherent) detection,” *American Journal of Physics*, vol. 56, no. 3, pp. 235–245, 1988.

[134] P. Yu, “A novel scheme for hundred-Hertz linewidth measurements with the self-heterodyne method,” *Chinese Physics Letters*, vol. 30, no. 8, p. 084208, 2013.

[135] L.-S. Ma, P. Jungner, J. Ye, and J. L. Hall, “Delivering the same optical frequency at two places: accurate cancellation of phase noise introduced by an optical fiber or other time-varying path,” *Optics Letters*, vol. 19, no. 21, pp. 1777–1779, 1994.

[136] G. Grosche, “Eavesdropping time and frequency: phase noise cancellation along a time-varying path, such as an optical fiber,” *Optics Letters*, vol. 39, no. 9, pp. 2545–2548, 2014.

[137] C. v. Tour, “Ultrastable optical frequency transfer over actively compensated amplified fiber links,” Master’s thesis, TU Delft and Vrije Universiteit Amsterdam, 2016.

[138] P. A. Williams, W. C. Swann, and N. R. Newbury, “High-stability transfer of an optical frequency over long fiber-optic links,” *Journal of Optical Society of America B*, vol. 25, no. 8, pp. 1284–1293, 2008.

[139] D. Bakalov, V. I. Korobov, and S. Schiller, "Magnetic field effects in the transitions of the $HD^+$ molecular ion and precision spectroscopy," *Journal of Physics B: Atomic, Molecular and Optical Physics*, vol. 44, no. 2, p. 025003, 2011.

[140] J.-P. Karr, V. I. Korobov, and L. Hilico, "Vibrational spectroscopy of ${H_2}^+$: Precise evaluation of the Zeeman effect," *Physical Review A*, vol. 77, p. 062507, 2008.

[141] J. C. J. Koelemeij, B. Roth, and S. Schiller, "Blackbody thermometry with cold molecular ions and application to ion-based frequency standards," *Physical Review A*, vol. 76, p. 023413, 2007.

[142] C. W. Chou, D. B. Hume, J. C. J. Koelemeij, D. J. Wineland, and T. Rosenband, "Frequency Comparison of Two High-Accuracy $Al^+$ Optical Clocks," *Physical Review Letters*, vol. 104, p. 070802, 2010.

[143] S. Patra and J. C. J. Koelemeij, "Ghost features in Doppler-broadened spectra of rovibrational transitions in trapped $HD^+$ ions," *Journal of Molecular Spectroscopy*, vol. 332, pp. 109 – 116, 2017.

[144] J. J. Spezeski. PhD thesis, Yale University, 1977.

[145] J. C. J. Koelemeij, "Infrared dynamic polarizability of $HD^+$ rovibrational states," *Physical Chemistry Chemical Physics*, vol. 13, pp. 18844–18851, 2011.

[146] S. G. Karshenboim and V. G. Ivanov, "Quantum electrodynamics, high-resolution spectroscopy and fundamental constants," *Applied Physics B*, vol. 123, no. 1, p. 18, 2016.

[147] J.-P. Karr, L. Hilico, and V. I. Korobov, "One-loop vacuum polarization at $m\alpha^7$ and higher orders for three-body molecular systems," *Physical Review A*, vol. 95, p. 042514, 2017.

[148] Z.-X. Zhong, P.-P. Zhang, Z.-C. Yan, and T.-Y. Shi, "Precision spectroscopy of the hydrogen molecular ion $HD^+$," *Physical Review A*, vol. 86, p. 064502, 2012.

[149] V. I. Korobov and Z.-X. Zhong, "Bethe logarithm for the $H_2^+$ and $HD^+$ molecular ions," *Physical Review A*, vol. 86, p. 044501, 2012.

[150] J. P. Karr, 2017. Private communication.

[151] B. L. Welch, "The generalization of 'Student's' problem when several different population varlances are involved," *Biometrika*, vol. 34, no. 1-2, pp. 28–35, 1947.

[152] Student (W. S. Gosset), “The probable error of a mean,” *Biometrika*, vol. 6, no. 1, pp. 1–25, 1908.

[153] Wikipedia, *Welch’s t-test*, 2018 (accessed September 30, 2018). https://en.wikipedia.org/wiki/Welch

[154] H. B. Prosper, “Practical statistics for particle physicists,” *arXiv:1608.03201*, 2016.

[155] P. J. Mohr, B. N. Taylor, and D. B. Newell, “CODATA recommended values of the fundamental physical constants: 2006,” *Rev. Mod. Phys.*, vol. 80, pp. 633–730, Jun 2008.

[156] R. Pohl, “Laser spectroscopy of muonic hydrogen and the puzzling proton,” *Journal of the Physical Society of Japan*, vol. 85, no. 9, p. 091003, 2016.

# Acknowledgement

From the day I joined for my doctoral studies at the Vrije Universiteit Amsterdam to the day this thesis was approved by the members of the reading committee, it has been a long journey. Although only my name is there on the title page of this dissertation, it is obvious that this endeavour would not be successful without the contributions of many more people. So the least I can do is to acknowledge their help and support here.

To begin with, I would like to thank Jeroen Koelemeij, my copromotor for providing me with the opportunity to work in his group as a PhD student. Jeroen, I admire your acumen and creativity in solving a scientific problem, be it theoretical or experimental. Your knowledge, experience and optimism have been invaluable to this work. Moreover, your ability to be patient and always be in a jovial mood is something I look up to. Also, let me take this opportunity to apologise to you for all the emails and text messages in WhatsApp sent at ungodly hours over the past five years. Even more surprising is that some times, I would also receive replies to them almost immediately. It has been a pleasure working with you. Dank u wel Jeroen!

My gratitude goes to my promotors Wim Ubachs and Kjeld Eikema for their support. Wim and Kjeld's encouragement, enthusiasm and a pragmatic approach in setting realisable goals have been instrumental in finishing this thesis. Kjeld has been of great help in setting up and the working of the frequency stabilisation of the spectroscopy lasers. Not only did he provide us space in his already crowded lab to set up our lasers and associated electronics, but also shared his deep knowledge of frequency comb lasers in getting it to work. His experience with dye lasers was particularly important to us when he identified that we were missing a crucial element in our dye circulation system for our continuous wave dye laser. Wim and Kjeld, thank you for your help and support!

This experiment would not be possible without the detailed feasibility study of the problem by the group of Laurent Hilico and Jean-Philippe Karr from LKB, Paris, who we are glad to have as our collaborators. I convey my thanks and gratitude to them. I am lucky to have visited them on several occasions during my PhD, where they are also pursuing a similar experiment as described in this work on $H_2^+$. The exchanges with them have been stimulating and encouraging every single time. On one of my visits, Laurent was kind enough to introduce me into the world of molecular dynamics simulations. For our experiment, precise theoretical values of the transition we are measuring is essential. These values are made available to us by Vladimir Korobov of JINR Dubna, Russia and Jean-Philippe Karr, who are world leaders in calculating precise energy level structure of three-body systems like the hydrogen molecular ions. I am grateful for having both of them as our collaborators. During my visits to Paris, I also came to know Albane Douillet and Johannes Heinrich, with whom interactions, both academic and others have been very enjoyable.

My regards to Subhadeep De of the National Physical Laboratory, New Delhi in India, who was a guest scientist in our group in 2015. I enjoyed working with him in the lab during his short visit here.

Coming to colleagues, it was Jurriaan Biesheuvel who introduced me to ion trapping and laser cooling in the lab first hand. Even after leaving the group and joining another job for long, he found time to come back to the lab to help us with some Python related issues in our experimental control programme. Thanks to Tjeerd Pinkert, who taught me quite a bit of fibre-optics and helped me set up the laser frequency stabilisation part of the experiment. Tjeerd's script for controlling the DDS has also been very useful to us. Frank Cozijn, thank you for designing the SHG cavity we use to laser-cool $Be^+$ ions. In an experimental setup where many things need to be optimised almost on a daily basis, your SHG cavity has been an island of calm and stability. Also, your inputs with the diode lasers and the loop antenna have been very helpful, not to forget your regular presence at our setup and encouragements.

Progress became a lot better when Matthias Germann joined our group as a postdoc in October 2016. For many atomic and molecular physicists, spending long hours everyday in a cold and dark room is a reality that has to be accepted. Thanks to Matthias for sharing that burden day in and day out. Also, thanks for helping me find my way a bit in the puzzling world of angular momentum algebra in molecules, which at some points made me feel like I was suffering from Dyslexia. Scientific discussions with you have always been engaging and inspiring, be it in the lab or over a beer.

It would be a crime not to mention Rob Kortekaas, our group technician. Whenever we asked him for help, he would do it as soon as it was possible for him. Particularly, it was a large part due to him that moving our entire setup from one part of the lab to a new location was completed without a hitch. However, it was quite painful for a night owl like me to be in the lab at 8 am in the morning during the move and I was late by 10 minutes or so. Since then, Rob has kept reminding me that on occasions when I happen to be in the lab before 9 in the morning (other than Monday) by asking if I am sick. Thanks Rob! It would not be possible to build up the experimental setup without your help. I would also thank the members of the Electronics and Mechanical workshops of the university, who have built or repaired several devices that we use regularly. Particularly I would like to mention the names of Tim Kortekaas, Mario Molenaar, Wesley Delmeer, Tinco Brouwer, Pieter Caspers, Peter Stevens and Rob Limburg of the Electronics workshop.

My regards to Chantal van Tour and Konstantinos Mourtziapis (former employee) of OPNT for helping us to set up our intra-lab White rabbit network for frequency and data transfer.

Madhu Trivikram, it was a pleasure getting to know you. Thanks for being a great friend and an elder brother. Thanks to you and your wife Anupama, I got to have great food very often throughout the majority of the last 5 years. Being far away from home, they were a treat every single time.

It has been a privilege to work with all other members of the Atoms, Molecules and Laser Physics group of the LaserLaB during my PhD. Edcel Salumbides has been of great help during my first experience in trying to get our dye laser to lase and also for his encouragements throughout. Thanks to Adonis Flores, Hari Mishra, Remy Notermans, Bob Rengelink, Laura Dreissen, Ruud van der Beek, Robert Altmann, Mingli Niu, Aernout van der Poel, Cunfeng Cheng, Jowel Hussels, Yuri van der Werf, Raphaël Jannin and all other colleagues who I had the pleasure of interacting almost on a daily basis for some parts or the entirety of my PhD. Discussions with you have allowed me to learn things beyond the scope of my dissertation. I would also like to thank Rick Bethlem for allowing us to use his “Beauty” in our experiment. My thanks to also Wim Vassen for always being an encouraging figure in the group. It is unfortunate for the scientific community to have lost him so prematurely. My condolences to his family!

Last but not the least, working here would not be possible without the continuous support of my parents, who live far in India. Visiting them once or twice a year is never sufficient, but their unwavering love has been an emotional pillar to get going in times good or bad. Coming to my friends in India, who are my extended family, on numerous occasions I have missed spending time with you, but sometimes I was glad that I was living far from you all.